Nonlinear response in engineered optical materials

GUSTAV STRÖMQVIST

KTH Engineering Sciences

Doctoral Thesis
Department of Applied Physics
KTH – Royal Institute of Technology
Stockholm, Sweden 2012

Nonlinear response in engineered optical materials

Laser Physics
Department of Applied Physics
KTH – Royal Institute of Technology
106 91 Stockholm
Sweden

ISBN 978-91-7501-295-7
TRITA-FYS 2012:13
ISSN 0280-316X
ISRN KTH/FYS/--12:13--SE

Akademisk avhandling som med tillstånd av Kungliga Tekniska Högskolan framläggs till offentlig granskning för avläggande av teknologie doktorsexamen fredagen den 27 april 2012 kl. 10:15 i sal FD5, Albanova, Roslagstullsbacken 21, KTH, Stockholm. Avhandlingen kommer att försvaras på engelska.

Cover picture: Visible beams, angularly dispersed in a glass prism, after the generation through non-phase-matched frequency mixing of the pump and the signal in a mirrorless optical parametric oscillator: pump (infrared, appears purple), signal + signal (red), pump + signal (green) and pump + pump (blue).

Printed by Universitetsservice US AB, Stockholm 2012

Gustav Strömqvist
Nonlinear response in engineered optical materials
Laser Physics, Department of Applied Physics, KTH – Royal Institute of Technology, 106 91 Stockholm, Sweden
ISBN 978-91-7501-295-7, TRITA-FYS 2012:13, ISSN 0280-316X, ISRN KTH/FYS/--12:13--SE

Abstract

Material and structure engineering are increasingly employed in active optical media, in this context defined as media capable of providing laser or/and optical parametric gain. For laser materials, the main aim of the engineering is to tailor the absorption and emission cross sections in order to optimise the laser performance. At the same time, the engineering also results in a collateral modification of the material's nonlinear response. In the first part of this work, the nonlinear index of refraction is characterised for two crystallographic forms of laser-ion doped and undoped double-tungstate crystals. These laser crystals have broad gain bandwidths, in particular when doped with Yb^{3+}. As shown in this work, the crystals also have large Kerr nonlinearities, where the values vary significantly for different chemical compositions of the crystals. The combination of a broad gain bandwidth and a high Kerr nonlinearity makes the laser-ion doped double tungstates excellent candidates to employ for the generation of ultrashort laser pulses by Kerr-lens modelocking.

The second part of the work relates to the applications of engineered second-order nonlinear media, which here in particular are periodically-poled $KTiOPO_4$ crystals. Periodic structure engineering of second-order nonlinear crystals on a submicrometre scale opens up for the realisation of novel nonlinear devices. By the use of quasi-phase matching in these structures, it is possible to efficiently down-convert a pump wave into two counterpropagating parametric waves, which leads to a device called a mirrorless optical parametric oscillator. The nonlinear response in these engineered submicrometre structures is such that the parametric wave that propagates in the opposite direction of the pump automatically has a narrow bandwidth, whereas the parametric wave that propagates with the pump essentially is a frequency-shifted replica of the pump wave. The unusual spectral properties and the tunabilities of mirrorless optical parametric oscillators are investigated.

Keywords: nonlinear optics, nonlinear index of refraction, double tungstates, periodic poling, $KTiOPO_4$, quasi-phase matching, parametric down-conversion, mirrorless optical parametric oscillators

Sammanfattning

I den här doktorsavhandlingen studeras optiska ickelinjäriteter i material som kan manipuleras för att förändra deras optiska egenskaper. Materialen som avses är antingen laserkristaller, som används för direkt framställning av laserljus, eller kristaller med en andra ordningens ickelinjäritet, som används för frekvenskonvertering av befintliga laserstrålar.

Laserkristallerna som behandlas i den här avhandlingen är dubbelvolframat, och även något dubbelmolybdat, med kemisk beteckning $MT(XO_4)_2$. M är här natrium eller kalium, T är en trevärd katjon och X är antingen volfram eller molybden. Dessa kristaller har de senaste åren fått en ökad användning som värdmaterial för laserjoner, såsom Yb^{3+}, Nd^{3+} och Tm^{3+}. I avhandlingen visas att det ickelinjära brytningsindexet, n_2, i dessa kristaller är relativt högt och också har en relativt stor variation mellan olika kemiska och kristallografiska sammansättningar. De uppmätta värdena på n_2 är mellan $13 \cdot 10^{-16}$ cm^2/W och $68 \cdot 10^{-16}$ cm^2/W. Ickelinjäriteten är tillräckligt stor för att kunna användas för att modlåsa lasrarna enbart med hjälp av den optiska Kerr-effekten i laserkristallerna, vilket innebär att det ickelinjära brytningsindexet ger upphov till att kristallerna fungerar som ickelinjära linser. När de dubbelvolframaten dopas med Yb^{3+} är emissionstvärsnittet tillräckligt brett för att kunna generera pulser som är betydligt kortare än 100 femtosekunder. Värdena på n_2 för dubbelvolframaten är betydligt högre än det för safir, $3.1 \cdot 10^{-16}$ cm^2/W, som dopat med titan är den lasertyp som idag främst använder den optiska Kerr-effekten för modlåsning.

I den andra delen av avhandlingen behandlas den ferroelektriska kristallen $KTiOPO_4$. Med hjälp av polning av kristallen är det möjligt att lokalt byta tecken på kristallens andra ordnigens ickelinjäritet. När det här görs periodiskt i kristallen så ändras de ickelinjära egenskaperna och kristallen kan användas för effektiv frekvenskonvertering av laserljus genom kvasifasanpassade processer. Med dagens teknologi kan perioderna göras under en mikrometer, vilket gör det möjligt att parametriskt nedkonvertera pumpljus till två parametriska vågor som färdas i motsatta riktningar. Tillskillnad från det normala fallet när båda parametriska vågorna färdas i samma riktning som pumpljuset, så leder de motpropagerande parametriska vågorna till optisk parametrisk oscillation utan behov av speglar för återkoppling. Istället sker återkopplingen automatiskt mellan de motpropagerande parametriska vågorna. I avhandlingen visas att den här typen av ljuskälla har unika spektrala egenskaper som automatiskt leder till att det genererade ljuset är spektralt smalbandigt, vilket inte sker i det normala fallet då båda parametriska vågorna färdas med pumpljuset. Våglängden på det parametriska ljuset som färdas i motsatt riktning mot pumpljuset är starkt kopplat till periodiciteten av modulationen av den ickelinjära koefficienten och kan bara ändras marginellt genom att byta våglängd på pumpljuset. Den parametriska vågen som färdas i samma riktining som pumpljuset får i det närmaste pumpljusets spektrala egenskaper.

Contents

List of publications

This thesis is based on the following journal papers.

I A. García-Cortés, M.D. Serrano, C. Zaldo, C. Cascales, G. Strömqvist and V. Pasiskevicius,
Nonlinear refractive indices of disordered $NaT(XO_4)_2$ T = Y, La, Gd, Lu and Bi, X = Mo, W femtosecond laser crystals,
Appl. Phys. B **91** 507-510 (2008).

II N. Thilmann, G. Strömqvist, M.C. Pujol, V. Pasiskevicius, V. Petrov and F. Díaz,
Nonlinear refractive indices in Yb^{3+}-doped and undoped monoclinic double tungstates $KRE(WO_4)_2$ where RE = Gd, Y, Yb, Lu,
Appl. Phys. B **96** 385-392 (2009).

III A. Zukauskas, G. Strömqvist, V. Pasiskevicius, F. Laurell, M. Fokine and C. Canalias,
Fabrication of submicrometer quasi-phasematched devices in KTP and RKTP [Invited],
Opt. Mater. Express **1**, 1319-1325 (2011).

IV G. Strömqvist, V. Pasiskevicius and C. Canalias,
Self-established noncollinear oscillation and angular tuning in a quasiphase-matched mirrorless optical parametric oscillator,
Appl. Phys. Lett. **98**, 051108 (2011).

V G. Strömqvist, V. Pasiskevicius, C. Canalias and C. Montes,
Coherent phase-modulation transfer in counterpropagating parametric down-conversion,
Phys. Rev. A **84**, 023825 (2011).

VI G. Strömqvist, V. Pasiskevicius, C. Canalias, P. Aschieri, A. Picozzi and C. Montes,
Temporal coherence in mirrorless optical parametric oscillators,
J. Opt. Soc. Am. B **29** (2012) [accepted for publication].

Related publications not included in the thesis

A V. Pasiskevicius, G. Strömqvist and C. Canalias,
Noncollinear mirrorless optical parametric oscillator,
CLEO - Conference on Lasers and Electro-Optics, San Jose, USA (2008).

B V. Pasiskevicius, C. Canalias, G. Strömqvist and F. Laurell,
Mirrorless OPO: first steps towards unlocking the potential of counter-propagating three-wave interactions (invited),
Proc. SPIE 6875, 687508 (2008)

C A. García-Cortés, M.D. Serrano, C. Zaldo, C. Cascales,
G. Strömqvist and V. Pasiskevicius,
Z-scan measurements of nonlinear refractive indices of $NaT(XO_4)_2$ T= Y, La, Gd, Lu and Bi, X= Mo, W, femtosecond laser crystals,
Proc. SPIE 6998, 69981N (2008).

D G. Strömqvist, V. Pasiskevicius and C. Canalias,
Spectral Properties of a Mirrorless Optical Parametric Oscillator,
CLEO - Conference on Lasers and Electro-Optics, Baltimore, USA (2009).

E G. Strömqvist, V. Pasiskevicius and C. Canalias,
Spectral Properties of a Mirrorless Optical Parametric Oscillator,
20^{th} International Laser Physics Workshop, Sarajevo, Bosnia and Herzegovina (Invited) (2011).

F V. Pasiskevicius, G. Strömqvist, F. Laurell and C. Canalias,
Quasi-phase matched nonlinear media: Progress towards nonlinear optical engineering,
Optical Materials **34** (2012) 513-523.

Author contribution

My contribution in the original papers was the following:

I I performed the experiments together with A. García-Cortés under supervision of V. Pasiskevicius.

II I performed the experiments together with N. Thilmann under supervision of V. Pasiskevicius.

III I did the crystal processing, periodic poling and optical evaluation of the KTP and Rb:KTP crystals with the periodicity of $\Lambda = 38.86$ μm and thickness of 3 mm under supervision of C. Canalias.

IV I performed the experiments, did the calculations and wrote the paper with assistance from C. Canalias and V. Pasiskevicius.

V I performed the experiments and wrote the paper together with V. Pasiskevicius.

VI I performed the experiments and wrote the paper with assistance from V. Pasiskevicius and C. Montes.

Preface

The research forming this thesis was performed in the Laser Physics group at the Department of Applied Physics at KTH from 2007 to 2012.

Just before I started my PhD studies, the first mirrorless optical parametric oscillator was demonstrated in this group. I have had the privilege to work with and characterise this device together with Carlota and Valdas. Some of the experiments resulted in paper IV, paper V and paper VI, which constitute the basis of a large part of this thesis.

The crystals used for the characterisation of the nonlinear index of refraction of different double-tungstate compounds in paper I and paper II were supplied by crystal growers in the EU project DT-CRYS.

This work would not have been possible without the financial support from The Swedish Research Council (VR) and the EU project DT-CRYS.

The thesis summarises the work of six journal articles. The first part of the thesis gives an overview of the work and reprints of the articles are found in the second part.

Acknowledgements

First of all, I want to thank my main supervisor Valdas Pasiskevicius. I have learned many things by working together with Valdas in the lab, everything from the tedious alignment of delay lines to the beauty of second-harmonic generation in raw sugar from Sibiriens Soppkök. The quality of this work would have been greatly reduced without the assistance from Valdas.

I also want to thank my other supervisor Fredrik Laurell, for giving me the chance to start in the Laser Physics group, for the barbecue parties, for all the funny stories and for giving me the opportunity to practise my German almost every day.

Apart from Valdas and Fredrik, I want to thank the present and past members of the Laser Physics group for good company in the office, in the lab, at the coffee breaks and on conference trips. I would like to give special thanks to the following group members:
- Carlota Canalias, for being a very nice office mate, for teaching me how to pole PPKTP crystals, for the MOPO experiments and for all the tips about what to do and what not to do in Barcelona.
- Katia Gallo, for always taking her time to discuss nonlinear optics and also explaining it in a very pedagogic way.
- Björn Le Normand (Jacobsson), for always being helpful and sharing his skills, both in the lab and with Fourier transforms.
- Pär Jelger, for excellent company on the conference trips to Denver and Barcelona, and also for keeping me updated with what is going on in the gardening business.
- Hoon Jang, both for all the physics discussions and for the sushi deliveries when I have worked late with this thesis.

I also want to thank everybody that I have published papers with. Apart from Valdas and Carlota that have already been mentioned, I in particular want to thank Carlos Montes for the simulations in paper V and paper VI and the corresponding figures in this thesis.

Believe it or not, there is more in the world than nonlinear optics. Without mentioning any names (you know who you are), I would like to thank my friends from the world outside for the ski trips, for the training for Lidingöloppet, for innebandy on Sundays, and for great company in general.

I want to thank my parents for all the support during all these years. Another big thank you goes to my sisters for always looking out for me and for unintentionally(?) putting some pressure on me to no longer be the one sibling in the family without a PhD.

Last, but definitely not least, I want to thank Helene for always being there for me and for making my life so much better.

List of abbreviations and symbols

The following abbreviations and symbols for physical quantities are used throughout the thesis.

BPM	birefringent phase matching
FWHM	full width at half maximum
MOPO	mirrorless optical parametric oscillator
MTX	double tungstate or double molybdate
OPO	optical parametric oscillator
QPM	quasi-phase matching
TPA	two-photon absorption
$\mathbf{r} = x\hat{\mathbf{e}}_x + y\hat{\mathbf{e}}_y + z\hat{\mathbf{e}}_z$	spatial coordinate
t	time
ε_0	permittivity of free space
μ_0	permeability of free space
$i = \sqrt{-1}$	imaginary unit
λ	vacuum wavelength
ν	frequency
$\omega = 2\pi\nu$	angular frequency
$\mathbf{k}$	wave vector
$k = \lvert\mathbf{k}\rvert = 2\pi n/\lambda = \omega n/c$	wave-vector magnitude
$c = 1/\sqrt{\mu_0\varepsilon_0} = \lambda\nu$	speed of light in vacuum
$v = \omega/k = c/n$	speed of light in a medium
$v_g = \partial\omega/\partial k = c/n_g$	group velocity
n	refractive index
n_2	nonlinear refractive index
n_g	group index
$\beta_2 = \partial^2 k/\partial\omega^2$	group-velocity dispersion
Λ	spatial period
$\mathbf{K}_G$	grating vector
$K_G = \lvert\mathbf{K}_G\rvert = 2\pi/\Lambda$	grating-vector magnitude
$\chi^{(N)}_{jk\ldots}$	N^{th}-order electric susceptibility
$\tilde{\mathbf{E}}$	electric field
$\mathbf{E}$	complex amplitude of $\tilde{\mathbf{E}}$

Part I

Background and overview

Chapter 1

Introduction

1.1 Background

Sources of coherent electromagnetic radiation at optical frequencies have applications in many areas, such as material processing, telecommunication, optical storage, spectroscopy and laser surgery. These sources are either lasers or laser-pumped devices based on nonlinear optics. A laser consists of a *gain medium*, in which the laser light is amplified, and a *cavity*, in which the laser light is resonant. The amplification can only occur when the gain medium is *pumped*, which means that energy somehow has to be externally supplied. This could be done *e.g.* electrically, as for diode lasers, or optically, as for solid-state lasers. The energy supplied to the gain medium can be released in the form of laser light, as well as in the form of unwanted heat. Since the first laser action in ruby in 1960 [1], lasing has been achieved in many different media. These include gases, like the HeNe laser [2], rare-earth ions, like Nd^{3+} [3] and Yb^{3+} [4] in solid-state hosts, semiconductors [5] and liquids, like organic dyes [6]. For the control of the laser output in the time domain, Q-switching [7] and modelocking [8] can be applied to generate pulses with length of around nanoseconds and down to femtoseconds, respectively.

The frequency of the emitted laser light is determined by the energy-level structure of the gain medium. Solid-state lasers cover a large part of the near-infrared spectral region with Nd^{3+} and Yb^{3+} emitting around 1 μm, Er^{3+} around 1.5 μm and Ho^{3+} and Tm^{3+} around 2 μm. The laser light can by the use of *nonlinear optics* be converted in the frequency domain in order to fill the gaps between the different emission lines. Through interactions with a nonlinear polarisation, in particular a second-order nonlinear polarisation, light at twice the frequency of the incoming laser light can be generated through *second-harmonic generation* (SHG), which was demonstrated in 1961 [9] shortly after the invention of the laser. Similarly, the mixing of two laser beams with distinct frequencies in a nonlinear medium may lead to *sum-frequency generation* (SFG) [10] or *difference-frequency generation* (DFG)

[11]. By placing a nonlinear medium inside a resonant cavity, an *optical parametric oscillator* (OPO) [12] is formed, which can be used to generate new frequencies. OPOs normally have a large tuning range and can be used to generate coherent radiation in spectral regions where no suitable laser transitions are found. All these nonlinear processes require rather high intensities and therefore need lasers.

1.2 Engineering of laser media

The energy levels for laser ions in solid-state host materials are affected by the crystal potential at the lattice sites where the laser ions are situated. The host material thereby modifies the magnitude and the spectrum of absorption and emission cross sections in the laser ion, which to some extent can be tailored by the synthesisation of suitable host materials. Apart from leading to host materials with the desired emission and absorption properties, the laser-material engineering may also lead to a collateral modification of the nonlinear response.

The double tungstates constitute a group of crystals to recently gain prominence as host materials for laser ions. These crystals are characterised by large spectroscopic cross sections and are very suitable for spectral engineering. The crystals are *polystructural* and crystallise in monoclinic or tetragonal forms. In the tetragonal form, the crystals are *disordered*, meaning that two different ions are randomly distributed on the same lattice sites, which leads to inhomogeneously-broadened cross sections for Yb^{3+} with spectral widths that can support the generation of pulses with a temporal length well below 100 fs. Together with the broad cross sections, the double tungstates have, as determined in this work, rather high Kerr nonlinearities. The combination of broad cross sections and a high Kerr nonlinearity makes these crystals excellent candidates for the generation of ultrashort laser pulses by *Kerr-lens modelocking* [13]. It is then important to know the values of the Kerr coefficients in order to properly design the laser cavities. It is shown here that there is a rather large variation in the Kerr nonlinearity between different chemical compositions, which can be exploited for future material-design approaches.

1.3 Engineering of second-order nonlinear media

Unlike in laser media, where the nonlinear response is collaterally modified when the cross sections are engineered, modification of the nonlinear response is the main aim of engineering of second-order nonlinear media. The engineering of second-order media in this thesis is *structure engineering* in ferroelectric crystals. By locally varying the sign of the second-order nonlinear coefficient, typically in a periodic manner, the spectral properties of the nonlinear processes in the medium are modified as a result of *quasi-phase matching* (QPM) [14]. The ferroelectric medium that is used here is $KTiOPO_4$ (KTP), both in its pure form and also doped with a small concentration of rubidium. The small amount of Rb^+ replacing K^+ only has minor effects on the nonlinear response of KTP, but it modifies the

properties of *ferroelectric-domain switching* in the material and makes the crystals easier to work with.

Periodic switching of ferroelectric domains on a submicrometre scale leads to the possibility to construct new types of nonlinear devices. One example is a *mirrorless* optical parametric oscillator (MOPO). Unlike a conventional OPO, which relies on feedback from a resonant cavity, a MOPO is based on a distributed-feedback mechanism that is automatically established between two counterpropagating parametric waves. This concept was proposed in 1966 [15], but was not experimentally realised until 2007 [16]. The reason for this 41-year delay between the idea and the realisation is the difficulty to construct a domain grating with submicrometre periodicity that is uniform on the length scale of millimetres in one spatial direction and hundreds of micrometres in the other two directions. The nonlinear response in the engineered crystal with submicrometre periodicity has the useful property that it automatically leads to the generation of spectrally-narrow parametric waves. This is normally not the case in conventional OPOs, where the output spectra are wide, unless narrowed down by *e.g.* etalons [17, 18], surface gratings [18] or volume Bragg gratings [19].

1.4 Object of this thesis

The object of this thesis is first to study the nonlinear response in two types of double-tungstate laser crystals that are promising candidates as gain media for the generation of ultrashort pulses. The other part of the thesis deals with the structuring technology of $KTiOPO_4$, which leads to the realisation of a mirrorless optical parametric oscillator in periodically-poled $KTiOPO_4$ with a submicrometre periodicity. The spectral properties and the tunability of this device are investigated.

1.5 Outline of this thesis

This thesis is based on the original peer-reviewed publications paper I to paper VI, which are reproduced in Part II. In Part I, Chapter 2 gives an introduction to nonlinear optics, with the focus on quasi-phase-matched second-order nonlinear processes, optical parametric oscillators and the effects of a nonlinear index of refraction. Chapter 3 is based on paper I and paper II and deals with the measurement of the nonlinear index of refraction in different double-tungstate laser crystals. Domain engineering in $KTiOPO_4$ for frequency conversion of optical beams is described in Chapter 4, together with the findings in paper III. Chapter 5 deals with mirrorless optical parametric oscillators realised in periodically-poled $KTiOPO_4$ with a submicrometre periodicity. The focus is on the spectral properties and on the tunabilities, which are based on the findings in paper IV, paper V, and paper VI. A conclusion of the work is given in Chapter 6.

Chapter 2

Light-matter interactions

A classical picture of light-matter interactions is that the electric field of the light induces oscillating dipoles in the medium in which it propagates. The dipoles radiate secondary light at their oscillation frequencies, which in linear media are the same frequencies as those in the incoming light. The effect of linear interactions is a dispersion relation and the light travelling through the medium is slowed down. In nonlinear media, the response of the induced dipoles is nonlinear and the dipoles also oscillate, and thereby radiate, at frequencies that are not present in the incoming light, which may lead to the generation of new frequencies.

This chapter gives a brief general overview of optical beams and a frequency-domain description of second-order and third-order nonlinear optics, with a focus on the processes and techniques that are relevant in this thesis: quasi-phase matching, optical parametric oscillation and the effects of a nonlinear index of refraction. The concepts described in this chapter are mainly based on the books by Yariv [20], Boyd [21], and Sutherland [22], in which more complete descriptions are found. The dipole approximation is used and all quantities are given in SI units.

2.1 The optical field

Being an electromagnetic wave, light is characterised by its electric and magnetic components, $\tilde{\mathbf{E}}(\mathbf{r},t)$ and $\tilde{\mathbf{B}}(\mathbf{r},t)$, which evolve in space and time in accordance with Maxwell's equations. The fields interact with charged particles in matter, but the light-matter interactions at optical frequencies are significantly stronger for the electric-field component and the magnetic interactions can normally be disregarded. For the applications described in this thesis, the interacting light will be quasi-monochromatic laser beams with electric fields of the form

$$\tilde{\mathbf{E}}(\mathbf{r},t) = \tfrac{1}{2}\mathbf{E}(\mathbf{r},t)e^{-i\omega t} + c.c., \tag{2.1}$$

where $\mathbf{E}(\mathbf{r},t)$ denotes a complex amplitude that is slowly varying in time in comparison with the exponential containing the the carrier frequency, $\exp(-i\omega t)$. The complex conjugate, *c.c.*, is added to ensure that the electric field is real. Together with $\mathbf{E}(\mathbf{r},t)$, a spatially slowly-varying amplitude, $\mathbf{A}(\mathbf{r},t)$, is defined as $\mathbf{E}(\mathbf{r},t) = \mathbf{A}(\mathbf{r},t)\exp(i\mathbf{k}\cdot\mathbf{r})$, where $\mathbf{k}$ is the wave vector that defines the propagation direction of the beam and has the magnitude $k = \omega n/c = 2\pi n/\lambda$. The beams are referred to as quasi-monochromatic, meaning that the width, $\Delta\omega$, of the temporal Fourier transform of $\tilde{E}(\mathbf{r},t)$ is small compared to the carrier frequency, $\Delta\omega/\omega \ll 1$.

At optical frequencies, the oscillations of $\tilde{E}(\mathbf{r},t)$ are too rapid to detect with electronic detection systems. However, $\tilde{E}(\mathbf{r},t)$ can be reconstructed by the use of attosecond pulses [23], but the amplitude of $\tilde{E}(\mathbf{r},t)$ is more often indirectly determined through the *intensity*, $I(\mathbf{r},t)$, which is proportional to the temporal average of the square of the electric field,

$$I(\mathbf{r},t) = \tfrac{1}{2}\varepsilon_0 cn|A(\mathbf{r},t)|^2. \tag{2.2}$$

The direction of $\tilde{\mathbf{E}}(\mathbf{r},t)$ is referred to as the polarisation of the optical wave, which in vacuum and in isotropic media lies in a plane perpendicular to the propagation direction $\mathbf{k}$. The beams considered in this thesis are *linearly polarised*, meaning that $\tilde{\mathbf{E}}(\mathbf{r},t)$ oscillates in the same direction at all points in the beam. The polarisation direction is important for many applications in nonlinear optics.

The total optical field may be a superposition of several quasi-monochromatic waves,

$$\tilde{\mathbf{E}}(\mathbf{r},t) = \sum_n \tilde{\mathbf{E}}_n(\mathbf{r},t) = \tfrac{1}{2}\sum_{n>0} \mathbf{E}(\omega_n)e^{-i\omega_n t} + c.c., \tag{2.3}$$

where the complex amplitudes now are denoted $\mathbf{E}(\omega_n) \equiv \mathbf{E}_n(\mathbf{r},t)$. $\mathbf{E}(\omega_n)$ is still a function of the spatial coordinate, but the dependence on $\mathbf{r}$ is not explicitly written out. The complex conjugates are of the form $\mathbf{E}^*(\omega_n)\exp(i\omega_n t)$, which can be seen as terms of negative frequency. The sum can then be written with a more compact notation to sum over both positive and negative frequencies,

$$\tilde{\mathbf{E}}(\mathbf{r},t) = \tfrac{1}{2}\sum_n \mathbf{E}(\omega_n)e^{-i\omega_n t}, \tag{2.4}$$

where $\mathbf{E}(-\omega_n) = \mathbf{E}^*(\omega_n)$.

2.2 Spatial and temporal shapes of $A(\mathbf{r},t)$

If $A(\mathbf{r},t)$ consists of only one quasi-monochromatic wave, the spatial and temporal parts can often be separated, $A(\mathbf{r},t) = A_{\mathbf{r}}(\mathbf{r})A_t(t)$. The simplest spatial shape of $A(\mathbf{r},t)$ is a *plane wave* that extends to infinity in the transverse directions. With the propagation direction defined as the z direction, the spatial part is then written $A_{\mathbf{r}}(\mathbf{r}) = A_{\mathbf{r}}(z)$, where the amplitude is constant for a freely-propagating wave and

has a z dependence if it experiences gain or attenuation. Plane waves serve as first approximations of $A_{\mathbf{r}}(\mathbf{r})$ for collimated laser beams. As the transverse dimensions can be disregarded, the calculations are greatly simplified and analytical solutions can be obtained. A more realistic spatial shape for a free-propagating focused beams is a TEM_{00} beam, where $A_{\mathbf{r}}(\mathbf{r})$ has a Gaussian profile perpendicular to the propagation direction. The characteristics of this beam are determined by the vacuum wavelength, the index of refraction and the beam size at the waist. A beam propagating in the z direction with the beam waist located at $z = 0$ has an amplitude of the form

$$A_{\mathbf{r}}(\rho, z) = A_{\mathbf{r},0} \frac{w_0}{w(z)} \exp\left[-\frac{\rho^2}{w^2(z)} + i\frac{k\rho^2}{2R(z)} + i\zeta(z)\right], \tag{2.5}$$

where ρ is a transverse radial coordinate, $A_{\mathbf{r},0}$ is the on-axis peak amplitude and w_0 is the beam waist radius, defined as the distance where the amplitude of the electric field is $1/e$ times the on-axis value. w_0, λ and n define the *Rayleigh length*, $z_0 = \pi w_0^2 n/\lambda$, being the distance from the beam waist where the beam area is twice as big as at the waist. The beam radius, $w(z)$, the wavefront radius of curvature, $R(z)$ and the Gouy phase, $\zeta(z)$, vary along the beam propagation axis as $w^2(z) = w_0^2[1+(z/z_0)^2]$, $R(z) = z+z_0^2/z$ and $\zeta(z) = -\arctan(z/z_0)$. Away from the waist, the beam spreads due to diffraction and the curvature of the wavefront increases from plane to spherical. In the far field, $z \gg z_0$, the divergence angle of the beam is $\theta \simeq \lambda/(\pi w_0 n)$. The radial amplitude distribution and the beam divergence of a Gaussian beam are illustrated in Fig. 2.1.

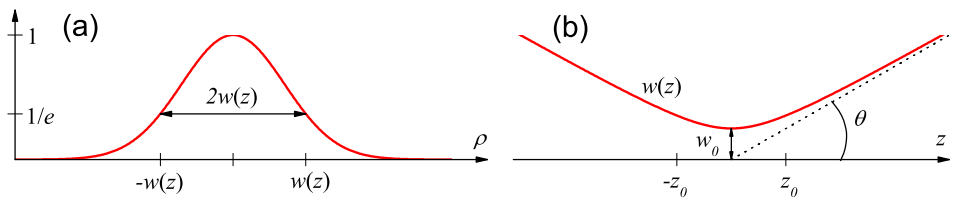

Fig. 2.1: (a) The relative amplitude of a Gaussian beam as function of the transverse coordinate, (b) the beam radius as function of the distance from the beam waist.

In the time domain, the beam amplitude can be either continuous or pulsed. If pulsed, it can often be approximated by a Gaussian pulse with the amplitude

$$A_t(t) = A_{t,0} \exp\left[-2\ln 2\,(t/\Delta t)^2 + i\phi(t)\right], \tag{2.6}$$

where Δt is the pulse width defined as the full width at half maximum (FWHM) of the intensity $I_t(t) \propto |A_t(t)|^2$ and $\phi(t)$ is the phase modulation of the pulse. If the pulse propagates in a medium with refractive index n, the phase velocity is

$$v = \frac{\omega}{k} = \frac{c}{n}, \tag{2.7}$$

whereas the pulse moves with the *group velocity*,

$$v_g = \frac{\partial \omega}{\partial k} = \frac{c}{n_g}, \tag{2.8}$$

where the *group index* in terms of vacuum wavelength is

$$n_g = n - \lambda \frac{\partial n}{\partial \lambda}. \tag{2.9}$$

The spectrum of the pulse generally depends on the particular pulse shape, the pulse width and the phase modulation. With the Fourier transform of $A_t(t)$ defined as

$$A_\omega(\omega) = \mathcal{F}[A_t(t)] = \int_{-\infty}^{\infty} A_t(t) e^{i\omega t} dt, \tag{2.10}$$

the spectral width of the pulse is the width $\Delta\omega$ of $I_\omega(\omega) \propto |A_\omega(\omega)|^2$. For a given temporal width, there is a lower bound of the spectral width, and vice versa. For *linearly-chirped* Gaussian pulses, *i.e.* pulses with a quadratic temporal phase modulation, $\phi(t) = bt^2$, the *time-bandwidth product* of the spectral and temporal widths Δt and $\Delta\omega$, defined as the FWHM widths of $I_t(t)$ and $I_\omega(\omega)$, is given by

$$\Delta t \Delta\omega = 4 \ln 2 \sqrt{1 + (b/a)^2}, \tag{2.11}$$

where $a \equiv 2 \ln 2/(\Delta t)^2$. For a given bandwidth, the chirp broadens the temporal shape of the pulse and moves the high frequencies to the trailing end of the pulse for a *positive chirp* ($b > 0$) and to the leading end for a *negative chirp* ($b < 0$). With no chirp ($b = 0$), $\Delta t \Delta\omega$ is minimised, and the pulse is referred to as *transform limited*.

2.3 Induced electric polarisation

When light propagates in a dielectric material, the electric field exerts forces on the charges in the medium, which results in a separation of positive and negative charges. For electric fields at optical frequencies, the displaced charges are mainly electrons, but ions are displaced to a significant extent for lower frequencies in the far infrared. The separated charges give rise to induced electric dipole moments in the material and the average amount of induced dipole moment per unit volume is referred to as the induced *electric polarisation* of the medium, $\tilde{\boldsymbol{P}}(\mathbf{r}, t)$, which is a function of the external electric field and the *polarisability*, which is the material's ability to displace charges. At low electric field strengths, the material response is to a very good approximation linear, which in principle is the case for light that is not in the form of focused laser beams. When nonlinear effects occur, the induced polarisation can often be expressed as a power series in the applied electric field,

$$\tilde{\mathbf{P}} = \sum_N \tilde{\mathbf{P}}^{(N)} = \tilde{\mathbf{P}}^{(1)} + \tilde{\mathbf{P}}^{NL}, \tag{2.12}$$

where $\tilde{\mathbf{P}}^{(1)}$ is the linear polarisation and the remaining terms are the nonlinear polarisation, $\tilde{\mathbf{P}}^{NL}$. The terms $\tilde{\mathbf{P}}^{(N)}$ contain N factors of the electric field and mixing of N frequencies that are present in $\tilde{\mathbf{E}}$. Normally, the terms with $N \geq 4$ are too weak to be of interest and the power series can be terminated. As for the electric field, $\tilde{\mathbf{P}}^{(N)}$ can be decomposed into complex amplitudes and temporally oscillating terms,

$$\tilde{\mathbf{P}}^{(N)} = \tfrac{1}{2} \sum_n \mathbf{P}^{(N)}(\omega_n) e^{-i\omega_n t}, \tag{2.13}$$

where the sum is over both positive and negative frequencies. The N^{th}-order electric susceptibility, $\boldsymbol{\chi}^{(N)}$, is defined as the quantity that relates the complex amplitude of $\tilde{\mathbf{P}}^{(N)}$ with the complex amplitude of $\tilde{\mathbf{E}}$. With both $\mathbf{E}(\omega_n)$ and $\mathbf{P}^{(N)}(\omega_n)$ being three-dimensional vectors, $\boldsymbol{\chi}^{(N)}$ is a tensor of rank $N+1$ with 3^{N+1} components. All the components are not necessarily independent and the tensors reflect the structural symmetry of the material, meaning that many components are related for highly-symmetric structures, such as cubic crystals. The Cartesian components of the first three terms $\mathbf{P}^{(N)}$ are written,

$$P_j^{(1)}(\omega_\alpha) = \varepsilon_0 \sum_k \chi_{jk}^{(1)}(-\omega_\alpha; \omega_\alpha) E_k(\omega_\alpha), \tag{2.14}$$

$$P_j^{(2)}(\omega_\alpha) = \tfrac{1}{2}\varepsilon_0 \sum_{kl} \sum_{(\beta\gamma)} \chi_{jkl}^{(2)}(-\omega_\alpha; \omega_\beta, \omega_\gamma) E_k(\omega_\beta) E_l(\omega_\gamma), \tag{2.15}$$

$$P_j^{(3)}(\omega_\alpha) = \tfrac{1}{4}\varepsilon_0 \sum_{klm} \sum_{(\beta\gamma\delta)} \chi_{jklm}^{(3)}(-\omega_\alpha; \omega_\beta, \omega_\gamma, \omega_\delta) E_k(\omega_\beta) E_l(\omega_\gamma) E_m(\omega_\delta). \tag{2.16}$$

With this notation, the first arguments in the susceptibilities is minus the frequency of the induced polarisation and all arguments sum to zero. For the second-order case, this means that $\chi_{jkl}^{(2)}(-\omega_\alpha; \omega_\beta, \omega_\gamma)$ induces a part of the polarisation $P_j^{(2)}(\omega_\alpha)$ from the electric fields $E_k(\omega_\beta)$ and $E_l(\omega_\gamma)$, where the frequencies ω_β and ω_γ obey $-\omega_\alpha + \omega_\beta + \omega_\gamma = 0$. This is repeated for all such frequencies by the summation over $(\beta\gamma)$. Then the summation is done over the Cartesian indices k and l to obtain the total polarisation $P_j^{(2)}(\omega_\alpha)$. The $P_j^{(1)}(\omega_\alpha)$ and $P_j^{(3)}(\omega_\alpha)$ terms are obtained analogously, with the difference for $P_j^{(1)}(\omega_\alpha)$ that it only contains the frequencies of the applied electric field. The effects of $\tilde{\mathbf{P}}^{(1)}$, $\tilde{\mathbf{P}}^{(2)}$ and $\tilde{\mathbf{P}}^{(3)}$ are discussed in the three subsequent sections.

Through Maxwell's equations, the nonlinear part of the polarisation enters the wave equation as a source term for frequencies that are not present in the applied electric field. In a homogeneous dielectric medium with no free charges or currents, the wave equation for $\tilde{\mathbf{E}}$ reads

$$\nabla \times \nabla \times \tilde{\mathbf{E}} + \frac{n^2}{c^2} \frac{\partial^2 \tilde{\mathbf{E}}}{\partial t^2} = -\mu_0 \frac{\partial^2 \tilde{\mathbf{P}}^{NL}}{\partial t^2}. \tag{2.17}$$

The wave equation is also fulfilled for each frequency component of $\tilde{\mathbf{E}}$ and the corresponding term in $\tilde{\mathbf{P}}^{NL}$ by making the substitutions $\tilde{\mathbf{E}} \to \frac{1}{2}\mathbf{E}(\omega_n)\exp(-i\omega_n t)$

and $\tilde{\mathbf{P}}^{NL} \rightarrow \frac{1}{2}\mathbf{P}^{NL}(\omega_n)\exp(-i\omega_n t)$. Frequency components that are not initially present in $\tilde{\mathbf{E}}$ can then be generated through the corresponding components in $\tilde{\mathbf{P}}^{NL}$. For monochromatic plane waves travelling in the z direction, Eq. (2.17) simplifies to

$$\left[\frac{d^2A(\omega_n)}{dz^2} + 2ik_n\frac{dA(\omega_n)}{dz}\right]e^{ik_n z} = -\mu_0\omega_n^2 P^{NL}(\omega_n), \tag{2.18}$$

for each frequency component ω_n present in $\tilde{\mathbf{P}}^{NL}$. Often the *slowly-varying envelope approximation* (SVEA) can be used and the second-order derivative in Eq. (2.18) is neglected, which requires that $|d^2A(\omega_n)/dz^2| \ll |2k_n dA(\omega_n)/dz|$.

2.4 Linear optics

Linear optical phenomena are related to the material's index of refraction and absorption coefficient. The phase velocity of the light is slowed down by a factor of $1/n$ and around certain frequencies absorption occurs. The Cartesian components of the induced polarisation are then given by Eq. (2.14), where $\chi^{(1)}_{jk}(-\omega_\alpha;\omega_\alpha)$ often is written $\chi^{(1)}_{jk}(\omega_\alpha)$. In glasses, liquids, gases and cubic crystals, the linear susceptibility tensor is isotropic, $\chi^{(1)}_{jk}(\omega) = \chi^{(1)}(\omega)\delta_{jk}$, which means that the tensor can be replaced by the scalar quantity $\chi^{(1)}(\omega)$, whose real and imaginary parts are related to the index of refraction, $n(\omega)$, and to the absorption coefficient with respect to intensity, $\alpha(\omega)$, as

$$n(\omega) = \sqrt{1 + \mathrm{Re}\big[\chi^{(1)}(\omega)\big]}, \tag{2.19}$$

$$\alpha(\omega) = \frac{\omega \mathrm{Im}\big[\chi^{(1)}(\omega)\big]}{n(\omega)c}. \tag{2.20}$$

For non-cubic crystals, as for orthorhombic $KTiOPO_4$ (KTP) and the tetragonal and monoclinic double tungstates studied in this thesis, the tensorial nature of $\boldsymbol{\chi}^{(1)}$ needs to be taken into account and the expression for the refractive index becomes more complicated. At frequencies where the material is transparent, the components of $\boldsymbol{\chi}^{(1)}$ are real and it can be shown that the tensor is symmetric, meaning that $\chi^{(1)}_{jk}(\omega) = \chi^{(1)}_{kj}(\omega)$ in any matrix representation. The eigenvalues of a symmetric matrix are always real and the eigenvectors corresponding to different eigenvalues are orthogonal and define the *principal coordinate axes*. The Cartesian components of any susceptibility tensor are here always given in the principal coordinate system. In the basis of eigenvectors, the matrix representing $\boldsymbol{\chi}^{(1)}$ is diagonal. Beams that are polarised along one of the principal axes $j \in \{x, y, z\}$ experience a refractive index of

$$n_j = \sqrt{1 + \chi^{(1)}_{jj}}, \tag{2.21}$$

which is called a principal index of refraction. In isotropic media, the three principal indices are equal, $n_x = n_y = n_z$. Crystals belonging to the tetragonal, hexagonal

and trigonal crystal classes are referred to as uniaxial crystals, for which two of the principal indices coincide, *e.g.* $n_x = n_y \neq n_z$. The degenerate value is referred to as the *ordinary* index, n_o, whereas the other index is referred to as the *extraordinary* index, n_e. For orthorhombic, monoclinic and triclinic crystal classes, the three principal indices are distinct and the crystals are referred to as biaxial. The principal indices, and the corresponding principal axes x, y and z, are conventionally labelled so that $n_x < n_y < n_z$. An alternative notation for the principal indices in biaxial crystals is $n_p < n_m < n_g$, with the corresponding principal axes N_p, N_m and N_g, where p, m and g stand for *petite*, *moyen* and *grand*, being French for small, intermediate and large, respectively. In orthorhombic and tetragonal crystals, the principal axes always coincide with the crystallographic axes. In monoclinic crystals, one principal axis coincides with the crystallographic **b** axis, *i.e.* the crystallographic axis that is perpendicular to the other two in a monoclinic system.

In uniaxial and biaxial crystals, the index of refraction experienced by a wave can, at least for one of two orthogonal polarisation directions, be altered by changing the propagation direction in the crystal. This is important for nonlinear applications where *phase matching* is necessary in order to achieve efficient energy exchange between waves of different frequencies, which is further explained in the next section. The index of refraction experienced by a wave that propagates in a direction with unit vector $\hat{\mathbf{k}} = \sin\theta\cos\varphi\ \hat{\mathbf{e}}_x + \sin\theta\sin\varphi\ \hat{\mathbf{e}}_y + \cos\theta\ \hat{\mathbf{e}}_z$ is in biaxial crystals given by a solution of

$$\sin^2\theta\cos^2\varphi\frac{n_x^2}{n^2 - n_x^2} + \sin^2\theta\sin^2\varphi\frac{n_y^2}{n^2 - n_y^2} + \cos^2\theta\frac{n_z^2}{n^2 - n_z^2} = 0. \tag{2.22}$$

There are two possible solutions, n_1 and n_2, for each direction of $\hat{\mathbf{k}}$, corresponding to waves with orthogonal polarisations. A wave containing components of both polarisations will be divided into two waves that propagate at different phase velocities. Both indices are bound between the lowest and the highest principal indices, $n_x < n_1, n_2 < n_z$.

In uniaxial crystals, the situation is simplified. The ordinary index is independent of the propagation direction and the extraordinary index depends on the angle θ between the propagation direction and the non-degenerate principal axis as

$$\frac{1}{n_e^2(\theta)} = \frac{\cos^2\theta}{n_o^2} + \frac{\sin^2\theta}{n_e^2}. \tag{2.23}$$

Dispersion

According to Eq. (2.20) and Eq. (2.19), the index of refraction and the absorption coefficient are given as functions of the real and imaginary parts of $\chi^{(1)}$, respectively. $\mathrm{Re}\big[\chi^{(1)}(\omega)\big]$ and $\mathrm{Im}\big[\chi^{(1)}(\omega)\big]$ are not independent, but are related through the *Kramers-Kronig relations*, with the consequence that the index of refraction

predominantly changes around frequencies where the material is absorbing. Between absorption lines, the index of refraction can be mathematically modelled as a *Sellmeier expansion* of the form

$$n^2(\lambda) = 1 + \sum_j \frac{B_j \lambda^2}{\lambda^2 - C_j^2}, \tag{2.24}$$

where B_j is related to the strength of the absorption peak at the wavelength C_j. Slight variations of this form of $n^2(\lambda)$ are common, *e.g.* with a correction term proportional to λ^2. To accurately model the refractive index in the visible and near-infrared wavelength regions, it is normally enough to model with one or two absorption lines in the ultraviolet and one in the mid or far infrared. The absorption in the UV is due to electronic resonances and the absorption in the far infrared is caused by lattice resonances. Between absorption lines, the refractive index increases with ω (decreases with λ), which is known as *normal dispersion*. The opposite behaviour, which occurs around the absorption lines is called *anomalous dispersion*. A schematic sketch of the refractive index between two absorption lines in shown in Fig. 2.2. In the UV, absorption occurs for frequencies larger than the material's bandgap, as light at those frequencies generate free electrons in the material, which is schematically illustrated with the extension of the absorption line towards higher frequencies.

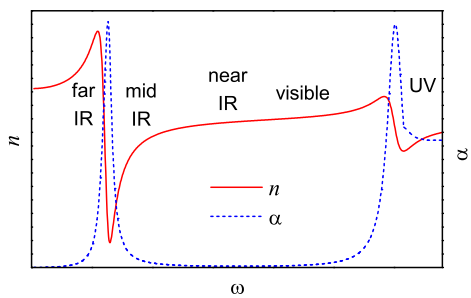

Fig. 2.2: A schematic graph showing one absorption line in the ultraviolet and one in the far infrared. Variation in n predominantly occurs around the absorption lines. Between the lines, n increases with ω (decreases with λ).

2.5 Second-order nonlinear interactions

At sufficiently high field strengths, the nonlinear terms in the induced polarisation cannot be disregarded. This section deals with second-order nonlinear interactions, also referred to as *three-wave mixing*, which originate from $\tilde{\mathbf{P}}^{(2)}$. The expression for its Cartesian components, Eq. (2.15), contains a summation over $(\beta\gamma)$. For

each pair $(\beta\gamma)$, there is either one or two contributions to ω_α, depending on if the fields at ω_γ and ω_β are distinguishable. The sum can be written as a sum over all distinct pairs $\beta\gamma$ obeying $\omega_\alpha = \omega_\beta + \omega_\gamma$ times a *degeneracy factor*, $D^{(2)}$,

$$P_j^{(2)}(\omega_\alpha) = \tfrac{1}{2}\varepsilon_0 D^{(2)} \sum_{\beta\gamma} \sum_{kl} \chi_{jkl}^{(2)}(-\omega_\alpha; \omega_\beta, \omega_\gamma) E_k(\omega_\beta) E_l(\omega_\gamma). \tag{2.25}$$

$D^{(2)}$ is the number of distinct permutations of the fields at ω_β and ω_γ, meaning that $D^{(2)} = 1$ if $E_k(\omega_\beta)$ and $E_l(\omega_\gamma)$ are taken from the same beam and have the same frequency, and else $D^{(2)} = 2$. Positive and negative frequencies are counted as distinct. If the electric field contains the positive frequencies $\omega_1 < \omega_2$, together with their negative counterparts as the fields are real, the second-order polarisation contains all frequencies ω_α of the form

$$\omega_\alpha = \sigma_\beta \omega_\beta + \sigma_\gamma \omega_\gamma, \tag{2.26}$$

where $\sigma_\beta, \sigma_\gamma \in \{-1, 1\}$ and $\omega_\beta, \omega_\gamma \in \{\omega_1, \omega_2\}$. These components of $\tilde{\mathbf{P}}^{(2)}$ are used for *second-harmonic generation* (SHG) at $2\omega_1$ and $2\omega_2$, *sum-frequency generation* (SFG) at $\omega_1 + \omega_2$, *difference-frequency generation* (DFG) at $\omega_2 - \omega_1$ and *optical rectification* (OR) at zero frequency. Second-order nonlinear media are commonly used for frequency conversions of laser beams and these nonlinear effects were demonstrated shortly after the invention of the laser [1]. SHG was first demonstrated in 1961 [9], where a pulsed ruby laser was frequency doubled in quartz. Later that year, SFG was realised by mixing of beams from two ruby lasers of slightly different frequencies in triglycine sulfate [10]. DFG was first demonstrated by frequency mixing between axial modes in a ruby laser in CdSe [11].

Symmetries of $\chi_{jkl}^{(2)}$

There are 27 components $\chi_{jkl}^{(2)}$ for each involved frequency set $(-\omega_\alpha; \omega_\beta, \omega_\gamma)$, but due to different symmetry arguments, not all of these are independent. Since $\tilde{\mathbf{E}}$ and $\tilde{\mathbf{P}}^{(2)}$ are real quantities, the complex amplitudes at a positive frequency is related to the complex amplitude at its negative counterpart. This leads to the general relation that complex conjugation of $\chi_{jkl}^{(2)}$ inverts all the signs of the frequency arguments,

$$\chi_{jkl}^{(2)}(-\omega_\alpha; \omega_\beta, \omega_\gamma) = \chi_{jkl}^{(2)*}(\omega_\alpha; -\omega_\beta, -\omega_\gamma). \tag{2.27}$$

Two contributions to $P_j^{(2)}(\omega_\alpha)$ in Eq. (2.25) are $\chi_{jkl}^{(2)}(-\omega_\alpha; \omega_\beta, \omega_\gamma) E_k(\omega_\beta) E_l(\omega_\gamma)$ and $\chi_{jlk}^{(2)}(-\omega_\alpha; \omega_\gamma, \omega_\beta) E_l(\omega_\gamma) E_k(\omega_\beta)$. Both these terms use the same fields and only their sum has a physical meaning. It is then convenient to split the total contribution in two equal terms,

$$\chi_{jkl}^{(2)}(-\omega_\alpha; \omega_\beta, \omega_\gamma) = \chi_{jlk}^{(2)}(-\omega_\alpha; \omega_\gamma, \omega_\beta), \tag{2.28}$$

which is known as *intrinsic permutation symmetry*. This symmetry relation enables the introduction of the degeneracy factor in Eq. (2.25). When the involved frequencies are far from absorption resonances, additional symmetry relations apply. When there is no absorption, the energy density stored in the second-order polarisation is a constant quantity and it can be shown that the susceptibility then is real and possesses *full permutation symmetry*, meaning that the indices can be permuted freely, as long as the frequency components also are permuted in the same way, *i.e.*,

$$\chi^{(2)}_{jkl}(-\omega_\alpha;\omega_\beta,\omega_\gamma) = \chi^{(2)}_{kjl}(\omega_\beta;-\omega_\alpha,\omega_\gamma) = \chi^{(2)}_{lkj}(\omega_\gamma;\omega_\beta,-\omega_\alpha) = \dots \tag{2.29}$$

Furthermore, the dispersion in the nonlinear susceptibility is low when the frequencies are well below resonances. Then *Kleinman symmetry* applies, meaning that as long as there is no resonance between the involved frequencies, the frequencies can be permuted without permuting the Cartesian indices of the susceptibility,

$$\chi^{(2)}_{jkl}(-\omega_\alpha;\omega_\beta,\omega_\gamma) = \chi^{(2)}_{jkl}(\omega_\beta;-\omega_\alpha,\omega_\gamma) = \chi^{(2)}_{jkl}(\omega_\gamma;\omega_\beta,-\omega_\alpha) = \dots \tag{2.30}$$

Conversely, using the full permutation symmetry, the indices can be freely permuted without permuting the frequencies,

$$\chi^{(2)}_{jkl}(-\omega_\alpha;\omega_\beta,\omega_\gamma) = \chi^{(2)}_{kjl}(-\omega_\alpha;\omega_\beta,\omega_\gamma) = \chi^{(2)}_{lkj}(-\omega_\alpha;\omega_\beta,\omega_\gamma) = \dots \tag{2.31}$$

The frequency arguments can then be omitted if all interacting frequencies are between the same two resonances. Since most nonlinear interactions for frequency conversions of laser beams take place in these frequency regions, all symmetry relations often apply. The dispersion in the second-order susceptibility can be estimated with the use of the semi-empirical *Miller's rule*, which relates the second-order susceptibility to the the first-order susceptibility,

$$\Delta_{jkl} = \frac{\chi^{(2)}_{jkl}(-\omega_\alpha;\omega_\beta,\omega_\gamma)}{\chi^{(1)}_{jj}(-\omega_\alpha;\omega_\alpha)\chi^{(1)}_{kk}(-\omega_\beta;\omega_\beta)\chi^{(1)}_{ll}(-\omega_\gamma;\omega_\gamma)}, \tag{2.32}$$

where Δ_{jkl} is approximately constant. All relations, Eq. (2.27) - Eq. (2.32), can be generalised to the susceptibility of any order.

Further symmetry relations can be found by considering the structural symmetry of the medium, which for most crystal classes relate several of the tensor elements and many can be deduced to be zero. In fact, for *centrosymmetric media*, like glasses and cubic crystals belonging to symmetry class 432, all components $\chi^{(2)}_{jkl}$ are identically zero and such materials do not have any second-order polarisation response in the bulk.

For the second-order case, the full permutation symmetry reduces the 27 components $\chi^{(2)}_{jkl}$ to 18 independent elements, which are further reduced to 10 with Kleinman symmetry. The tensor is often written in *contracted form*, where the two last indices are replaced by one,

$$d_{jm} = \tfrac{1}{2}\chi^{(2)}_{jkl}. \tag{2.33}$$

The Cartesian indices are written as numbers rather than x, y and z with the following substitution:

$$\begin{array}{cccccccccccccccc} j & = & x & y & z, & kl & = & xx & yy & zz & yz & zy & xz & zx & xy & yx \\ j & = & 1 & 2 & 3, & m & = & 1 & 2 & 3 & 4 & 4 & 5 & 5 & 6 & 6 \end{array} . \tag{2.34}$$

The contracted tensor can be represented as 3×6 matrix, which has up to 10 independent components when Kleinman symmetry is valid,

$$\mathbf{d} = \begin{pmatrix} d_{11} & d_{12} & d_{13} & d_{14} & d_{15} & d_{16} \\ d_{16} & d_{22} & d_{23} & d_{24} & d_{14} & d_{12} \\ d_{15} & d_{24} & d_{33} & d_{23} & d_{13} & d_{14} \end{pmatrix}, \tag{2.35}$$

and the second-order polarisation at ω_α generated by one pair $\beta\gamma$ obeying $\omega_\alpha = \omega_\beta + \omega_\gamma$ can be written in the following compact form:

$$\begin{pmatrix} P_x^{(2)}(\omega_\alpha) \\ P_y^{(2)}(\omega_\alpha) \\ P_z^{(2)}(\omega_\alpha) \end{pmatrix} = \varepsilon_0 D^{(2)} \mathbf{d} \begin{pmatrix} E_x(\omega_\beta)E_x(\omega_\gamma) \\ E_y(\omega_\beta)E_y(\omega_\gamma) \\ E_z(\omega_\beta)E_z(\omega_\gamma) \\ E_y(\omega_\beta)E_z(\omega_\gamma) + E_z(\omega_\beta)E_y(\omega_\gamma) \\ E_x(\omega_\beta)E_z(\omega_\gamma) + E_z(\omega_\beta)E_x(\omega_\gamma) \\ E_x(\omega_\beta)E_y(\omega_\gamma) + E_y(\omega_\beta)E_x(\omega_\gamma) \end{pmatrix}. \tag{2.36}$$

As an example, if the fields $\mathbf{E}(\omega_\beta)$ and $\mathbf{E}(\omega_\gamma)$ both are polarised in the z direction, the second-order polarisation is

$$\begin{pmatrix} P_x^{(2)}(\omega_\alpha) \\ P_y^{(2)}(\omega_\alpha) \\ P_z^{(2)}(\omega_\alpha) \end{pmatrix} = \varepsilon_0 D^{(2)} \begin{pmatrix} d_{13}E_z(\omega_\beta)E_z(\omega_\gamma) \\ d_{23}E_z(\omega_\beta)E_z(\omega_\gamma) \\ d_{33}E_z(\omega_\beta)E_z(\omega_\gamma) \end{pmatrix}. \tag{2.37}$$

For fixed propagation and polarisation directions of the electric field, the magnitude of the second-order polarisation may be written in terms of the magnitudes of the electric fields,

$$P(\omega_\alpha) = \varepsilon_0 D^{(2)} d_{eff} E(\omega_\beta) E(\omega_\gamma), \tag{2.38}$$

where d_{eff} is the *effective nonlinearity*, which is a function of the components of $\mathbf{d}$ and the propagation angles and polarisation directions of the involved fields. In many cases d_{eff} is a single component d_{jm} with trigonometric functions of the propagation angles θ and φ. In KTP, $d_{13} = d_{23} = 0$, meaning that Eq. (2.37) is of the form of Eq. (2.38) with $d_{eff} = d_{33}$ when $\mathbf{E}(\omega_\beta)$ and $\mathbf{E}(\omega_\gamma)$ are z polarised.

Phase matching

Solving the wave equation, Eq. (2.18), for fields propagating in the z direction at the three distinct positive frequencies ω_1, ω_2 and ω_3, where $\omega_3 = \omega_1 + \omega_2$, leads to a

set of three coupled equations, which in the slowly-varying envelope approximation are of the following form:

$$\frac{dA_1}{dz} = i\frac{\omega_1}{n_1 c} d_{eff} A_3 A_2^* e^{i\Delta kz}, \tag{2.39}$$

$$\frac{dA_2}{dz} = i\frac{\omega_2}{n_2 c} d_{eff} A_3 A_1^* e^{i\Delta kz}, \tag{2.40}$$

$$\frac{dA_3}{dz} = i\frac{\omega_3}{n_3 c} d_{eff} A_1 A_2 e^{-i\Delta kz}, \tag{2.41}$$

where $A_n \equiv A(\omega_n)$, $A_n^* \equiv A(-\omega_n)$ and $n_n \equiv n(\omega_n)$. The wave-vector mismatch, $\Delta k \equiv k_3 - k_1 - k_2 = (\omega_3 n_3 - \omega_2 n_2 - \omega_1 n_1)/c$, is normally nonzero due to dispersion in the refractive index of the nonlinear medium. In the degenerate case, $\omega_1 = \omega_2 = \omega_3/2$, Eq. (2.39) and Eq. (2.40) are merged into one equation and the right hand side of Eq. (2.41) is multiplied by 1/2, since $D^{(2)}$ then is reduced from 2 to 1. The coupled equations describe how energy is exchanged between the fields of different frequencies due to the nonlinear interaction. It can be deduced that the number of photons created or lost at ω_3 is equal to the number of photons lost or created at ω_1, and also at ω_2, which is known as the *Manley-Rowe relations*:

$$\frac{1}{\omega_3}\frac{dI_3}{dz} = -\frac{1}{\omega_1}\frac{dI_1}{dz} = -\frac{1}{\omega_2}\frac{dI_2}{dz}. \tag{2.42}$$

Normally, fields at two of the three frequencies are initially present and generate a field at the third frequency through sum-frequency generation or difference-frequency generation. For *optical parametric generation* (OPG) and *optical parametric oscillation* (OPO), only one field is initially present and the other fields start from quantum noise. For weak interactions, the decrease in the amplitudes of the input fields can as a first approximation be disregarded. This leads to easy calculations and some results that are qualitatively correct even for high conversion efficiencies, such as the importance of *phase matching*. As an example, sum-frequency generation is considered where a weak field at $\omega_3 = \omega_1 + \omega_2$ is generated from the fields at ω_1 and ω_2 in a nonlinear medium of length L. With A_1 and A_2 approximately constant, Eq. (2.41) can be directly integrated to obtain the amplitude of A_3 at $z = L$, which results in the following sum-frequency intensity at the end of the crystal:

$$I_3(L) = \frac{2\omega_3^2 I_1 I_2 d_{eff}^2 L^2}{\varepsilon_0 c^3 n_1 n_2 n_3} \mathrm{sinc}^2\left(\frac{\Delta kL}{2}\right), \tag{2.43}$$

where $\mathrm{sinc}(x) \equiv \sin(x)/x$. Apart from being proportional to the product of the input intensities and the square of the effective nonlinearity, the wave-vector mismatch limits the crystal length for which an additional increase in the output intensity I_3 is generated through the factor $\mathrm{sinc}^2(\Delta kL/2)$. A graph of $\mathrm{sinc}^2(\Delta kL/2)$ as function of $\Delta kL/2$ is shown in Fig. 2.3. The value of the function is reduced to 1/2 for $|\Delta kL/2| \simeq 1.39$ and the first zeros are located at at $|\Delta kL/2| = \pi$.

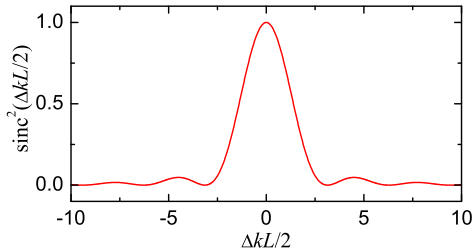

Fig. 2.3: $\mathrm{sinc}^2(\Delta kL/2)$ as function of $\Delta kL/2$.

The total electric field at a point z' is a superposition of the fields that were generated at earlier times at $z < z'$ and have propagated to z' at the given time. Unless $\Delta k = 0$, these fields are not in phase at z' and their interference is not fully constructive. After one *coherence length*,

$$L_c = \frac{\pi}{|\Delta k|}, \tag{2.44}$$

the interference starts being destructive and the field amplitude decreases and power starts flowing back from the field at ω_3 to the fields that generate the nonlinear polarisation at ω_3, *i.e.* to the fields at ω_1 and ω_2. The amplitude at ω_3 goes to zero after $2L_c$. For interactions with z-polarised light in KTP, the numerical value of L_c ranges from $\sim$1 μm for interactions in the UV [24] to $\sim$20 μm for interactions in the infrared [25], at the same time as the crystals where the interactions take place normally have a length of several millimetres, *i.e.* hundreds of coherence lengths or more. For an efficient interaction where the whole crystal length is used, it is therefore necessary to achieve *phase matching*, $\Delta k = 0$. In a homogeneous medium, this can possibly be done in anisotropic crystals where one of the interacting waves has its polarisation direction orthogonal to that of the other two. The birefringence, *e.g.* $|n_e(\lambda) - n_o(\lambda)|$ in uniaxial crystals, needs to be large enough to compensate for the dispersion in the refractive index. Once the principal refractive indices are known as functions of the wavelength, the propagation angles in the crystal are chosen in accordance with Eq. (2.23) for uniaxial crystals and Eq. (2.22) for biaxial crystals to adjust the lengths of the wave vectors. This way of achieving $\Delta k = 0$ is referred to as *birefringent phase matching* (BPM) and was first considered in 1962 [26, 27]. The waves then have to interact through a nondiagonal component d_{jm}, *i.e.* not through d_{11}, d_{22} or d_{33}, as these components couple fields that all have the same polarisation. If $\mathbf{E}(\omega_3)$, the field at the highest frequency, has its polarisation direction orthogonal to those of $\mathbf{E}(\omega_1)$ and $\mathbf{E}(\omega_2)$, the phase matching is referred to as type I. If the polarisation of $\mathbf{E}(\omega_3)$ is parallel to one of $\mathbf{E}(\omega_1)$ and $\mathbf{E}(\omega_2)$, and orthogonal to the other, the phase matching is referred to as type II. In the case that all three fields are polarised in the same direction, the phase matching is referred to as type 0. Even though the crystal birefringence cannot be used for

phase matching of type-0 interactions, they can be made efficient through *quasi-phase matching*, which is explained in the next subsection. For any type of phase matching, the interacting waves may propagate in noncollinear directions, obeying the vectorial relation $\Delta\mathbf{k} = \mathbf{k}_3 - \mathbf{k}_1 - \mathbf{k}_2 = \mathbf{0}$.

The interaction length for BPM is sometimes limited by *Poynting vector walk-off*, caused by the fact that a beam propagates in the direction of the energy flow given by $\tilde{\mathbf{E}} \times \tilde{\mathbf{H}}$, where $\tilde{\mathbf{H}}$ is the magnetic field. This direction is in anisotropic crystals not necessarily parallel to the propagation direction of the phase fronts, given by the wave vector $\mathbf{k}$, which points in the direction of $(\tilde{\mathbf{E}} + \tilde{\mathbf{P}}/\varepsilon_0) \times \tilde{\mathbf{H}}$. $\tilde{\mathbf{P}}$ and $\tilde{\mathbf{E}}$ only point in the same direction when $\tilde{\mathbf{E}}$ oscillates along a principal axis. Two interacting beams that have orthogonal polarisations, *e.g.* where one is polarised parallel to a principal axis and the other is not, will hence be spatially separated as the beams propagate and the interaction length is thereby reduced, especially for tightly focused beams. In uniaxial crystals, the walk-off angle, ρ, for an extraordinary beam is given by

$$\tan\rho = \frac{n_e^2(\theta)}{2}\left[\frac{1}{n_e^2} - \frac{1}{n_o^2}\right]\sin(2\theta), \tag{2.45}$$

which increases with a larger birefringence and is maximised around $\theta = \pi/4$. When the walk-off angle is zero for all extraordinary beams ($\theta = \pi/2$), the phase matching is referred to as *noncritical*, as opposed to *critical* for all other values of θ. The interacting wavelengths where noncritical phase matching is possible are given by the dispersion in the nonlinear medium and can be slightly varied by changing the crystal temperature or the crystal composition [28].

Engineerable media: quasi-phase matching

As previously explained, the electric field amplitude builds up in the first coherence length and then the power flows back into the waves that created the nonlinear polarisation. This could be prevented if a relative phase shift between the polarisation and the electric field were to be introduced at $z = L_c$. A periodic π phase shift, with the periodicity of L_c, assures that the interference of the electric field generated at different positions in the crystal always is partially constructive and the whole crystal length can be used for the interaction. This is referred to as *quasi-phase matching* (QPM) and was first proposed in 1962 [14] and demonstrated in 1966 [29] by frequency doubling of a CO_2 laser in non-birefringent ZnS and GaAs. The phase shifts were introduced by periodic total internal reflection in plane-parallel slabs, making the phase difference obtain partially constructive values throughout the crystals. Another way of achieving QPM is to periodically structure the nonlinear coefficient. This was first done by bonding crystal plates of different orientations into a stack, where two consecutive plates had an opposite sign of the nonlinear coefficient [30]. This method has the disadvantage of Fresnel-reflection losses between the plates and the plate thickness can normally not be

made as thin as a coherence length. Instead, the real breakthrough for QPM had to wait for the periodic polarisation switching by *electric-field poling* in ferroelectric materials. Periodic electric-field poling was first demonstrated for QPM applications in 1993 by the generation of blue light through quasi-phase-matched SHG in a waveguide in $LiNbO_3$ [31]. This was later followed by bulk QPM interactions in periodically-poled $LiNbO_3$ [32] and $KTiOPO_4$ [33]. Today, the ferroelectric crystals are the most common QPM materials and the periodicities obtained in $KTiOPO_4$ are below 1 μm [16, 34, 35]. Another technique for QPM is *orientation patterning* of semiconductors, meaning that they are periodically grown in different crystal directions and the sign of d_{eff} is thereby periodically inverted. This was first used for QPM applications in GaAs [36] and later in GaN [37, 38].

With QPM, the efficiency of the nonlinear interactions no longer relies on the birefringent and dispersive properties of the nonlinear medium, but the periodicity of the polarisation phase shift can be designed to match the wave-vector mismatch of any nonlinear process within the transparency range of the medium. Furthermore, novel nonlinear devices can be constructed, such as counterpropagating devices, where the natural birefringence of any material is too low to phase match interactions with counterpropagating waves of similar frequencies. QPM with periodicities of the order of the interacting wavelengths has been used for SHG in the backward direction [35, 39], electrically-controlled Bragg reflectors [34], and, of special interest for this thesis, for the realisation of mirrorless optical parametric oscillators [16].

With a spatially-varying nonlinear coefficient, $d_{eff}(z)$, the z dependence needs to be included in Eq. (2.39) - Eq. (2.41). If $d_{eff}(z)$ has a fixed magnitude, but periodically changes its sign along the propagation direction, the resulting equations can essentially be cast into the same form as Eq. (2.39) - Eq. (2.41) with a constant d_{eff}, if the definitions of Δk and d_{eff} are modified [40]. By writing $d_{eff}(z) = d_{eff} f(z)$, where $f(z)$ changes from 1 to -1 and has the periodicity Λ, it can be expanded in a Fourier series,

$$d_{eff}(z) = d_{eff} \sum_{m=-\infty}^{\infty} G_m e^{iK_m z}, \tag{2.46}$$

where the spatial frequencies K_m are given by

$$K_m = \frac{2\pi m}{\Lambda} \tag{2.47}$$

and the Fourier coefficients G_m are

$$G_m = \frac{1}{\Lambda} \int_0^{\Lambda} f(z) e^{-iK_m z} dz. \tag{2.48}$$

For instance, by the use of Eq. (2.46), Eq. (2.41) becomes

$$\frac{dA_3}{dz} = i \frac{\omega_3}{n_3 c} A_1 A_2 d_{eff} \sum_{m=-\infty}^{\infty} G_m e^{-i(\Delta k - K_m)z}. \tag{2.49}$$

All terms in the sum give rise to oscillatory terms that after integration average out to zero, unless the modulation period Λ adds a spatial phase shift that has been designed to match that caused by the dispersion between the interacting waves, meaning that for $m = m'$, $\Delta k - K_{m'} \simeq 0$. The amplitude of that term grows linearly with z and its contribution dominates over the oscillating terms with $m \neq m'$, meaning that the sum can be approximated with the m' term. Eq. (2.39) - Eq. (2.41) are then of their original forms, but with Δk and d_{eff} substituted by

$$\Delta k_Q = \Delta k - K_{m'} \tag{2.50}$$

and

$$d_{eff,Q} = d_{eff} G_{m'}. \tag{2.51}$$

$K_{m'}$ is referred to as the magnitude of the *grating vector* for m'^{th}-order QPM. For further discussion in this text, the subscript Q for quasi-phase matching is mostly omitted and the grating vector is denoted $\mathbf{K}_G$. The other values of m give rise to oscillatory terms that slightly modify the field amplitudes within each coherence length, but average out to zero after m' coherence lengths. For a periodic sign change of d_{eff} with a *duty cycle* $D = l/\Lambda$, as defined in Fig. 2.4, the Fourier coefficients are

$$G_m = \frac{2}{m\pi} \sin(m\pi D)\, e^{-im\pi D}, \tag{2.52}$$

where only the amplitudes of the coefficients are important. In the ideal case for odd-order QPM, $D = 1/2$ and the magnitudes of the odd coefficients are maximised to $2/(m\pi)$ and the even ones are zero. As the odd coefficients scale as $1/m$, it is desirable to use $m = 1$ in order to minimise the reduction in $|d_{eff,Q}|$.

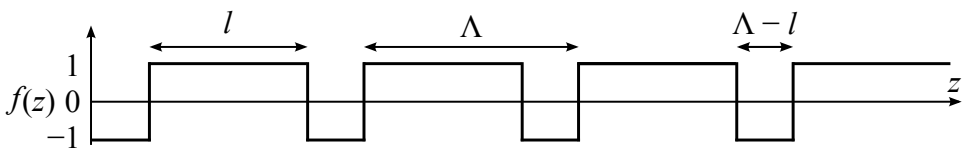

Fig. 2.4: The duty cycle is defined as $D = l/\Lambda$

Even though quasi-phase matching reduces the effective nonlinearity by at least a factor $2/\pi$, the resulting nonlinearity may still be larger compared to in birefringent phase matching, since all nonzero components d_{jm} are accessible. Materials that lack birefringence, such as GaAs, but have a high nonlinearity can be used for QPM but not for BPM. For other materials, such as $LiNbO_3$ and $KTiOPO_4$, the largest component is the diagonal component d_{33}, which is not accessible through BPM since all interacting waves then are polarised in the z direction. In fact, $2d_{33}/\pi$ is significantly larger than any of the other components d_{jm} for these materials. The possibility to use all waves with the same polarisation, polarised along a principal axis, makes the phase matching noncritical and eliminates Poynting vector walk-off

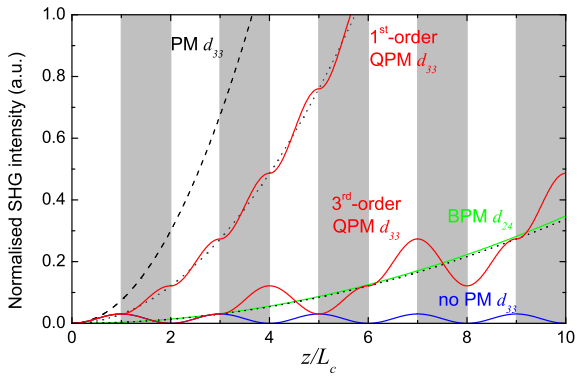

Fig. 2.5: The relative intensity of the second harmonic as function of the propagation distance in KTP, expressed in coherence lengths for the non-phase-matched and QPM interactions. The type-0 QPM interactions are compared with perfect phase matching, no phase matching and type-II BPM with d_{24}.

that reduces the interaction length in BPM. Therefore, if possible, QPM is often used for type-0 interactions.

A comparison of the intensity of SHG in KTP for different phase-matching techniques is illustrated in Fig. 2.5. Using the largest coefficient, $d_{33} = 16.9$ pm/V [41], type-0 QPM of 1^{st} and 3^{rd} order are compared with the non-phase-matched case and the case of perfect phase matching, which however cannot be achieved due to dispersion. The QPM is also compared with a type-II interaction with $d_{24} = 3.64$ pm/V [41], where $d_{eff} \leq d_{24}$ and the exact value depends on trigonometric functions of the propagation angle, θ, relative to the x axis. It is assumed in the graph that $\theta = 0$, which leads to $d_{eff} = d_{24}$, which is slightly larger than d_{eff} for 3^{rd}-order QPM with d_{33}. For the QPM cases, the effects of the non-phase-matched terms give rise to the modulations between the coherence lengths. If only the Fourier term with the m-value fulfilling $\Delta k_Q = 0$ were to be plotted, the QPM intensities would follow the dotted lines and the modulations between the coherence lengths disappear. For QPM calculations, the modulations are normally disregarded.

Optical parametric oscillators

Through a second-order nonlinear process, it is possible to generate two new frequencies from a pump wave containing only a single frequency. This is referred to as *optical parametric generation* (OPG), where a pump photon of frequency ω_p is spontaneously down-converted into a pair of parametric photons of frequencies ω_s and ω_i. These photons are referred to as *signal* and *idler*, respectively, where, by definition, the signal photon is the one in the pair with the higher energy, $\omega_s > \omega_i$.

Both energies add up to that of the pump photon,

$$\omega_p = \omega_s + \omega_i. \tag{2.53}$$

The spontaneous down-conversion is a purely quantum-mechanical process where the pump photons interact with quantum fluctuations at either of the signal or the idler frequencies through the second-order polarisation. Once the down-conversion has started, other pump photons may interact with the generated photons at ω_s or ω_i to create a new pair at the same frequencies through difference-frequency generation (DFG), that in turn can interact with other pump photons and coherently stimulate the down-conversion process. In accordance with energy conservation alone, the division of a pump photon into signal and idler photons can be done in an infinite number of ways by varying the signal frequency to $\omega_s + \Delta\omega$ and the idler frequency to $\omega_i - \Delta\omega$. The polarisations and propagation directions of the generated photons can be arbitrary. However, the interactions with the pump are only efficient for the signal-idler pairs of frequencies and propagation directions where the phase mismatch is small,

$$\Delta\mathbf{k} = \mathbf{k}_p - \mathbf{k}_s - \mathbf{k}_i \underbrace{-\mathbf{K_G}}_{\text{if QPM}} \simeq \mathbf{0}, \tag{2.54}$$

where the grating vector $\mathbf{K_G}$ is included if d_{eff} is periodically structured. The amplitudes of the pump, signal and idler waves evolve in accordance with Eq. (2.39) - Eq. (2.41) where $\omega_1 = \omega_i$, $\omega_2 = \omega_s$ and $\omega_3 = \omega_p$. As quantum fluctuations always are present, the signal and idler cannot strictly start from zero, but initially have a very small amplitude and a random phase. In the nondepleted-pump approximation, the signal (or idler) intensity increases during the propagation length L as

$$\frac{I_s(L)}{I_s(0)} = 1 + (\Gamma L)^2 \frac{\sinh^2\left[\sqrt{(\Gamma L)^2 - (\Delta k L/2)^2}\right]}{(\Gamma L)^2 - (\Delta k L/2)^2}, \tag{2.55}$$

where the gain coefficient is given by

$$\Gamma^2 = \frac{8\pi^2 d_{eff}^2}{\varepsilon_0 c n_p n_s n_i \lambda_s \lambda_i} I_p(0). \tag{2.56}$$

As perfect phase matching is not required, the signal and idler bandwidths are often large and their exact values depend on the gain and on how fast Δk increases with a frequency shift from the phase-matched point where $\Delta k = 0$. Δk can be approximated with a Taylor series in $\Delta\omega$,

$$\Delta k \simeq \left(\frac{1}{v_{gs}} - \frac{1}{v_{gi}}\right)\Delta\omega + \tfrac{1}{2}(\beta_{2s} + \beta_{2i})(\Delta\omega)^2, \tag{2.57}$$

where $v_{gj} = (\partial\omega/\partial k)_j$ and $\beta_{2j} = (\partial^2 k/\partial^2\omega)_j$. The first-order term in $\Delta\omega$ is sufficient as long as the group velocities are different, $v_{gs} \neq v_{gi}$. The equality,

$v_{gs} = v_{gi}$, occurs *e.g.* at degeneracy for a type-0 interaction, as the parametric waves then are identical, and the second-order term must be taken into account. For large gains, $\Gamma L \gg 1$, the FWHM bandwidth of the parametric waves, for a monochromatic pump, is for $v_{gs} \neq v_{gi}$

$$\Delta\nu \simeq \frac{2(\ln 2)^{\frac{1}{2}}}{\pi} \left(\frac{\Gamma}{L}\right)^{\frac{1}{2}} \left|\frac{v_{gs}v_{gi}}{v_{gs} - v_{gi}}\right|, \tag{2.58}$$

and for $v_{gs} = v_{gi}$

$$\Delta\nu \simeq \frac{2(\ln 2)^{\frac{1}{4}}}{\pi} \left(\frac{\Gamma}{L}\right)^{\frac{1}{4}} \left|\frac{1}{\beta_{2s} + \beta_{2i}}\right|^{\frac{1}{2}}. \tag{2.59}$$

The gain bandwidth is very broad at the degeneracy point, especially if that occurs at the wavelength where $\beta_{2s} = \beta_{2i} = 0$. In that case, third-order terms in $\Delta\omega$ need to be taken into account in Eq. (2.57). In order to reduce the bandwidth of the parametric waves and to increase the efficiency of the interaction, the nonlinear medium can be placed inside a cavity where at least one of the parametric waves is resonant. This forms an *optical parametric oscillator* (OPO), which can be used to convert a laser beam at the pump frequency to beams of lower frequencies. The first OPO was demonstrated in $LiNbO_3$ in 1965 [12] and was based on birefringent phase matching. 30 years later, the first quasi-phase-matched OPO was realised in periodically-poled $LiNbO_3$ with a period of $\Lambda = 15.5$ μm [42]. A simple design of a *singly-resonant* OPO is shown in Fig. 2.6(a). Only one of the parametric waves, in this case the signal, is resonant in the cavity, which provides feedback to the resonant wave. The cavity mirrors have high reflectivity for the signal, but low the idler, which does not resonate in the cavity. If the idler also were to resonate, the OPO would be *doubly resonant*. Tuning of the device can be achieved by adjusting the phase-matching or oscillation conditions. The phase matching can be changed by rotating the crystal, by changing the crystal temperature, by tuning the pump, by changing the QPM grating if QPM is employed, or by a combination of all of the above. The oscillation conditions can be changed by rotating the cavity for the resonant wave and make the interaction noncollinear. In a singly-resonant OPO, the oscillation threshold is reached when the gain equals the round-trip loss for the resonant wave, which for low internal losses is approximately given by

$$\Gamma_{th} L \simeq 1 - R_s, \tag{2.60}$$

where R_s is the intensity reflectivity at the signal frequency [12].

The OPO studied in this thesis is of a different kind. It is a *mirrorless* optical parametric oscillator (MOPO), which was proposed in 1966 [15], but has not been extensively studied experimentally until the first demonstration in 2007 [16] and in the continuing work in paper IV, paper V and paper VI. The MOPO is based on a different physical mechanism compared to conventional OPOs, such as the one in Fig. 2.6(a). For the MOPO, no resonant cavity is needed to provide feedback to the parametric waves. Instead, the parametric waves in a MOPO propagate in

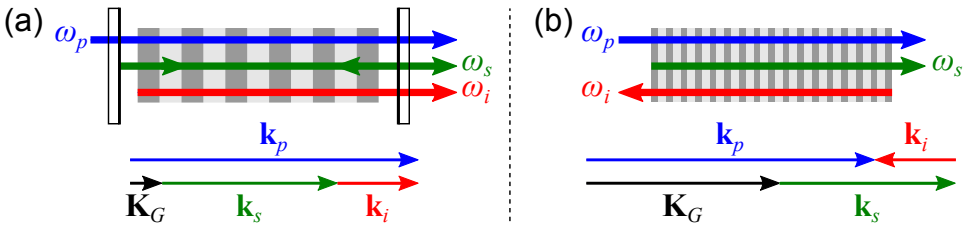

Fig. 2.6: (a) A conventional signal-resonant OPO, based on signal feedback from the cavity mirrors, generating signal and idler waves in the forward direction. (b) A mirrorless OPO based on distributed feedback between the counterpropagating parametric waves.

opposite directions and automatically establish a distributed-feedback mechanism when the crystal is pumped above threshold, which provides the necessary feedback for the oscillation. The MOPO concept is schematically illustrated in Fig. 2.6(b) and its special characteristics are further described in Chapter 5.

Large grating vectors are needed in order to quasi-phase-match counterpropagating interactions. An example of the grating vectors required for the four possible QPM configurations for collinear parametric down-conversion is illustrated in Fig. 2.7. The periods in KTP for interactions with $\lambda_p = 861.7$ nm, $\lambda_s = 1217.9$ nm and $\lambda_i = 2945.7$ nm are $\Lambda \simeq 805$ nm for a counterpropagating idler, $\Lambda \simeq 330$ nm for a counterpropagating signal, $\Lambda \simeq 236$ nm for counterpropagating signal and idler, compared to $\Lambda \simeq 30.27$ μm for a co-propagating interaction. The submicrometre periodicities are not easy to fabricate, but the fabrication techniques are under constant development, as is discussed in paper III and in Chapter 4.

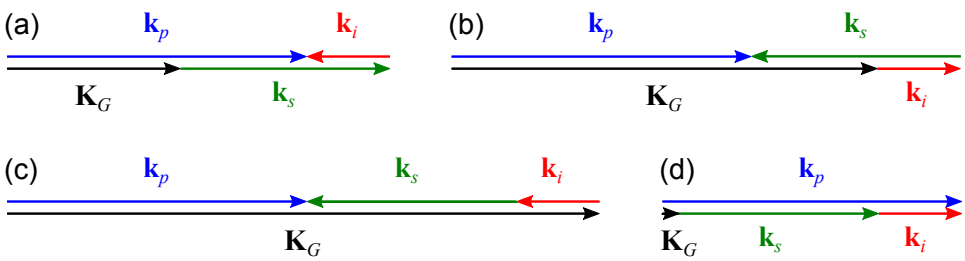

Fig. 2.7: The four collinear configurations to down-convert pump into signal and idler through QPM. (a) counterpropagating idler, $\Lambda \simeq 805$ nm, (b) counterpropagating signal, $\Lambda \simeq 330$ nm, (b) counterpropagating signal and idler, $\Lambda \simeq 236$ nm, (d) co-propagating configuration, $\Lambda \simeq 30.27$ μm. The vectors are approximately drawn to scale for $\lambda_p = 861.7$ nm, $\lambda_s = 1217.9$ nm and $\lambda_i = 2945.7$ nm in KTP, except in (d) where the length of $\mathbf{K}_G$ is significantly shorter than the arrow head.

2.6 Third-order nonlinear interactions

Unlike second-order nonlinear interactions, third-order nonlinear interactions take place in any material, centrosymmetric or not. The interactions describe the energy exchange between up to four distinct frequencies and is therefore referred to as *four-wave mixing*. Like for the second-order case, a degeneracy factor, $D^{(3)}$, can be introduced to simplify the expression for the nonlinear polarisation as a result of the intrinsic permutation symmetry:

$$P_j^{(3)}(\omega_\alpha) = \tfrac{1}{4}\varepsilon_0 D^{(3)} \sum_{\beta\gamma\delta} \sum_{klm} \chi^{(3)}_{jklm}(-\omega_\alpha;\omega_\beta,\omega_\gamma,\omega_\delta) E_k(\omega_\beta) E_l(\omega_\gamma) E_m(\omega_\delta), \quad (2.61)$$

where the value of $D^{(3)}$ depends on how many of the factors $E_k(\omega_\beta)$, $E_l(\omega_\gamma)$ and $E_m(\omega_\delta)$ that are taken from the same beam and have the same frequency. If this is the case for all three fields, then $D^{(3)} = 1$. $D^{(3)} = 3$ if that applies to two fields and $D^{(3)} = 6$ if all fields are distinct. Again, positive and negative frequencies are counted as distinct. The third-order polarisation induced by an electric field containing the positive frequencies ω_1, ω_2 and ω_3, together with their negative counterparts, contain the frequencies ω_α of the form

$$\omega_\alpha = \sigma_\beta\omega_\beta + \sigma_\gamma\omega_\gamma + \sigma_\delta\omega_\delta, \quad (2.62)$$

where $\sigma_\beta, \sigma_\gamma, \sigma_\delta \in \{-1, 1\}$ and $\omega_\beta, \omega_\gamma, \omega_\delta \in \{\omega_1, \omega_2\, \omega_3\}$. At moderate intensities, third-order interactions are generally much weaker than second-order ones. Therefore, second-order interactions are more common for efficient frequency conversions, making third-harmonic generation more efficient by two sequential $\chi^{(2)}$ processes than by one $\chi^{(3)}$ process. However, third-order effects may be large in optical fibres due to the long interaction lengths [43].

Nonlinear index of refraction

The main interest of four-wave mixing for this work is the case of *degenerate four-wave mixing* where an intense laser beam due to a $\chi^{(3)}$ nonlinearity modifies the refractive index that the beam itself experiences in the medium, which is referred to as *self-action*. A change in the refractive index that is proportional to the intensity of the optical beam, $\Delta n = n_2 I$, is often referred to as the *optical Kerr effect* and such a nonlinearity is called a Kerr nonlinearity. The coefficient n_2, which has the units of inverse intensity, is referred to as the nonlinear index of refraction.

If a beam contains the positive frequency ω and is linearly polarised along a principal axis, here taken as the x axis, the third-order polarisation along the same axis is

$$P_x^{(3)}(\omega) = \tfrac{3}{4}\varepsilon_0 \chi^{(3)}_{xxxx}(-\omega;\omega,-\omega,\omega) E_x(\omega) E_x(-\omega) E_x(\omega). \quad (2.63)$$

It should be stressed that this interaction is automatically phase matched, as all interacting fields have the same polarisation direction and the frequencies are in

pairs of $\pm\omega$. The total polarisation at the frequency ω that is generated from linear and third-order effects is then

$$P_x(\omega) = \varepsilon_0 \left[\chi^{(1)}_{xx} + \tfrac{3}{4}\chi^{(3)}_{xxxx}|E_x(\omega)|^2\right] E_x(\omega) \equiv \varepsilon_0 \chi^{(1)}_{xx,eff}(I) E_x(\omega). \tag{2.64}$$

The frequency arguments have been dropped as only one frequency is involved and an intensity-dependent effective $\chi^{(1)}_{xx}$ has been introduced, which in terms of intensity is

$$\chi^{(1)}_{xx,eff}(I) = \chi^{(1)}_{xx} + \frac{3I}{2\varepsilon_0 c n_0}\chi^{(3)}_{xxxx}, \tag{2.65}$$

where n_0 denotes the linear refractive index. The real part of the intensity-dependent susceptibility leads to an intensity-dependent index of refraction,

$$n(I) = \sqrt{1 + \mathrm{Re}[\,\chi^{(1)}_{xx,eff}(I)\,]} \simeq n_0 + \frac{3\mathrm{Re}[\,\chi^{(3)}_{xxxx}\,]}{4\varepsilon_0 c n_0^2} I, \tag{2.66}$$

which defines the nonlinear index of refraction as

$$n_2 = \frac{3\mathrm{Re}[\,\chi^{(3)}_{xxxx}\,]}{4\varepsilon_0 c n_0^2}. \tag{2.67}$$

The Taylor expansion of the square root in Eq. (2.66) is valid when the intensity-dependent part $n_2 I$ is small compared to the linear refractive index, $n_2 I \ll n_0$. It is shown in Chapter 3 that this is the case even for highly nonlinear materials and intensities of several tens of GW/cm^2. Similar to the introduction of n_2, nonlinear absorption can be included by assuming that the absorption coefficient has an intensity dependence,

$$\alpha(I) = \alpha + \beta I. \tag{2.68}$$

The part of the absorption coefficient that is proportional to the intensity is related to *two-photon absorption* (TPA), which occurs when the energy of two photons in the beam exceeds the energy of a transition between energy states in the medium. The TPA coefficient, β, is related to the imaginary part of $\chi^{(3)}_{xxxx}$,

$$\beta = \frac{3\omega\mathrm{Im}[\,\chi^{(3)}_{xxxx}\,]}{2\varepsilon_0 n_0^2 c^2}. \tag{2.69}$$

Measurement techniques for n_2 and β are explained in Chapter 3.

Effects of a nonlinear index of refraction

A nonlinear index of refraction affects optical beams both in the time-frequency domain and in the spatial domain due to nonlinear phase shifts. The nonlinear phase shift after propagation through a medium of length L is

$$\phi_{NL} = \frac{2\pi\Delta n(I)}{\lambda} L, \tag{2.70}$$

which gives rise to a frequency shift of

$$\delta\omega = \frac{\partial\phi_{NL}}{\partial t} = \frac{2\pi}{\lambda}\frac{\partial[\Delta n(I)]}{\partial t}L. \tag{2.71}$$

A frequency shift hence only occurs when there is a temporal change in the intensity-dependent refractive index, for which it is necessary that the beam is pulsed. In a Kerr medium, $\Delta n(I) = n_2 I$, a pulsed beam experiences a phase shift proportional to $\partial I/\partial t$, which leads to a modification of the phase modulation in the beam and thereby also of the spectral content in the pulse. This is known as *self-phase modulation* (SPM) [44], which can be used to broaden [45, 46] or to narrow [47] pulses in the frequency domain. Balancing of the effect of SPM with dispersion leads to the generation of temporal solitons [48]. An intensity-dependent refractive index can also be used for all-optical switching [49] and signal processing [50].

A similar effect also occurs in the spatial domain. As the intensity of a focused beam has a transverse dependence, the amount of nonlinear phase acquired in the medium varies transversely across the beam. This leads to a changed curvature of the wavefronts, as wavefronts are surfaces of constant phase, which leads to nonlinear lensing and possibly *self-trapping* [51] or *self-focusing* [52] of the light. The nonlinear lensing properties, which *e.g.* can be used for the generation of spatial solitons [53] or modelocking of lasers by *Kerr-lens modelocking* (KLM) [13], are further discussed in Chapter 3.

Chapter 3

Characterisation of the Kerr nonlinearity

The main aim of laser-material engineering is to tailor the magnitude and the spectrum of relevant absorption and emission cross sections. In many cases, this also results in a collateral modification of the nonlinear response. This chapter is devoted to the investigation of variations in the Kerr nonlinearity in novel polystructural (monoclinic and tetragonal) laser hosts derived from the same double-tungstate family of crystals. This family of crystals is characterised by large spectroscopic cross sections and is very suitable for spectral engineering. It is shown in paper I and paper II that the variation of the Kerr nonlinearity in different chemical compositions of these crystals can be rather large. The findings are important for the field of ultrashort-pulse oscillators and amplifiers, where these materials are increasingly used.

3.1 $MT(XO_4)_2$ laser crystals

Double-tungstate and double-molybdate crystals with the chemical composition $MT(XO_4)_2$ (in short, MTX) are common host materials for optically-active ions, such as Yb^{3+}, Nd^{3+}, Er^{3+}, Tm^{3+} and Ho^{3+}. In the formula, M is a monovalent alkali cation, T is a trivalent cation and X denotes W or Mo for double tungstates and double molybdates, respectively. The compositions studied in this thesis involve laser-ion doped and undoped crystals with M = Na or K; T = Y, La, Gd, Lu, Yb or Bi.

Crystal structures

Depending on the growth conditions, the MTX compounds crystallise in different crystallographic structures. Many of the NaTX compounds melt congruently and can be grown by the Czochralski (Cz) method. In fact, this applies to all NaTX

compounds treated here, with the exception of NaLuW and samples with high doping concentrations. These can instead be grown by the top-seeded solution-growth slow-cooling (TSSG-SC) method from a high-temperature solution in $Na_2W_2O_7$ or Na_2WO_4 [54]. The NaTX compounds crystallise in *disordered* tetragonal structures [55, 56], meaning that the Na and T ions are randomly distributed on the same lattice sites [55, 57]. The crystals are optically uniaxial, with the optical axis coinciding with the crystallographic **c** axis. Light with ordinary and extraordinary polarisation, *i.e.* $\mathbf{H}||\mathbf{c}$ and $\mathbf{E}||\mathbf{c}$, are referred to as σ-polarised and π-polarised, respectively. The lattice constants are $a = b \simeq 5.20$ Å and $c \simeq 11.27$ Å for NaYW [58], with similar values for the other NaTX compounds.

As opposed to the sodium compounds that crystallise in disordered tetragonal forms, potassium compounds of the form KTW crystallise in monoclinic structures when grown by the TSSG-SC method from a solution in $K_2W_2O_7$ [59]. The monoclinic crystal structure gives rise to large anisotropies in the linear-dielectric, mechanical and thermal properties, which are described for KLuW in [60]. Monoclinic crystals are biaxial and the principal dielectric axis corresponding to the smallest refractive index, N_p, coincides for KTW compounds with the crystallographic **b** axis. KYW has the lattice constants $a \simeq 10.64$ Å, $b \simeq 10.35$ Å and $c \simeq 7.54$ Å, where the angle between the **a** and **c** axes is $\beta \simeq 130.5°$. The principal axis corresponding to the largest refractive index, N_g, is rotated an angle $\kappa \simeq 18.5°$ from the **c** axis and makes an angle $\beta + \kappa$ with the **a** axis. For KYW, the lattice constants and the angles are taken from [61] and the values for the other KTW compounds are similar. The relations between the crystallographic and the dielectric axes for the tetragonal and monoclinic crystals are illustrated in Fig. 3.1.

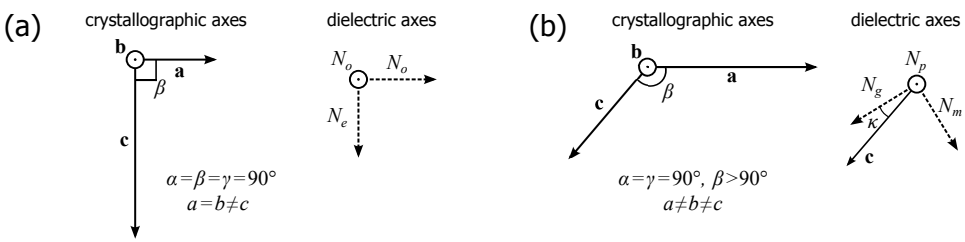

Fig. 3.1: (a) The optical axis, N_e, is parallel to the **c** axis in the uniaxial tetragonal structure. (b) N_g is rotated an angle κ from the **c** axis and makes an angle $\beta + \kappa$ with the **a** axis in the monoclinic structure. The crystallographic vectors in (a) and (b) are approximately drawn to scale for NaYW and KYW, respectively.

Optical properties

The linear refractive index of the MTX compounds is around 2. Fig. 3.2 shows the dispersion in NaYW [62] and KLuW [60] for wavelengths up to 1100 nm.

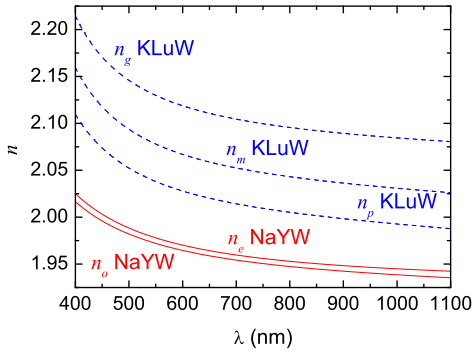

Fig. 3.2: The three principal indices in KLuW [60] and two in NaYW [62] as function of the wavelength.

In the NaTX compounds doped with active ions, the random distribution of the Na and T ions cause the crystal potential around the dopants to vary in the same random manner. This gives rise to a substantial inhomogeneous broadening of the spectral lines [55], which can be used to achieve an increased tunability or for the generation of ultrashort pulses [62]. However, as the spectral lines broaden, there is a proportional decrease in the peak of the emission and absorption cross sections [55, 56]. The emission and absorption cross sections in disordered Yb:NaYW are for the σ and π polarisations illustrated in Fig. 3.3 [62].

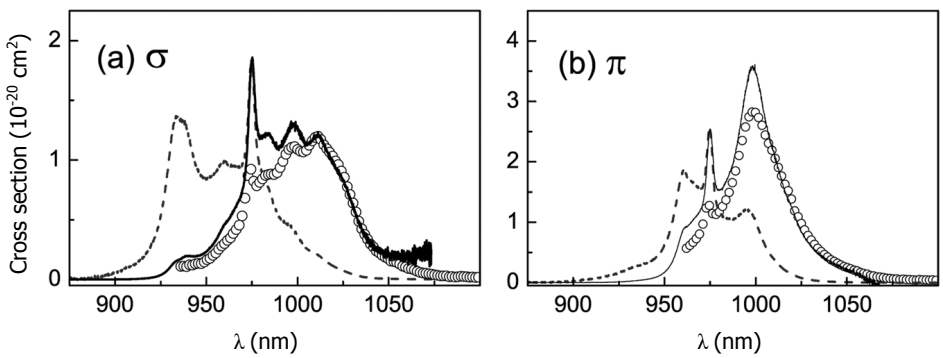

Fig. 3.3: Absorption (dashed line) cross section and the calculated (solid line) and directly-measured (circles) emission cross section in disordered Yb:NaYW [62].

In Yb:NaYW, the broad cross sections allow for broad laser tunability or the generation of pulses down to 53 fs by using a semiconductor saturable-absorber mirror (SESAM) for passive modelocking of the laser [62]. An example of the broad tunability and the ultrashort-pulse generation is shown in Fig. 3.4 .

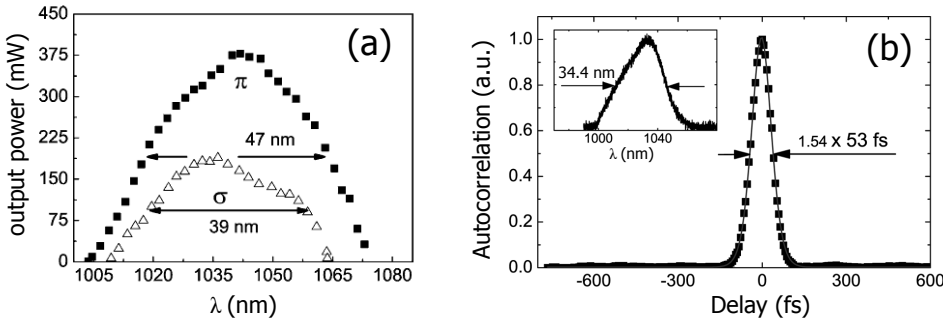

Fig. 3.4: (a) The wide tunability of continuous-wave lasing in disordered Yb:NaYW [62]. (b) Modelocked operation in disordered Yb:NaYW with pulse lengths of 53 fs [62].

Another way to passively modelock lasers is to use the nonlinear properties of the laser crystal itself. With a correct cavity design, the nonlinear focusing properties of the laser medium provide the saturable loss that favours a pulsed operation. This is referred to as *Kerr-lens modelocking* (KLM) and was first demonstrated in Ti:sapphire oscillators [13]. It has also been been demonstrated in monoclinic Yb:KYW with pulses down to 71 fs [63]. The monoclinic double tungstates have higher peak cross sections than the disordered tetragonal ones, as can be seen by comparing the cross sections for Yb:KYW [64] in Fig. 3.5 with the ones for Yb:NaYW in Fig. 3.3.

Due to the unsurpassed gain bandwidth in Ti:sapphire, the shortest laser pulses are generated from Ti:sapphire oscillators. Ti:sapphire lasers, however, suffer from some major drawbacks that can be overcome in Yb lasers. Ti:sapphire needs green light for pumping, which nowadays is provided by a frequency-doubled solid-state laser. Yb lasers, on the other hand, can be directly diode pumped and can be made very efficient due to the close frequency distance between the absorption (∼975 nm) and the emission wavelengths (∼1020 nm - 1070 nm).

For further development of KLM lasers with MTX crystals, the nonlinear properties of the crystals need to be known in order to properly design the laser cavities. n_2 for the disordered tetragonal crystals had not been characterised at all before the work in paper I. There was also some uncertainty regarding the anisotropy of n_2 along the different principal dielectric axes in the monoclinic compounds. The two very different values of $n_2 \simeq 8.7 \cdot 10^{-16}$ cm^2/GW for Yb:KYW [65] and $n_2 \simeq 21 \cdot 10^{-16}$ cm^2/GW for KYW [66] had previously been reported, where the first value was measured with $\mathbf{E}||\mathbf{a}$, *i.e.* not parallel to a principal axis, and the sec-

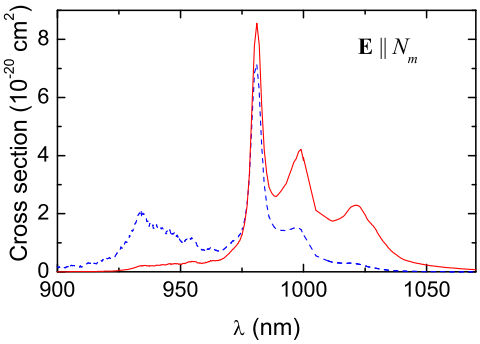

Fig. 3.5: Absorption (dashed line) and emission (solid line) cross section in monoclinic Yb:KYW for the electric field polarised along N_m [64].

ond value was measured with both $\mathbf{E}||N_m$ and $\mathbf{E}||N_p$, with no significant difference in n_2 between the two polarisations. This is in contrast to the values measured for Yb:KGdW [67], which show an anisotropy between the $\mathbf{E}||N_m$ and $\mathbf{E}||N_p$ cases. The uncertainties in the anisotropy measurements and the measurement of the new compound KLuW motivated for the measurements of n_2 with the light polarised along N_m and N_p in paper II.

3.2 The z-scan technique

The z-scan technique is a simple experimental method for the characterisation of a material's intensity-dependent refractive index and absorption coefficient by the use of a single focused beam [68]. The principle of the method is to scan the sample through the focus of the beam, while measuring the power transmitted through an aperture in the far field. Since the intensity distribution of the beam has a transverse dependence, the nonlinear phase acquired after passing through a sample with a nonlinear index of refraction varies across the beam. The sample then acts as a nonlinear lens, whose focusing properties alter the curvature of the wavefront that leaves the sample. This change in wavefront curvature modifies the beam-intensity pattern in the far field. Depending on the aperture geometry, this effect may modulate the power transmitted through the aperture, which is recorded throughout the scan as a function of the sample position relative to the focus and provides information about the nonlinear absorption or the nonlinear refractive index.

The nonlinear absorption can first be deduced by scanning the sample with the aperture fully open, so that all the light that is transmitted through the sample is collected. Any reduction in the measured power is then, apart from Fresnel reflections, due to nonlinear absorption. Once the nonlinear absorption is known,

another scan with the aperture partially closed gives information about the nonlinear index of refraction. A schematic sketch of the setup and a typical shape of the aperture transmittance for different sample positions are shown in Fig. 3.6.

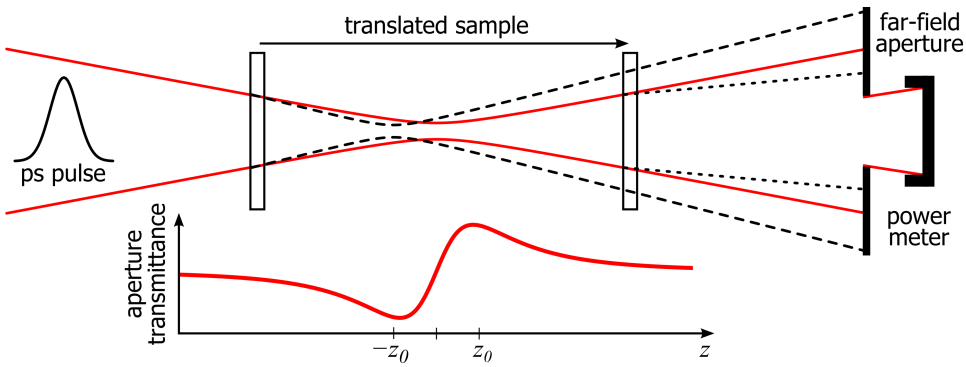

Fig. 3.6: The $z-$scan principle is that the power transmitted through the aperture in the far field changes as the sample is scanned through the beam. The nonlinear refractive index and absorption coefficient can be deduced by varying the aperture geometry.

Far away from the focus, the intensity is relatively low and the nonlinear lensing is therefore weak, causing the intensity to approach the value where the sample is not in the beam. If no nonlinear absorption occurs, the same intensity is also obtained when the sample is in the focus, since the sample then acts as a field lens and does not affect the far-field intensity distribution. Within a few Rayleigh lengths from the focus, the effect of the lensing is strongest and the intensity transmitted through the far-field aperture is modulated. Normally a scan of at least 8 Rayleigh lengths on each side of the focus is needed in order for the aperture transmittance to stabilise at a constant value. In theory, the sample thickness, L, has to be much smaller than the Rayleigh length of the beam, $L \ll z_0$, in order to simplify the mathematical evaluation of the nonlinear refractive index. It has however been experimentally verified that the same results are obtained as long as $L < z_0$ [68]. This greatly simplifies the experimental setup, as a smaller scanning range can be used. With a sample thickness of about 1 mm, the Rayleigh range can be 2.5 mm, meaning that a total scanning range of 40 mm is adequate, which is within the range of most motorised translation stages. To strictly fulfill that $L \ll z_0$, the scanning range would need to be increased by a factor of about 10 and scanning ranges around 400 mm are rather inconvenient.

$L \ll z_0$ could also be fulfilled by instead reducing the sample thickness, which however leads to other problems. The peak intensity needed for a certain modulation in the aperture transmittance is inversely proportional to the sample length, meaning that a thinner sample may have to operate close to, or even beyond, the damage threshold in order to show sufficient nonlinear lensing for the modulation

to be measurable. From a damage point of view, it is also more suitable to use pulse lengths of a few picoseconds compared to pulse lengths of tens of picoseconds. The nonlinear lensing in a given sample is in theory determined by the peak intensity of the pulse, meaning that a shorter pulse with lower energy can give rise to the same lensing as a longer pulse. The damage probability increases with both the peak intensity and the pulse duration [69], so the use of a shorter pulse is motivated.

z-scan theory

This subsection is based on the z-scan theory described in [68]. The refractive index is assumed to be of the form

$$n(I) = n_0 + \Delta n(I) \simeq n_0 + n_2 I, \tag{3.1}$$

where n_0 is the linear part and $\Delta n(I)$ is the intensity-dependent nonlinear part. If the nonlinear part is caused by a Kerr nonlinearity, *i.e.* by degenerate four-wave mixing in the material, the index change is proportional to the intensity, $\Delta n(I) = n_2 I$. The corresponding intensity-dependent absorption, $\alpha(I)$, consists of a linear part and a coefficient β related to the two-photon absorption,

$$\alpha(I) = \alpha + \beta I. \tag{3.2}$$

The beam that is used for the z-scan has a Gaussian spatial amplitude distribution,

$$A(\rho, z, t) = A_0(t)\frac{w_0}{w(z)} \exp\left[-\frac{\rho^2}{w^2(z)} + i\frac{k\rho^2}{2R(z)} + i\zeta(z)\right], \tag{3.3}$$

where $w^2(z) = w_0^2[1 + (z/z_0)^2]$ and $R(z) = z + z_0^2/z$ define the $1/e^2$ intensity radius and wavefront radius of curvature, respectively. The Gouy phase, $\zeta(z)$, has no ρ dependence and does not contribute to any change in the radial distribution. $A_0(t)$ denotes the temporal shape of the pulse, which typically is a linearly-chirped Gaussian, $A_0(t) = A_0 \exp\left[-2\ln 2(t/\Delta t)^2 + ibt^2\right]$ close to the transform limit. In the presence of an intensity-dependent refractive index, the beam acquires a nonlinear phase shift, $\Delta\phi(\rho, z, t)$, as it propagates through the sample, which modifies the wavefront curvature and the radial intensity distribution in the far field. For a Kerr nonlinearity, $\Delta\phi(\rho, z, t)$ is proportional to the beam intensity,

$$I(\rho, z, t) = \frac{I_0(t)}{1 + (z/z_0)^2} \exp\left[-\frac{2\rho^2}{w^2(z)}\right], \tag{3.4}$$

and can be written,

$$\Delta\phi(\rho, z, t) = \frac{\Delta\Phi_0(t)}{1 + (z/z_0)^2} \exp\left[-\frac{2\rho^2}{w^2(z)}\right], \tag{3.5}$$

where $\Delta\Phi_0(t)$ is the on-axis phase shift at the focus of the beam,

$$\Delta\Phi_0(t) = \frac{2\pi n_2 I_0(t) L_{eff}}{\lambda}. \tag{3.6}$$

L_{eff} is the effective length given by the physical length L and the linear absorption coefficient α as $L_{eff} = [1 - \exp(-\alpha L)]/\alpha \simeq L$ for $\alpha \simeq 0$. As a pulsed beam normally is used in order to reach the high peak powers that are needed in order to observe a nonlinear effect, the measurement contains a temporal average of the refractive-index change. For Gaussian pulses, the average index change is

$$\langle n_2 I_0(t) \rangle = n_2 I_0/\sqrt{2}, \tag{3.7}$$

where I_0 is the the on-axis peak intensity at the focus. Eq. (3.6) can then be rewritten in terms of the average phase shift at the focus,

$$\langle \Delta\Phi_0 \rangle = \frac{2\pi n_2 I_0 L_{eff}}{\sqrt{2}\lambda}. \tag{3.8}$$

At a distance $d \gg z_0$ from the focus, a circular aperture of radius ρ_a is centred on the optical axis. The power fraction of a Gaussian beam that passes through the aperture is $S = 1 - \exp(-2\rho_a^2/w_a^2)$, where w_a is the $1/e^2$ intensity radius at the aperture. However, the measured quantity after the aperture is absolute power rather than relative power, which is dependent on if absorption occurs in the sample. For now, it is assumed that no absorption occurs in the sample and the effects of absorption will be included later. Due to the fact that the beam experiences a ρ-dependent nonlinear phase shift in the sample, w_a will depend on the sample position, which explains why the transmitted intensity is modulated as the sample is scanned through the focus, as illustrated in Fig. 3.6. The effect is stronger when the aperture radius is small and $S \ll 1$. With a large aperture that collects most of the beam, $S \simeq 1$, the modulation is very low, as in principle all power is collected at all z positions. A sample with $n_2 > 0$, as the sample in Fig. 3.6, acts as a nonlinear positive lens, causing the beam to focus earlier when the sample is positioned at $z < 0$, resulting in a lower transmittance through the far-field aperture. When the sample instead is positioned at $z > 0$, the aperture transmittance increases as the sample still acts a a positive lens and decreases the angular spread of the beam. The opposite effect occurs for a sample with $n_2 < 0$. The distance between the positions where the maximum and minimum aperture transmittance occurs, called the *peak-to-valley* distance, is given by the Rayleigh length and is

$$\Delta z_{pv} \simeq 1.7 z_0. \tag{3.9}$$

The difference in aperture transmittance between the peak and the valley contains information about the nonlinear phase shift. A normalised transmittance, $T(z, \langle \Delta\Phi_0 \rangle)$, is defined as the power transmitted through the aperture when the sample is at position z divided by the transmitted power when the sample is far from the focus at $|z'| \gg z_0$. Within an uncertainty of ± 2 %, the peak-to-valley difference in normalised transmittance is proportional to $|\langle \Delta\Phi_0 \rangle|$,

$$\Delta T_{pv} \simeq 0.406(1 - S)^{\frac{1}{4}} |\langle \Delta\Phi_0 \rangle|, \tag{3.10}$$

for $|\langle\Delta\Phi_0\rangle| \leq \pi$. It is clear from Eq. (3.10) that the peak-to-valley transmittance difference is largest when the aperture is small, $S \simeq 0$, and vanishes when the aperture is fully open, $S = 1$. For small phase shifts, $|\langle\Delta\Phi_0\rangle| \ll 1$, the normalised transmittance can be written

$$T(z, \langle\Delta\Phi_0\rangle) \simeq 1 - \frac{4\langle\Delta\Phi_0\rangle x}{(x^2+9)(x^2+1)}, \tag{3.11}$$

where $x \equiv z/z_0$. This function is used to fit the experimentally-obtained values.

The theory above is based on the assumption that there is no absorption. Linear absorption results in a constant decrease in the transmitted intensity and can be avoided by measuring at wavelengths where the linear absorption is low, $\alpha \simeq 0$. However, two-photon absorption (TPA) occurs in many samples and that effect needs to be taken into account. As TPA is intensity dependent, the intensity through the aperture goes down as the sample approaches the focus. Fig. 3.7 shows z-scans of two samples with different amounts of TPA.

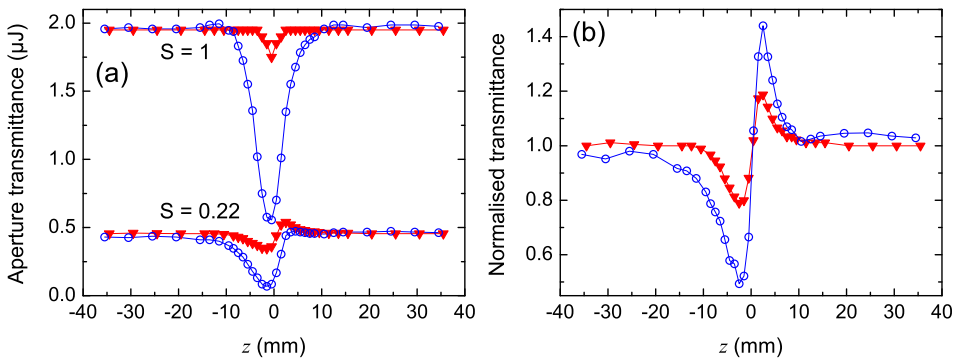

Fig. 3.7: (a) Measured transmittance through the aperture for π-polarised light in tetragonal Yb:NaGdW (triangles) with low TPA and NaBiW (circles) with high TPA. The graph shows z-scan traces with partially-closed aperture ($S = 0.22$) and fully-open aperture ($S = 1$). (b) Normalised scan based on the information in (a).

Fig. 3.7(a) shows z-scan traces with a fully-open aperture ($S = 1$) and with a partially-closed aperture ($S \simeq 0.22$). From the transmittance drop around $z = 0$ in the open-aperture scans, it can be deduced that TPA occurs in both Yb:NaGdW and NaBiW, but that the effect is much stronger in NaBiW. In order to compensate for the reduction in transmitted intensity due to TPA, the scan with partially-closed aperture is normalised by dividing the values by the open-aperture values at the corresponding z positions. The values are renormalised so that $T(z, \langle\Delta\Phi_0\rangle) \simeq 1$ for $|z| \gg z_0$, which yields the normalised trace in Fig. 3.7(b). The peak-to-valley transmittance difference, ΔT_{pv}, measured on a normalised curve, can be used to extract the nonlinear phase shift from Eq. (3.10). Using Eq. (3.8), the nonlinear

index of refraction is finally obtained as

$$n_2 \simeq \sqrt{2}\frac{\lambda}{2\pi}\frac{\langle\Delta\Phi_0\rangle}{I_0 L} \simeq \sqrt{2}\frac{\lambda}{2\pi}\frac{\Delta T_{pv}}{0.406(1-S)^{\frac{1}{4}} I_0 L}. \tag{3.12}$$

For Gaussian pulses, the TPA coefficient β can be calculated from the normalised trace with fully-open aperture by fitting the following equation to the experimental points:

$$T(z)|_{S=1} = \frac{1}{\sqrt{\pi} q_0(z)} \int_{-\infty}^{\infty} \ln\left[1 + q_0(z) e^{-\tau^2}\right] d\tau, \tag{3.13}$$

where τ is a dimensionless integration variable and $q_0(z) \equiv \beta I_0 L_{eff}/[1 + (z/z_0)^2]$.

3.3 Experimental z-scan setup

A linearly-polarised beam from a Ti:sapphire regenerative amplifier was used for the z-scans in paper I and paper II. The beam was pulsed with the repetition rate of 1 kHz, generating pulses of energies up to 1 mJ with pulse lengths between 2 ps and 4 ps. The pulse energy was reduced by using the 4 % relection from a glass surface and then controlled with a waveplate-polariser setup. As the Yb^{3+}-doped crystals are intended to lase between 1020 nm and 1070 nm, the wavelength for the z-scan was chosen to be relatively close to the lasing region, with the condition that the crystals did not exhibit linear absorption. For undoped and Yb^{3+}-doped samples, the wavelength of 820 nm was used in paper I and 819 nm in paper II. Two samples in paper I were doped with Nd^{3+} and Tm^{3+}, for which linear absorption was avoided by tuning the wavelength to 850 nm. The beam was focused to a $1/e^2$ intensity radius of 25 μm, resulting in a Rayleigh length of $z_0 = \pi w_0^2/\lambda \simeq 2.4$ mm, which is longer than the typical sample length of 1 mm. The far-field aperture was placed 0.6 m to 1 m away from the focus, *i.e.* at least $25z_0$.

The relative values of n_2 obtained in scans with the same experimental setup can be rather accurate, whereas the absolute values of n_2 depend on experimental uncertainties in the parameters in Eq. (3.12), with the largest uncertainty being in the peak intensity at the focus. Other sources of uncertainty is that the beam is not a perfect TEM_{00} beam, the pulses are not perfectly Gaussian and the aperture may not be properly centred on the optical axis. The setup can be evaluated by performing a z-scan with a well-characterised material, which in our case was a 1 mm-long reference sample of BK-7 glass. A scan of this sample yielded the value of $n_2 \simeq 4.5 \cdot 10^{-16}$ cm^2/W, which is in the range of the previously reported values between $3.45 \cdot 10^{-16}$ cm^2/W and $4.71 \cdot 10^{-16}$ cm^2/W [70–73] for BK-7. The absolute uncertainty in the values is estimated to be ± 20 %, which is comparable to that in other z-scan setups [67, 68, 74].

3.4 z-scan with tetragonal $NaT(XO_4)_2$ crystals

The nonlinear refractive index of disordered tetragonal NaTX crystals was measured in paper I, for both σ-polarised and π-polarised light. At the focus, the peak intensity was around 65 GW/cm^2 and the transmittance of the far-field aperture was set to $S \simeq 0.22$. The scanned crystals had a thickness in the range between 0.74 mm and 2.08 mm. Fig. 3.8 illustrates the normalised transmittance of four of the samples and the measured values of n_2 for all the seven samples are found in Table 3.1.

The first observation is that the nonlinear refractive index is positive for all the measured NaTX compounds. This is deduced by noting that the valley is located at $z < 0$ and the peak is located at $z > 0$, meaning that the nonlinear lensing is positive and thereby $n_2 > 0$. For the laser-ion doped crystals, the samples with large T^{3+} ionic radii, NaLaW and NaGdW, have the smallest values of n_2, around $16 \cdot 10^{-16}$ cm^2/W. The values for Yb:NaYW and NaLuW are around a factor of 2 larger. It is also observed that the strength of the Kerr nonlinearity in Yb:NaYX is not appreciably changed when W^{6+} is replaced with Mo^{6+}. The largest Kerr nonlinearity is found in NaBiW, where n_2 is around a factor of 2 larger than for Yb:NaYX. NaBiW also has a large nonlinear birefringence, $|n_{2\sigma} - n_{2\pi}|$, which for the other NaTX compounds is rather low.

TPA was observed in most crystals in Table 3.1. From Eq. (3.13), the TPA coefficient was estimated to be $\beta \simeq 0.4$ cm/GW in NaBiW, compared to $\beta \simeq 0.09$ cm/GW for Yb:NaGdW and $\beta \simeq 0.04$ cm/GW for NaLuW. The differences in TPA coefficients is related to the bandgaps, which for π-polarised light increases from 3.50 eV (355 nm) in NaBiW to 4.18 eV (297.2 nm) in NaGdW and 4.29 eV (289.3 nm) in NaLuW [75]. Compared to for the z-scan wavelength of 820 nm, the effect of TPA will be lower when lasing occurs, as the wavelengths then are around 1040 nm and the photon energies are lower.

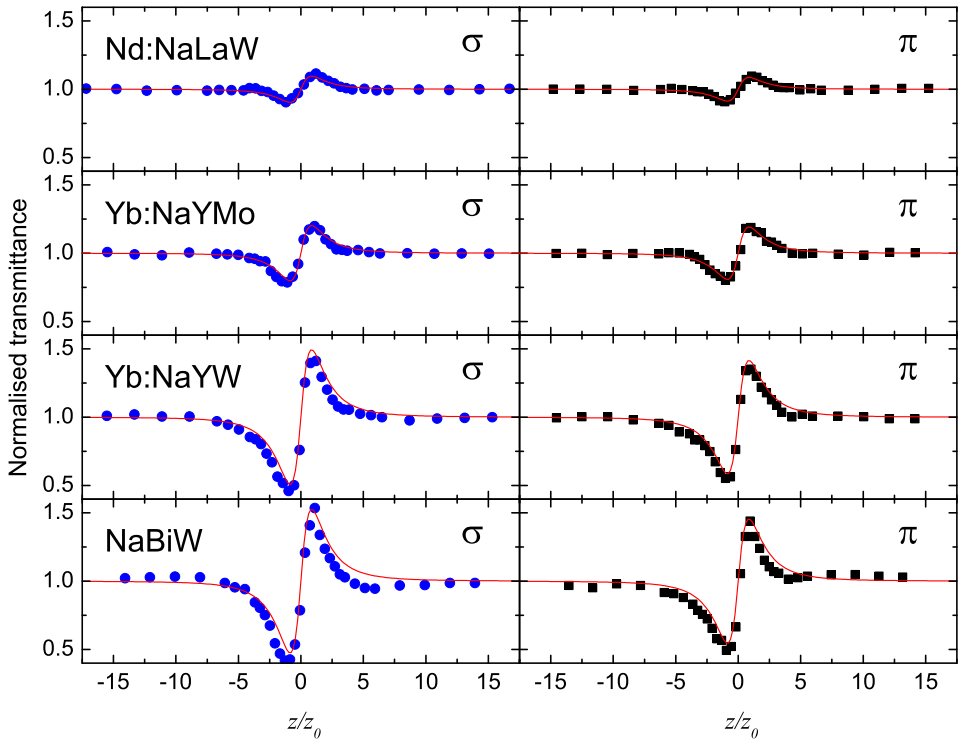

Fig. 3.8: z-scan measurements of four different doped and undoped disordered tetragonal $NaT(XO_4)_2$ crystals [paper I]. The sample thickness and the peak intensity used in each sample are slightly different, so the traces cannot be directly compared to evaluate the relative values of n_2.

Table 3.1: Nonlinear refractive index for disordered tetragonal $NaT(XO_4)_2$ crystals.

Crystal	Dopant	L (mm)	n_2^* (σ)	n_2^* (π)
NaLaW	Nd (10 at. %)	0.911	15^a	13^a
NaLaW	Tm (5 at. %)	0.745	16^a	16^a
NaGdW	Yb (5 at. %)	2.081	17^b	17^b
NaYW	Yb (10 at. %)	1.875	35^b	30^b
NaYMo	Yb (10 at. %)	0.848	34^b	33^b
NaLuW	-	0.995	23^b	28^b
NaBiW	-	1.160	68^b	58^b

* in units of 10^{-16} cm^2/W. $^a\lambda = 850$ nm. $^b\lambda = 820$ nm.

3.5 z-scan with monoclinic $KT(WO_4)_2$ crystals

The nonlinear refractive index of monoclinic KTW crystals was measured in paper II, for light polarised along N_p and N_m. At the focus, the peak intensity was around 50 GW/cm^2 and the transmittance of the far-field aperture was set to $S \simeq 0.18$. The crystal thickness was around 1.0 mm for all samples. Fig. 3.10 illustrates normalised transmittance of four of the samples and the measured values of n_2 for all the seven samples are found in Table 3.2, with values ranging between $15 \cdot 10^{-16}$ cm^2/W and $26 \cdot 10^{-16}$ cm^2/W.

Compared to the disordered tetragonal NaTX compounds, the monoclinic KTW compounds exhibit less two-photon absorption, with a maximum decrease in the intensity at the focus of 3 % for KLuW. The KTW crystals also have a larger anisotropy in n_2 along the principal axes, with a larger n_2 for $\mathbf{E}||N_m$ compared to $\mathbf{E}||N_p$. As $n_m > n_p$, it is to be expected from Miller's rule, the third-order generalisation of Eq. (2.32), that the nonlinear refractive indices also are related as $n_{2m} > n_{2p}$. This is beneficial, as the KTW compounds have larger absorption and emission cross sections when $\mathbf{E}||N_m$ and the higher nonlinear index can then be used for Kerr-lens modelocking. It is observed that n_{2m} increases in the order KLuW, KYbW, KYW, KGdW and it is illustrated in Fig. 3.9(a) that the increase has an almost linear dependence on the raduis of the T^{3+} ion. The nonlinear birefringence, $n_{2m} - n_{2p}$, also increases in this order and this effect is less pronounced when the crystals are doped with Yb^{3+}, as shown in Fig. 3.9(b).

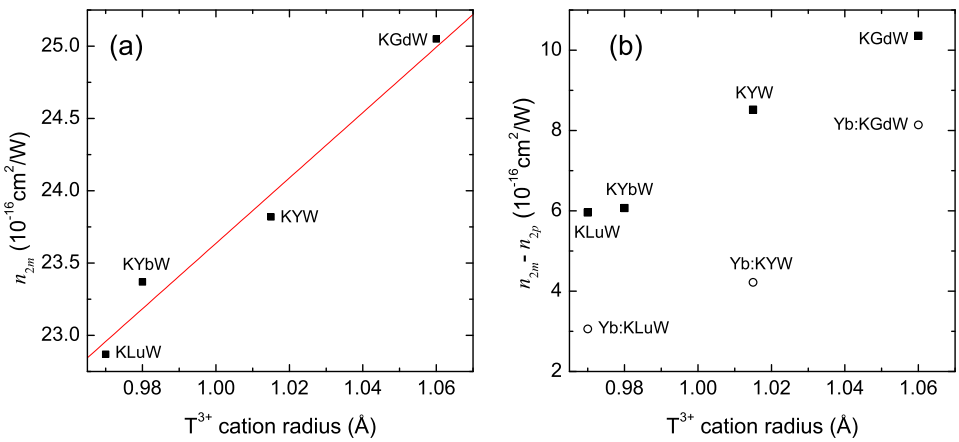

Fig. 3.9: (a) For $\mathbf{E}||N_m$, n_2 increases approximately linearly with the T^{3+} ionic radius [paper II]. (b) The nonlinear birefringence also increases with the T^{3+} ionic radius, but the effect is lower when the crystals are doped with Yb^{3+} [paper II].

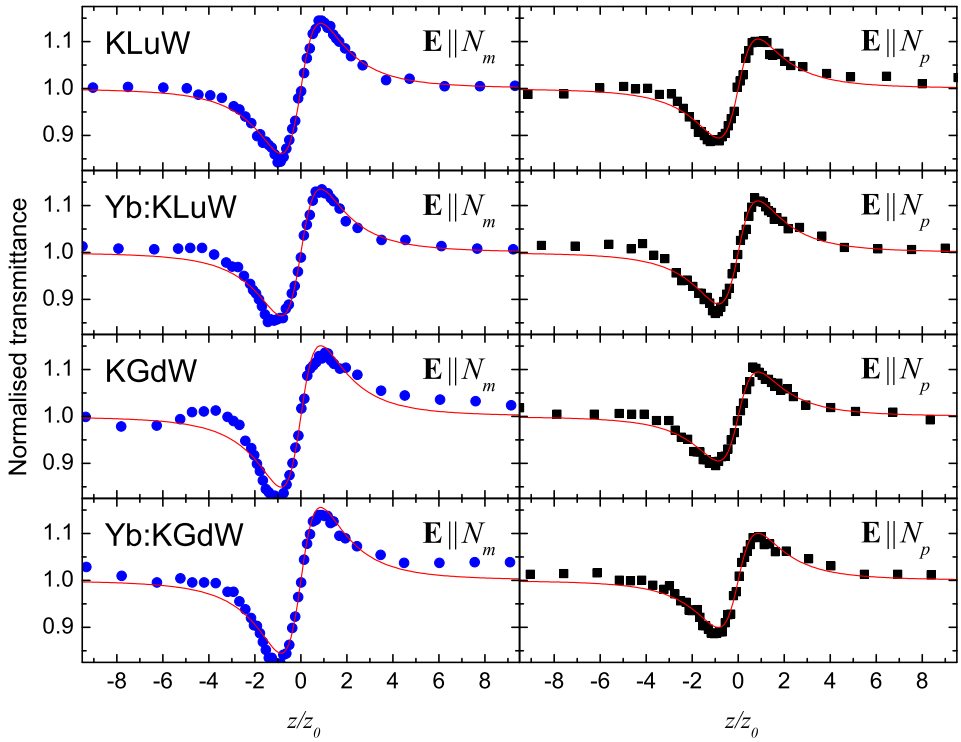

Fig. 3.10: z-scan measurements of four different doped and undoped monoclinic $KT(WO_4)_2$ crystals [paper II]. The sample thickness and the peak intensity used in each sample are similar, so the traces can be directly compared to evaluate the relative values of n_2.

Table 3.2: Nonlinear refractive index for monoclinic $KT(WO_4)_2$ crystals.

Crystal	Dopant	L (mm)	n_2^* ($\mathbf{E}\|\|N_m$)	n_2^* ($\mathbf{E}\|\|N_p$)
KLuW	-	1.034	23	17
KLuW	Yb (5 at. %)	1.032	22	19
KYbW	-	0.996	23	17
KYW	-	1.063	24	15
KYW	Yb (5 at. %)	1.026	19	15
KGdW	-	1.013	25	15
KGdW	Yb (5 at. %)	1.034	26	17

* in units of 10^{-16} cm^2/W. $\lambda = 819$ nm.

3.6 Conclusions

The nonlinear index of refraction of doped and undoped disordered-tetragonal and monoclinic $MT(XO_4)_2$ crystals were measured in paper I and paper II, with the measured values displayed in Table 3.1 and Table 3.2. The values range between $13 \cdot 10^{-16}$ cm^2/W and $68 \cdot 10^{-16}$ cm^2/W for the tetragonal crystals and $15 \cdot 10^{-16}$ cm^2/W and $26 \cdot 10^{-16}$ cm^2/W for the monoclinic samples. These Kerr coefficients are 5 to 22 times as large as that of sapphire, $n_2 \simeq 3.1 \cdot 10^{-16}$ cm^2/W [76], which means that the samples doped with active ions are good candidates for Kerr-lens modelocking of lasers.

The crystal with the highest Kerr nonlinearity is NaBiW. However, the attempts to Cz-grow NaBiW doped with adequate amounts of active Yb^{3+} or Tm^{3+} ions for lasing has so far been unsuccessful [77]. The increased amount of dopants leads to modification of the melting properties, which results in degradation of the optical quality of the crystals. Other growth procedures must therefore be developed for the fabrication of Yb:NaBiW crystals. The high Kerr nonlinearity of NaBiW could be related to the electronic structure of Bi^{3+}. Glasses doped with heavy ions, like Pb^{2+} and Bi^{3+}, also exhibit an increased Kerr nonlinearity, which has been attributed to the hyperpolarisability associated with the lone $6s^2$ electron pair of these ions [78].

It is also worth to comment on the magnitude of the change in the refractive index due to the Kerr nonlinearity in these crystals. By using σ-polarised light with an on-axis peak intensity of $I_0 \simeq 65$ GW/cm^2 in NaBiW, where $n_2 \simeq 68 \cdot 10^{-16}$ cm^2/W, the maximum value of the intensity-dependent part of the refractive index is $\Delta n = n_2 I_0 \simeq 4.4 \cdot 10^{-4}$ at the focus of the beam. This value should be compared to 2.170, which is the linear refractive index of σ-polarised light in NaBiW at a wavelength of 820 nm [77]. The relative change in the refractive index at this high intensity is hence only 0.02 % and the Taylor expansion in Eq. (2.66) is thereby valid. The other samples have lower Kerr nonlinearities and the relative changes in the refractive index are even lower, but are still enough for nonlinear lensing.

Chapter 4

Structure engineering of $KTiOPO_4$

$KTiOPO_4$ (KTP) is a ferroelectric crystal with a wide transparency range and a relatively high second-order nonlinearity, which is extensively used for nonlinear frequency conversions with either birefringent phase matching or quasi-phase matching. *Electric-field poling* turns a KTP crystal consisting of only one ferroelectric domain into a *periodically-poled* KTP (PPKTP) crystal with domains of alternating polarity with a fixed periodicity. The domain inversion also leads to a sign change of the second-order d_{jm} coefficients, which spectrally modifies the nonlinear response, and the PPKTP crystal can be used for quasi-phase-matched interactions. By proper design of the domain-inversion periodicity, any nonlinear interaction within the crystal's transparency range can be made efficient. This chapter gives an overview of the KTP properties and some of the findings in paper III, including the fabrication techniques for submicrometre PPKTP, which is a necessary component for the mirrorless optical parametric oscillator used in paper IV, paper V and paper VI.

4.1 Crystallographic properties of $KTiOPO_4$

The crystal structure of $KTiOPO_4$ is orthorhombic and belong to the noncentrosymmetric point group $mm2$ and the space group $Pna2_1$ [79]. The lattice constants are $a \simeq 12.81$ Å, $b \simeq 6.40$ Å and $c \simeq 10.62$ Å [80], where the two-fold symmetry axis is in the direction of the **c** axis and the two mirror planes are each perpendicular to the **a** or **b** axes. Each unit cell contains eight formula units of $KTiOPO_4$, which has a structure characterised by chains of TiO_6 octahedra that bind to each other directly and also via bridges of PO_4 tetrahedra. An illustration of the crystal structure is found in Fig. 4.1(a). The lengths of the Ti-O bonds alternate between between long and short, which gives rise to the ferroelectricity and a spontaneous electric polarisation, $\mathbf{P}_s$, along **c**. Regions of the same direction of $\mathbf{P}_s$ form *ferroelectric domains* in the crystal, where the polarity determines the signs of

the d_{jm} coefficients. The spontaneous polarisation can be inverted by applying an electric field with opposite polarity and a magnitude that is larger than the *coercive field*, E_c, which for KTP is around 2 kV/mm [33]. A three-dimensional network is formed by the TiO_6-PO_4 chains, in which channels are formed where the potassium ions are located at two nonequivalent lattice sites, K1 and K2. The potassium ions can move in these channels and the crystal therefore has a rather high ionic conductivity. Above the Curie temperature, 934 °C [80], $KTiOPO_4$ undergoes a phase transition and becomes paraelectric. The crystal structure is then centrosymmetric with the point group *mmm* and the space group *Pnan* [81]. The melting point is around 1150 °C [79].

As rubidium is located just below potassium in the periodic table, Rb^+ ions can substitute K^+ ions in the crystal structure. A low Rb^+ content, typically below 1 % of the K^+ ions, hardly affects the linear and nonlinear properties of KTP, but the larger ionic radius lowers the ionic conductivity by about two orders of magnitude [82]. The coercive field is 3.8 kV/mm, about twice as high as for undoped KTP.

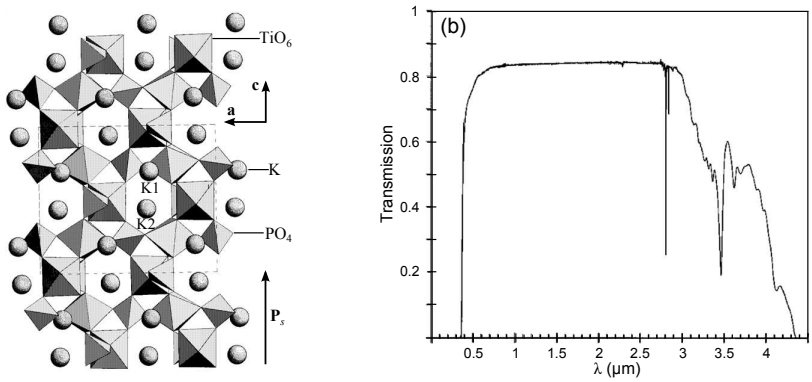

Fig. 4.1: (a) The crystal structure of $KTiOPO_4$ in the ferroelectric phase [81]. (b) The transmission through 10 mm $KTiOPO_4$ [83]. Fresnel reflections have reduced the transmission by approximately 9 % per surface.

4.2 Optical properties of $KTiOPO_4$

$KTiOPO_4$ has a wide transparency window between 365 nm and 4.3 μm [83]. In the infrared, there is a transmission dip around 2.8 μm due to OH groups trapped in the crystal during growth. The transparency is reduced for wavelengths longer than around 3 μm, as can be seen in the transmission graph in Fig. 4.1(b). The principal dielectric axes x, y and z are parallel to the crystallographic axes **a**, **b** and **c**, respectively. For nonlinear applications, z polarised waves are of a particular interest, since the largest d_{jm} coefficient, d_{33}, then is accessible. For this

polarisation, the refractive index, n_z, calculated from different Sellmeier expansions [84–86] is shown in Fig. 4.2(a), together with the group index in Fig. 4.2(b) and the group-velocity dispersion (GVD) coefficient $\beta_2 \equiv \partial^2 k/\partial\omega^2 = \lambda^3/(2\pi c^2)\partial^2 n/\partial\lambda^2$ in Fig. 4.2(c).

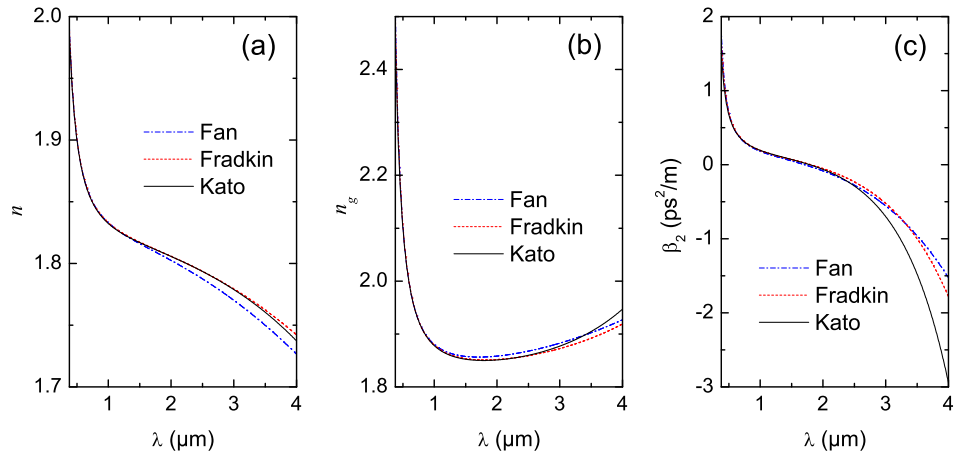

Fig. 4.2: (a) Index of refraction (b) group index and (c) GVD coefficient for z-polarised light in $KTiOPO_4$ as function of the vacuum wavelength, calculated with the Sellmeier expansions by Fan *et al.* [84], Fradkin *et al.* [85] and Kato *et al.* [86].

Unless otherwise stated, the Sellmeier expansion by Kato *et al.* [86] is used for the calculations of the refractive index in this thesis. n_z is then given by

$$n_z^2(\hat{\lambda}) = 4.59423 + \frac{0.06206}{\hat{\lambda}^2 - 0.04763} + \frac{110.80672}{\hat{\lambda}^2 - 86.12171}, \tag{4.1}$$

where $\hat{\lambda}$ is the vacuum wavelength in μm. This expression is valid at 20 °C and can be estimated at other temperatures with the temperature derivative,

$$\begin{aligned} \frac{\partial n_z}{\partial T} &= \left(\frac{9.221}{\hat{\lambda}^3} - \frac{29.220}{\hat{\lambda}^2} + \frac{36.677}{\hat{\lambda}} - 1.897\right)\cdot 10^{-6}/\mathrm{K}, \qquad 0.53 \le \hat{\lambda} \le 1.57 \\ \frac{\partial n_z}{\partial T} &= \left(\frac{-5.523}{\hat{\lambda}} + 33.920 - 17.101\hat{\lambda} + 3.424\hat{\lambda}^2\right)\cdot 10^{-6}/\mathrm{K}, \quad 1.32 \le \hat{\lambda} \le 3.53. \end{aligned} \tag{4.2}$$

A change in the crystal temperature also leads to thermal expansion, which due to the anisotropic crystal structure is larger in the x and y directions and has the expansion coefficients $\alpha_x \simeq 9.5\cdot 10^{-6}/\mathrm{K}$, $\alpha_y \simeq 9.2\cdot 10^{-6}/\mathrm{K}$ and $\alpha_z \simeq 0.3\cdot 10^{-6}/\mathrm{K}$ [87].

In contracted form, the second-order susceptibility tensor for orthorhombic $mm2$ crystals is

$$\begin{pmatrix} 0 & 0 & 0 & 0 & d_{15} & 0 \\ 0 & 0 & 0 & d_{24} & 0 & 0 \\ d_{31} & d_{32} & d_{33} & 0 & 0 & 0 \end{pmatrix}, \tag{4.3}$$

where $d_{31} = d_{15}$ and $d_{32} = d_{24}$ when Kleinman symmetry is valid. The second-order nonlinear coefficients of $KTiOPO_4$ have been experimentally measured for frequency-doubling of light at 1064 nm with the typical values $d_{15} \simeq 1.9$ pm/V, $d_{24} \simeq 3.6$ pm/V, $d_{31} \simeq 2.3$ pm/V, $d_{32} \simeq 4.0$ pm/V and $d_{33} \simeq 16.9$ pm/V [41]. Clearly, d_{33} is much larger than the other coefficients, but is in principle only accessible through quasi-phase-matched interactions.

Another important optical parameter is the damage threshold. It is hard to give an exact value for the damage threshold, as it depends on the pulse length and the wavelength, but it also varies from crystal to crystal. One value that has been reported is 15 GW/cm^2 for a pulse length of 1 ns at 1064 nm [84]. For shorter pulses, the damage threshold as a rule of thumb scales with the inverse square root of the pulse length. The large transparency range and the relatively high nonlinearity, together with a high damage threshold, makes KTP a good candidate for a material to use in OPOs.

4.3 Periodic poling of $KTiOPO_4$

In order to use KTP for quasi-phase-matched interactions, it is necessary to periodically invert the sign of the spontaneous polarisation. This can be done by periodic ion exchange [88], but is more often done by periodic poling, which first was demonstrated in 1997 [33]. The periodic poling is done by coating a surface of a crystal that consists of only a single ferroelectric domain with a metal-insulator periodic pattern. By applying a high electric field, the ferroelectric domains can then be inverted under the part of the crystal surface that has contact with the metal. Typical crystal dimensions are 10 mm × 5 mm × 1 mm in the **a**, **b** and **c** directions, respectively. A schematic sketch of the different steps from single-domain KTP to PPKTP is illustrated in Fig. 4.3.

An insulating photoresist layer with a thickness of a few micrometres is first spun onto the c^- face of the crystal and is heat treated at 110 °C for 90 s. A photolithographic mask with a periodic pattern of the desired period is placed on top of the photoresist, which is illuminated by UV light through the mask for a few milliseconds. For one-dimensional patterns, the mask is normally aligned with the crystal so that the periodicity is in the **a** direction. The reason for this is that the domain growth is much faster in the **b** direction [89, 90] compared to **a**, meaning that it is easier to pole dense grating along **a** than along **b**. The UV light breaks molecular bonds in the photoresist, which makes the exposed resist dissolve when the crystal is immersed into a developing solution. If this is done correctly, there is now a periodic pattern with air and photoresist on the c^- face. The air gaps

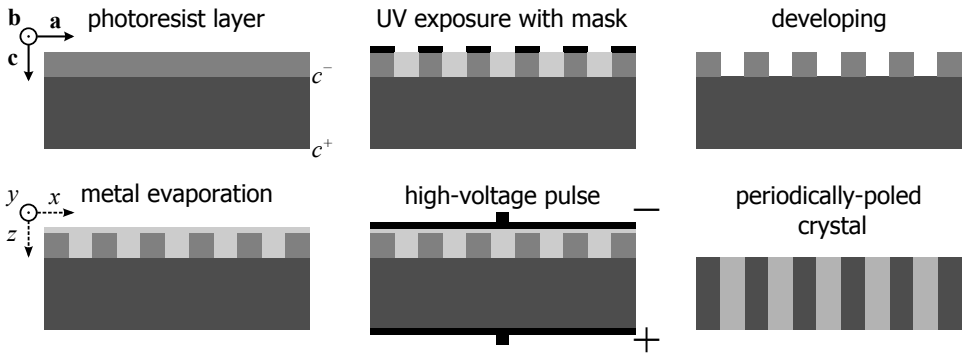

Fig. 4.3: An insulating photoresist layer is spun onto the c^- face of the crystal. A periodic pattern is written in the photoresist by UV exposure under a periodic mask. The photoresist is developed and aluminium is evaporated onto the pattern. The crystal is connected to a high-voltage supply and the ferroelectric domains are inverted where there is metal contact.

are then filled with aluminium, typically with a thickness around 100 nm, which is evaporated onto the c^- face in a vacuum chamber. The crystal is now ready to be poled and is connected to a high-voltage supply via liquid electrodes in the form of a solution of KCl. A voltage pulse that produces fields of the order of the coercive field with a duration of a few milliseconds is applied and the ferroelectric domains are periodically inverted where there is metal contact. The metal increases the domain nucleation rate [91] and increases the probability that the domains start growing on the c^- face and propagate through towards c^+.

The procedure described above and in Fig. 4.3 appears straight forward, but as every crystal sample is slightly different, particularly in terms of ionic conductivity, the process needs to be monitored so that one can adjust the voltage and the length of the electric pulses in order to reach the desired result. A too low voltage does not pole the sample and a too high voltage poles it even under the insulating photoresist. There are two main ways to monitor the poling process. One way is to monitor the polarisation rotation caused by the electro-optic effect as the poling voltage is applied across the crystal [92]. This is done by shining a HeNe laser through a polariser, then through the crystal and through a second polariser, which is rotated 90° with respect to the first one. With no voltage applied, there is no transmission of the HeNe beam through the second polariser. When the poling pulse is applied and if no poling occurs, the HeNe intensity after the second polariser is approximately constant throughout the applied voltage pulse. On the other hand, if poling occurs, the HeNe intensity will be modulated, as shown in Fig. 4.4.

After the poling, the quality of the domain grating can be evaluated by measuring the efficiency of second-harmonic generation in the crystal. This is done with

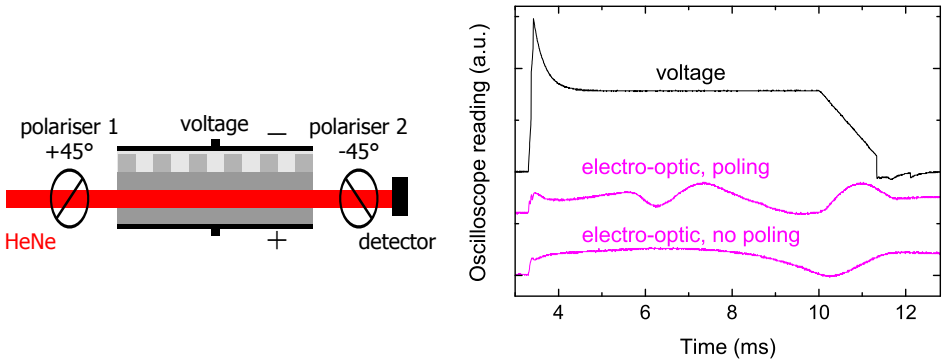

Fig. 4.4: When the crystal poles, the electro-optic effect modulates the photocurrent generated by the HeNe laser. This occurs for the middle trace, but not for the lower trace. The upper trace shows the applied voltage, which at the beginning of the pulse shows the RC response of the poling circuit.

a Ti:Sapphire laser, which can be tuned to wavelengths where QPM of some order occurs for the specific domain-inversion periodicity. A high relative SHG power that is sensitive to detuning from the QPM peak indicates that the domain grating is good. The homogeneity of the grating is tested by scanning the Ti:sapphire beam in the y and z directions and differences in the SHG is detected. Another method to evaluate the domain grating is to etch the crystal in an aqueous solution of KNO_3 and KOH [88]. The etching rate is faster at the c^- face compared to c^+, which makes the domain grating visible, as is shown in Fig. 4.5. However, this method only gives information about the grating structure on the surfaces and not in the bulk.

4.4 Fabrication of 3 mm-thick PPKTP crystals

The fabrication of PPKTP crystals with a period of $\Lambda = 38.86$ μm and a thickness of 3 mm in the **c** direction is described in paper III. These crystals are thicker than the typical PPKTP thickness of 1 mm and are suitable for high-power laser applications. The large crystal aperture allows for large beams with high average power, at the same time as the peak intensity is below damage threshold. A QPM period of 38.86 μm is designed for converting light at 1064 nm to around 2128 nm in a near-degenerate OPO. Both undoped and Rb-doped KTP crystals were used, where in the doped crystals 0.3 % of K^+ was replaced by Rb^+. The crystals were poled with a single 8 ms-long square-shaped pulse with an amplitude of 2.9 kV/mm for KTP and 5 kV/mm for Rb:KTP, with the results of one doped and one undoped crystal shown in Fig. 4.5. The crystal dimensions were 12 mm × 7 mm × 3 mm in the **a**, **b** and **c** directions, respectively, with periodically-poled regions of

approximately 9 mm × 5 mm × 3 mm.

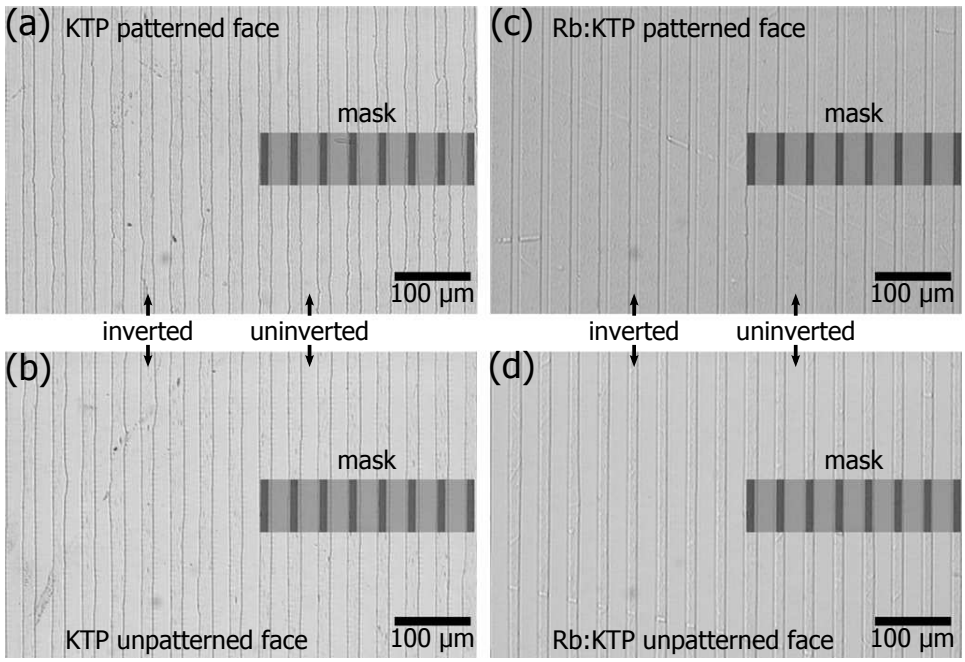

Fig. 4.5: Microscope images of the patterned and unpatterned sides of the 3 mm-thick periodically-poled KTP and Rb:KTP crystals. The crystals are poled all the way through. The undoped crystals obtains a duty cycle close to 50 %, whereas the Rb-doped crystals maintains the 30 % duty cycle of the mask [paper III].

One interesting feature is that the photolithographic mask used had openings with a duty cycle of 30 %. In KTP, this was a good choice, as the inverted domains have broadened from the 30 % of the mask opening to 49 %, *i.e.* close to the optimum duty cycle of 50 %. No such domain broadening occurs for the Rb-doped crystals. The domain grating in Rb:KTP maintains the duty cycle of the photolithographic mask, meaning that a mask with duty cycle of 50 % would have been a better choice. The effective nonlinearity is then, according to Eq. (2.52), reduced by a factor of $\sin(\pi D) \simeq 0.81$ for $D = 0.3$. It can also be seen in Fig. 4.5 that the domain walls are much straighter in Rb:KTP than in KTP, which is a property that makes Rb:KTP a promising material for crystals with submicrometre periods or for even thicker crystals. After the poling of these crystals, 5 mm-thick Rb:KTP crystals have been periodically poled [25].

4.5 Fabrication of submicrometre periods

With QPM periodicities below 1 μm, novel nonlinear light sources can be realised, *e.g.* mirrorless optical parametric oscillators. For the poling of submicrometre periods, KTP is a better material than *e.g.* $LiNbO_3$, as the domain growth in KTP is highly anisotropic, which allows for large domain sizes in the **b** and **c** directions and small sizes in the **a** direction [90]. In $LiNbO_3$, the domains tend to grow in shapes that follow the trigonal crystal structure [93], which makes it challenging to reduce the domain size in one spatial direction. Dense domain gratings in $LiNbO_3$ are normally limited to the surface and do not have the depth that is required for bulk devices [94].

The fabrication techniques for submicrometre periods are different compared to periods of a few or tens of micrometres. Due to diffraction, photolithographic masks are not suitable for patterning periods around 1 μm or below. Instead, the periodic pattern is created by the interference fringes formed by two UV beams, whose spatial period is determined by the UV wavelength and the angle α between the beams,

$$\Lambda = \frac{\lambda}{2\sin(\alpha/2)}, \tag{4.4}$$

where in our case a frequency-quadrupled Nd:YVO_4 laser gives the UV wavelength of $\lambda = 266$ nm.

Two methods for poling of submicrometre PPKTP are described in paper III. One is to make a periodic coercive-field grating by periodic in-diffusion of potassium ions. As the potassium content increases, the coercive field is reduced [95]. By leaving the crystal in a KNO_3 melt at 380 °C for 24 hours, the coercive field decreases by approximately 0.5 kV/mm [35]. With a periodic metallic pattern on the crystal c^- face, the in-diffusion of K^+ ions only occurs in the metal openings, creating regions with a periodic coercive-field difference. The crystal can then be poled at a field that periodically exceeds the coercive field in the crystal.

Another method is to use short electric pulses, typically with a length around one millisecond. The patterning is done similar to in Fig. 4.3, but where the interference pattern is used instead of the photolithographic mask. By using a short pulse with an amplitude that is substantially higher than the coercive field, the nucleation of domains is rapid at the c^- face and the short pulse length prevents the domains from spreading beyond the electrodes [91]. The drawback of this method is that the domains normally do not propagate all the way through to the c^+ face. The crystal that was used to realise the mirrorless optical parametric oscillator used in [16], and in paper IV, paper V and paper VI, was poled with a single 1.5 ms-long pulse with an amplitude of 2.6 kV/mm. An atomic force microscopy (AFM) image of this PPKTP crystal is shown in Fig. 4.6, revealing a crystal period of $\Lambda \simeq 800$ nm.

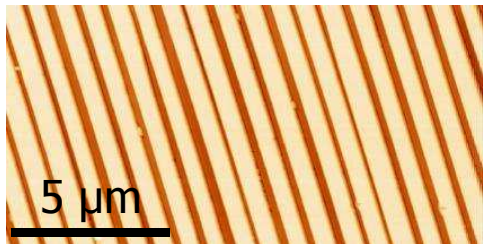

Fig. 4.6: Atomic force microscopy image of the patterned c face of a PPKTP crystal with $\Lambda \simeq 800$ nm, used for the mirrorless OPO in paper IV, paper V and paper VI.

4.6 Conclusions

Periodically-poled KTP and Rb:KTP crystals with a thickness of 3 mm and a poling periodicity of $\Lambda = 38.86$ μm have been fabricated. The crystals are designed for near-degenerate parametric down-conversion of pump light at 1064 nm with the largest second-order nonlinear coefficient d_{33}. The thickness of 3 mm makes them suitable for high-power applications. A low content of Rb-doping of KTP (here 0.3 %) affects the poling properties of the crystals. The ionic conductivity is greatly reduced and the coercive field increases by about a factor of 2. It is found that the Rb-doped crystals have straighter domain walls and maintain the periodicity of the photolithographic mask. This feature of Rb-doped crystals is promising for the poling of submicrometre periodicities in order to quasi-phase-match interactions with counterpropagating photons. It can also be used for the poling of even thicker crystals.

Chapter 5

Mirrorless optical parametric oscillators

Nonlinear three-wave interactions with counterpropagating photons can be used for the creation of narrowband parametric devices with unique spectral properties. These interactions, however, constitute an experimentally rather unexplored branch of nonlinear optics, due to the difficulty to achieve phase matching in a counterpropagating configuration. Some materials, like GaSe [96], possess a birefringence that is large enough to phase match interactions between two orthogonally-polarised co-propagating near-infrared waves in order to generate a counterpropagating wave at their frequency difference. These interactions are normally limited to backward waves in the THz region when the phase matching relies on the natural birefringence of the nonlinear medium. In order to increase the frequency of the backward wave, quasi-phase matching is needed, and it is for first-order QPM necessary to use a periodicity that is comparable to the pump wavelength.

The main feature that makes counterpropagating parametric interactions attractive is that they, unlike co-propagating interactions, may lead to optical parametric oscillation *without* the use of external mirrors or surface coatings. The necessary feedback is instead automatically provided through an internal distributed-feedback mechanism, which is established by the counterpropagating waves when the crystal is pumped above threshold. Furthermore, a counterpropagating phase-matching scheme intrinsically leads to parametric waves with narrow bandwidths, which *i.e.* could be used for the generation of ultrabright biphotons [97] for quantum applications. Before discussing the findings in paper IV, paper V and paper VI, a theoretical overview is given based on the original ideas behind the *mirrorless optical parametric oscillator* (MOPO) in [15] and the plane-wave modelling of the device in [98], as well as the first experimental realisation of a MOPO in PPKTP of submicrometre periodicity [16]. Throughout the chapter, the subscripts $j = p, f, b$ denote the pump, the forward and the backward parametric waves, respectively.

5.1 MOPO in homogeneous media

As in a conventional OPO, the sum of the energies of the parametric photons is equal to the energy of the pump photon,

$$\omega_p = \omega_f + \omega_b, \tag{5.1}$$

and phase matching is necessary for an efficient interaction,

$$\mathbf{k}_p = \mathbf{k}_f + \mathbf{k}_b. \tag{5.2}$$

Since $\mathbf{k}_p$ and $\mathbf{k}_f$ point in the forward direction, whereas $\mathbf{k}_b$ points in the backward direction, the scalar form of Eq. (5.2) reads

$$k_p = k_f - k_b. \tag{5.3}$$

The counterpropagating phase matching hence requires that the wave-vector magnitude the forward parametric wave is larger than the that of the pump, even though the pump has a higher frequency. This condition could be satisfied by employing BPM in a material with a large birefringence, where the forward parametric wave is generated orthogonally polarised to the pump, at the same time as the backward parametric wave has a wavelength that is much longer than those of the pump and the forward wave, $\lambda_p \simeq \lambda_f \ll \lambda_b$. The combined solution of Eq. (5.1) and Eq. (5.3) results in the following expression for the backward wavelength,

$$\lambda_b = \lambda_p \frac{n_f + n_b}{n_f - n_p}. \tag{5.4}$$

As opposed to conventional co-propagating parametric interactions, the configuration with counterpropagating parametric waves establishes an internal distributed-feedback mechanism, which leads to optical parametric oscillation without the need of external feedback from a cavity. A device based on this principle is called a *mirrorless optical parametric oscillator* (MOPO) and the principle of operation is somewhat similar to the oscillation obtained in distributed-feedback (DFB) lasers [99, 100]. However, unlike a DFB laser, which relies on the narrowband reflectivity obtained from a periodic modulation of the propagation constant, a MOPO is a truly mirrorless device and its operation is not based on reflections of any kind, but rather on counterpropagating phase matching. The MOPO was proposed in 1966 [15] with the suggestion to use trigonal selenium as the nonlinear medium, which is a uniaxial crystal with a trigonal crystal structure belonging to the point group 32. This material has a large birefringence, $n_o = 2.78$ and $n_e = 3.58$, a very large second-order nonlinearity and a wide transparency range between 0.8 μm and 20 μm. Type-II phase matching using $d_{26} = -d_{11} = -80$ pm/V could be achieved with ordinary pump and idler waves and an extraordinary signal wave, with an index of refraction depending on the propagation direction in the crystal given by Eq. (2.23). The effective nonlinearity of the interaction depends on the propagation

angle to the optical axis, θ, as $d_{eff} = d_{26} \cos\theta$. With a Q-switched Nd laser at 1.06 μm as pump source, the backward wavelength calculated from Eq. (5.4) and d_{eff} for the interaction are illustrated Fig. 5.1(a), together with phase-matching diagrams in Fig. 5.1(b) and (c). Dispersion has been neglected for the phase-matching calculations, which therefore are inaccurate, but however still show a correct qualitative behaviour.

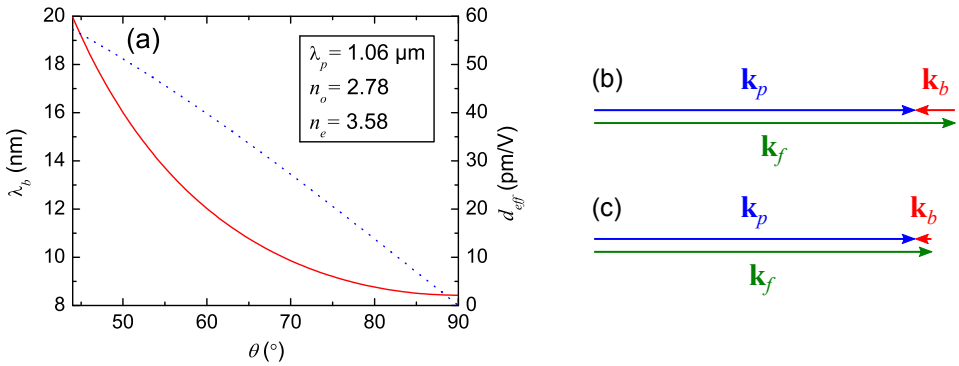

Fig. 5.1: (a) The backward-generated wavelength in trigonal selenium pumped at 1.06 μm (solid line) and the effective second-order nonlinearity for the interaction (dotted line) as function of the phase-matching angle θ. (b) Phase-matching diagram for $\theta = 90°$: $\lambda_b = 8.43$ μm and $\lambda_f = 1.21$ μm. (c) $\theta \simeq 44°$: $\lambda_b = 20.0$ μm, $\lambda_f = 1.12$ μm.

In theory, a widely-tunable source in the mid-infrared could be constructed with thresholds in the range of tens of MW/cm^2 in a 10 mm-long crystal. However, MOPOs have not yet been experimentally demonstrated in any homogeneous material. Instead, various schemes of backward DFG have been reported, *e.g.* the amplification of a backward mid-infrared beam in $NaNO_2$ [101] and backward DFG in the THz range in GaSe [96] between the pump and a forward signal. Hence counterpropagating nonlinear interactions in homogeneous media are possible, but it has so far always been necessary to have an input at either of the parametric waves for the interaction to take place. One reason for the difficulty to achieve parametric oscillation may be that the near-infrared forward wave and the far-infrared backward wave have very different diffraction properties, which leads to a poor overlap between the parametric beams. This could possibly be circumvented if the interaction is confined in a waveguide. Another approach, which has proven to be successful, is to instead of BPM use QPM with a periodicity comparable to the pump wavelength in order to increase the frequency of the backward wave to the mid infrared [16].

5.2 Plane-wave model of a nondegenerate MOPO

Analytical solutions of the counterpropagating nonlinear interaction can be obtained when the interacting fields are monochromatic plane waves [98], with the result of analytical expressions for the MOPO oscillation threshold and for the conversion efficiency. With the pump and the forward parametric wave propagating along x, and the backward wave propagating along $-x$, which is the propagation directions in KTP in our experiments, the coupled wave equations in the slowly-varying envelope approximation can be written in a normalised form [98],

$$\frac{da_f}{dx} = i\kappa a_p a_b^*, \tag{5.5}$$

$$\frac{da_b}{dx} = -i\kappa a_p a_f^*, \tag{5.6}$$

$$\frac{da_p}{dx} = i\kappa a_f a_b, \tag{5.7}$$

where the common coupling coefficient is

$$\kappa = \frac{d_{eff}}{2c}\sqrt{\frac{\omega_p\omega_f\omega_b}{n_p n_f n_b}}. \tag{5.8}$$

The amplitudes, a_j, are here normalised with respect to frequency and refractive index with the definition,

$$\tilde{E}_j(x,t) = \sqrt{\frac{\omega_j}{n_j}}a_j(x)e^{i(\pm k_j x-\omega_j t)} + c.c., \tag{5.9}$$

for $j \in \{p, f, b\}$. The sign in the exponential is $-$ for the backward wave and $+$ for the forward wave and the pump. First-order quasi-phase matching is assumed,

$$k_p = k_f - k_b + K_G, \tag{5.10}$$

where $K_G = 2\pi/\Lambda$. This condition, together with energy conservation, determines the frequencies of the parametric waves. It is here assumed that the MOPO is nondegenerate, *i.e.* $\omega_f \neq \omega_b$. The degenerate case is slightly different, as quasi-phase-matched back-conversion to the pump from the parametric waves is possible in both the $\pm x$ directions. With the normalised fields, the intensities are

$$I_j(x) = 2\varepsilon_0 c\,\omega_j \left|a_j(x)\right|^2. \tag{5.11}$$

The nonlinear medium is located between $x = 0$ and $x = L$ where the pump is incident on the face at $x = 0$. With no input fields at either of the parametric frequencies, the boundary conditions are $a_f(0) = 0$ and $a_b(L) = 0$. Solving the coupled wave equations, Eq. (5.5) - Eq. (5.7), with these boundary conditions leads to the following solutions for the parametric waves:

$$a_f(x) = ia_0 \sin\theta, \tag{5.12}$$

$$a_b(x) = a_0^* \cos\theta, \tag{5.13}$$

where the complex constant a_0 depends on the input pump intensity, $I_p(0)$, and θ is a real function of x with the boundary conditions $\theta(0) = 0$ and $\theta(L) = \pi/2$. The threshold is reached at the pump amplitude of $a_{p,th} = \pi/(2\kappa L)$, which translates into the threshold intensity

$$I_{p,th} = \frac{\varepsilon_0 c n_p n_f n_b \lambda_f \lambda_b}{2L^2 d_{eff}^2}. \tag{5.14}$$

Once above threshold, the pump is efficiently converted into parametric waves with the efficiencies $\eta_f = \eta\omega_f/\omega_p$ and $\eta_b = \eta\omega_b/\omega_p$, where $\eta \equiv 1 - I_p(L)/I_p(0)$ is the pump depletion, implicitly given by the integral equation

$$\int_0^{\pi/2} \frac{d\theta'}{\sqrt{1-\eta\sin^2\theta'}} = \frac{\pi}{2}\sqrt{I_p(0)/I_{p,th}}. \tag{5.15}$$

The efficiencies and the pump depletion are illustrated in Fig. 5.2(a). With η given by the input pump intensity through Eq. (5.15), the function θ is calculated from the relation

$$\int_0^{\theta} \frac{d\theta'}{\sqrt{1-\eta\sin^2\theta'}} = \frac{\pi x}{2L}\sqrt{I_p(0)/I_{p,th}}, \tag{5.16}$$

which close to threshold, $\eta \ll 1$, can be approximated with $\theta \simeq \pi x/(2L)$. The intensities of the parametric waves and the pump inside the crystal for different input pump intensities are shown in Fig. 5.2(b).

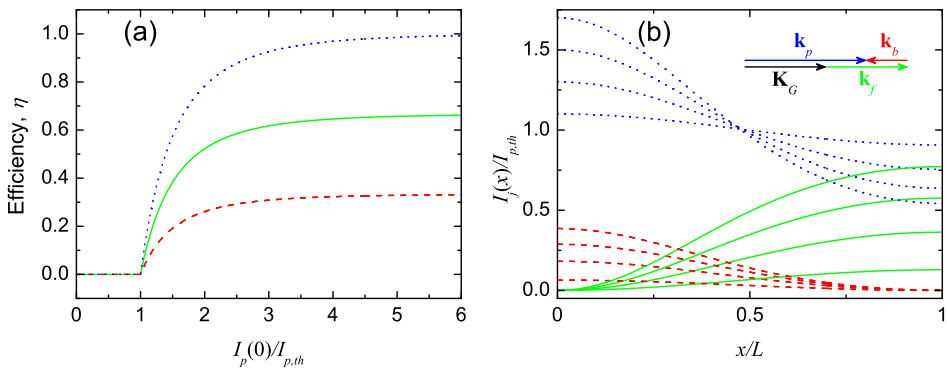

Fig. 5.2: (a) The pump depletion (dotted line) and the conversion efficiencies for the forward wave (solid line) and the backward wave (dashed line) as function of the pump intensity. (b) The intensity distribution throughout the crystal for the pump (dotted line), the forward wave (solid line) and the backward wave (dashed line) at the input pump intensities of $I_p(0)/I_{p,th} = 1.1, 1.3, 1.5$ and 1.7. The frequencies in both graphs are related as $\omega_b = \omega_f/2 = \omega_p/3$.

The mathematical description of the MOPO interactions is simple when the interacting waves are monochromatic and have a constant time dependence. In experiments, it is however necessary to use a pulsed pump in order to reach the oscillation threshold. The mathematical modelling is then more complicated and needs to be done numerically, as was done in the simulations in paper V and paper VI.

5.3 Experimental realisation of a MOPO

The first experimental demonstration of a MOPO was reported in 2007 [16], 41 years after the initial idea [15]. The experimental setup of a MOPO is schematically illustrated in Fig. 5.3 and only consists of the pump beam and the nonlinear crystal, which here is a 6.5 mm-long PPKTP crystal with a periodicity of $\Lambda \simeq 800$ nm.

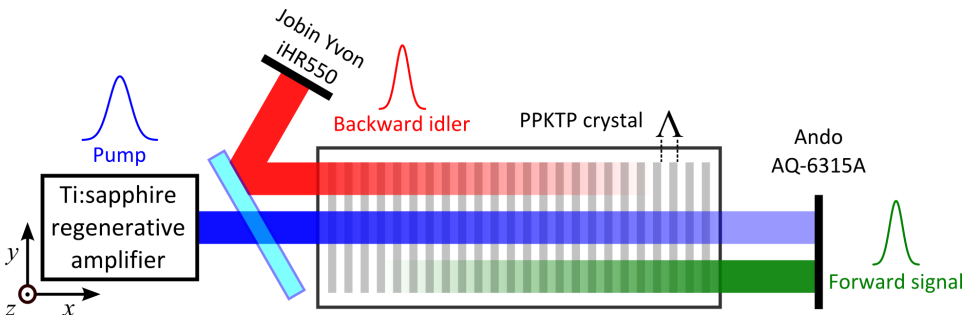

Fig. 5.3: The MOPO setup consists of only the pump source and the nonlinear crystal. A mirror, transparent for the pump and reflective for the idler, is placed in front of the crystal to pick up the backward idler beam. All beams overlap each other, but have been displaced vertically in the figure.

Due to the counterpropagating interaction, the MOPO has spectral properties that are very different compared to those of co-propagating OPOs. The backward wave intrinsically has a narrow bandwidth and the forward wave has a spectral width that is comparable to that of the pump. An example of the spectra of the pump and the parametric waves generated in a MOPO are found in Fig. 5.4.

The experimental setups in paper IV, paper V and paper VI were similar to the one shown in Fig. 5.3. The pump source was a Ti:sapphire regenerative amplifier (Coherent Legend), seeded with pulses from a modelocked oscillator (Spectra-Physics Tsunami) at the repetition frequency of 76 MHz. The pulses obtained a positive linear frequency chirp by adding positive group-delay dispersion (GDD) in a grating stretcher. They were then amplified at a repetition rate of 1 kHz, with the option to recompress the pulses by adding negative GDD in a grating compressor after the amplification. The system generates pulse energies of up to 1 mJ and can be tuned from 790 nm to 880 nm. Two alternative sets of stretcher-compressor

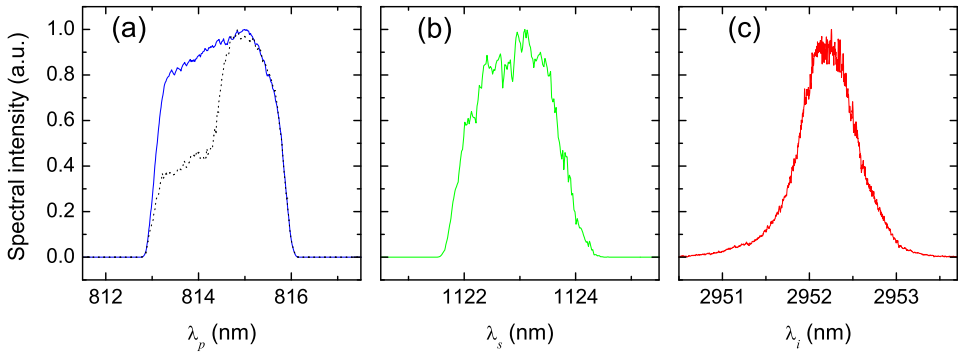

Fig. 5.4: (a) Depleted and undepleted pump spectrum, $\Delta\nu_p = 1.21$ THz. (b) The forward signal spectrum, $\Delta\nu_f = 410$ GHz. (c) The backward idler spectrum, $\Delta\nu_b = 23$ GHz (13 GHz deconvoluted) [paper V].

gratings with different dispersive properties can be used, where spatial filtering of the beam is performed in the stretcher in order to select the spectral width of the seed spectrum to amplify. The FWHM spectral width of the output can typically be chosen to be between 0.7 THz and 4 THz with FWHM pulse lengths from 1 ps to 100 ps for negatively-chirped compressed pulses and from 200 ps to 500 ps for uncompressed positively-chirped pulses. Temporal pulse characterisation of the compressed pump pulses was done by autocorrelation and the uncompressed pulses were measured with cross correlation with a 1 ps-long reference pulse.

The pump pulse energy was controlled with a waveplate-polariser setup before loosely focusing the beam to a $1/e^2$ intensity radius around 100 μm. The PPKTP crystal was placed at the focus, behind a partially reflective mirror that was used to pick up the idler beam. After the crystal, the spectra of the near-infrared pump and signal were measured with a fibre-coupled spectrometer (Ando AQ-6315A) and the mid-infrared idler spectrum was measured with a free-space imaging spectrometer (Jobin Yvon iHR550).

It should be pointed out that too short pump pulses are not suitable for MOPO pumping. The pump pulse should allow for the backward wave to interact with the pump throughout the whole crystal, meaning that the pump pulse length, Δt_p, should be longer than the time it takes for the pump to travel through the crystal, where it can start amplifying the backward wave at its input plane, plus the time it takes for the backward wave to travel through the crystal to its exit plane,

$$\Delta t_p \geq L\left(\frac{1}{v_{gp}} + \frac{1}{v_{gb}}\right). \tag{5.17}$$

For the wavelengths in Fig. 5.4, the minimum pump duration is $\Delta t_p \simeq 82$ ps. It is possible to use a shorter pulse, but the efficiency is then reduced. Eq. (5.17) is an estimate, as the particular temporal pump shape also comes into play.

5.4 Spectral MOPO characteristics

In the plane-wave model of a MOPO, the parametric waves are monochromatic in the approximation that phase matching strictly applies. Pumping with chirped pulses far from the transform limit gives rise to a large asymmetry in the bandwidths between the parametric waves, as can be seen in Fig. 5.4. As described in paper V, this asymmetry is related to how the phase modulation in the pump affects the phase modulation in the generated parametric waves. In a down-conversion process, the phases of the interacting waves are generally related as

$$\phi_p - \phi_f - \phi_b = -\pi/2, \tag{5.18}$$

which can be deduced from the coupled wave equations. In the MOPO case, it turns out that the phase of the backward-propagating wave essentially is constant as a result of the counterpropagating geometry. This can be shown by calculating the derivatives of the parametric frequencies with respect to the pump frequency. The derivatives are obtained by differentiating the QPM condition, Eq. (5.10), while keeping the grating periodicity constant and using the energy-conservation condition, Eq. (5.1), which results in the following expressions,

$$\frac{\partial\omega_f}{\partial\omega_p} = \frac{v_{gf}(v_{gb}+v_{gp})}{v_{gp}(v_{gb}+v_{gf})} \equiv 1+\varepsilon_1, \tag{5.19}$$

$$\frac{\partial\omega_b}{\partial\omega_p} = \frac{v_{gb}(v_{gp}-v_{gf})}{v_{gp}(v_{gb}+v_{gf})} \equiv -\varepsilon_1, \tag{5.20}$$

where v_{gj} $(j = p, f, b)$ are the group velocities. The plus signs in the denominators and in the numerator for the forward wave originate from the counterpropagating geometry. A dimensionless parameter, ε_1, is introduced as a measure of the group-velocity difference between the forward wave and the pump. For any value of the group velocities, the forward and backward derivatives have very different values as there still is a minus sign in the numerator of the backward equation. A low dispersion in the nonlinear medium implies that $|\varepsilon_1| \ll 1$ and the forward derivative is very close to unity and the backward tunability is consequently close to zero. Fig. 5.5 shows the tunability of the backward wave in KTP for a broad range of pump wavelengths and QPM periods.

Fig. 5.5 shows that in a counterpropagating configuration, the magnitude of the pump tunability for the backward wave is significantly lower than for the forward wave, regardless of the pump wavelength or QPM period. The backward wave contains approximately $|\partial\omega_b/\partial\omega_p|/|\partial\omega_f/\partial\omega_p| = |\varepsilon_1|/(1+\varepsilon_1) \simeq |\varepsilon_1|$ times the frequency content in the forward wave that originates from the frequency content in the pump. Compared to the pump and the forward wave, the temporal phase of the backward wave is then slowly varying and approximately constant, and truly constant when $\varepsilon_1 = 0$. Through the phase relation in Eq. (5.18), this implies that

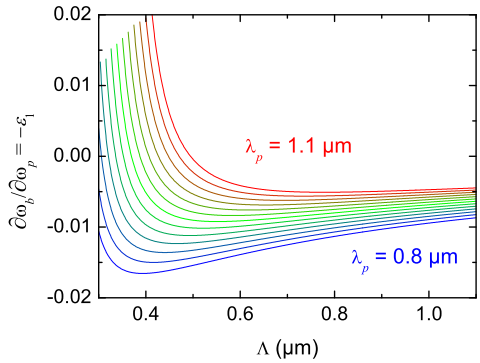

Fig. 5.5: The calculated pump tunability for the backward wave in KTP as function of the QPM period. The pump wavelengths range from 0.8 μm to 1.1 μm in steps of 25 nm.

the time derivatives of the phases in MOPOs generally are related as

$$\partial_t \phi_b \simeq 0, \tag{5.21}$$

$$\partial_t \phi_f \simeq \partial_t \phi_p. \tag{5.22}$$

In the case of strict equalities, the phase of the backward wave stays constant, implying that the backward-wave pulses are transform limited and the bandwidth is given by the temporal pulse duration. On the other hand, the phase of the forward wave varies with any changes in the pump phase, meaning that the forward wave essentially is a frequency-shifted replica of the pump. The same phenomena, *i.e.* that one parametric wave has a near-constant phase and that the phase of the other one essentially varies with the phase of the pump, may also occur in co-propagating configurations under very special conditions [102, 103]. It is then necessary to design the experiment so that the group velocity of one parametric wave is close to that of the pump, at the same time as the pump and the other parametric wave have a large group-velocity difference. The latter condition is automatically fulfilled in a counterpropagating configuration, as one wave counterpropagates the pump, and the former condition is approximately fulfilled if the dispersion in the nonlinear medium is low.

Experimental verification of the phase-modulation transfer

The large asymmetry in phase modulation between the forward and backward parametric waves was experimentally verified in paper V. A 6.5 mm-long PPKTP crystal with a period of 800 nm was pumped with positively-chirped pulses of a FWHM length of 480 ps, generating a forward signal and a backward idler with pulse lengths of 160 ps. The MOPO threshold was reached at $I_{p,th} \simeq 0.8$ GW/cm^2 and the spectra generated at $1.3I_{p,th}$ are the ones shown in Fig. 5.4. Both the pump and the

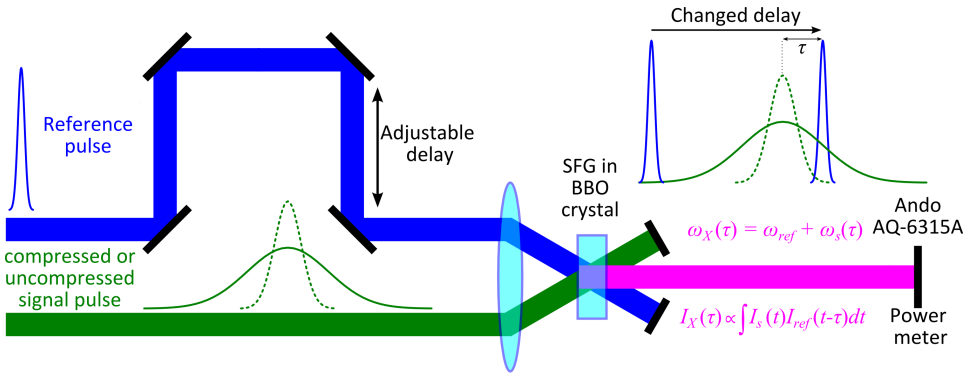

Fig. 5.6: The cross-correlation setup used in paper V for measurements of the chirp rates and the temporal intensity profiles of the forward signal and the pump.

forward signal were temporally and spectrally analysed by cross correlation with a short reference pulse in a BBO crystal. The principle is to measure the sum-frequency intensity and spectrum generated by the forward signal (or the pump) and the reference pulse as the reference pulse is scanned through the signal (or pump) pulse. The beams are designed to have a common focus inside the nonlinear crystal and the timing between the pulses can be changed by varying the delay in the reference arm, as is schematically illustrated in Fig. 5.6.

The reference pulse interacts with a part of the signal pulse and the sum-frequency spectrum and intensity, in Fig. 5.6 denoted $\omega_X(\tau)$ and $I_X(\tau)$, provide information about the local frequency and intensity in the signal pulse. The resolution is set by the width of the reference pulse, which in this case was 1 ps, *i.e.* more than a factor of 100 shorter than the pump and the signal. By scanning the reference pulse through the pump and the signal pulses, the detected shift of the peak in the sum-frequency spectrum is illustrated in Fig. 5.7(a). For both the pump and the forward signal, there is an approximately linear frequency shift in the sum frequency as the delay is changed. This is to be expected for the pump, as the pulses have passed through a grating stretcher, which adds a linear chirp. It is also expected for the signal, as the phase modulation should be transferred from the pump with the multiplication of $1 + \varepsilon_1 \simeq 1.01$. The measured chirp rate was $\partial\omega_p/\partial t \simeq 15.7$ mrad/ps^2 for the pump and about 1.6 % higher for the signal, $\partial\omega_f/\partial t \simeq 16.0$ mrad/ps^2, which within the experimental resolution verifies the expected transfer of phase modulation from the pump to the forward parametric wave. The chirp of the backward idler was not directly measured. However, as a result of energy conservation, the idler chirp must be weak and has an opposite sign compared to the chirp of the pump, as expected from Eq. (5.21).

It can also be pointed out that the positive chirp in the pump explains why the pump spectrum in Fig. 5.4 is not depleted uniformly. At the leading end of the pulse,

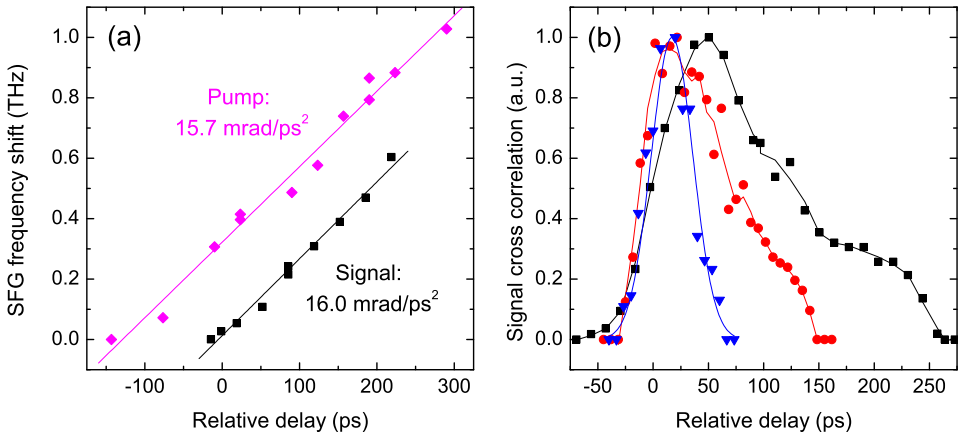

Fig. 5.7: (a) Both the pump and the forward signal are linearly chirped, where the chirp rate of the signal is slightly faster than that of the pump. (b) Cross-correlation traces of the uncompressed signal pulses and two compressed pulses at different compressor settings.

which here contains the longer wavelengths, no depletion occurs as the distributed feedback has not had the time to establish and the MOPO is not operational. Once the MOPO starts operating, the pump is efficiently depleted, which here occurs for wavelengths shorter than 814.7 nm. This also causes the signal spectrum to be narrower than the pump spectrum, as the whole pump spectrum is not depleted.

Another way to confirm that a linearly-chirped pump gives rise to a linearly-chirped forward signal is to verify that the signal pulses are compressible in the time domain. This was investigated in paper V, where the signal pulses passed through a grating compressor with negative GDD. The cross-correlation traces for an uncompressed pulse and for two different amounts of negative GDD in the compressor are illustrated in Fig. 5.7(b), which shows that compression occurs.

Numerical verification of the phase-modulation transfer

The transfer of phase modulation to the forward wave was also numerically simulated in paper V and paper VI by solving the coupled wave equations in the counterpropagating configuration:

$$(\partial_t + v_{gp}\partial_x + \gamma_p + i\beta_p\partial_{tt})\, A_p = -\sigma_p A_f A_b, \tag{5.23}$$

$$(\partial_t + v_{gf}\partial_x + \gamma_f + i\beta_f\partial_{tt})\, A_f = \sigma_f A_p A_b^*, \tag{5.24}$$

$$(\partial_t - v_{gb}\partial_x + \gamma_b + i\beta_b\partial_{tt})\, A_b = \sigma_b A_p A_f^*. \tag{5.25}$$

Here $\sigma_j \equiv 2\pi d_{eff} v_{gj}/(\lambda_j n_j)$, γ_j and $\beta_j \equiv v_{gj}\beta_{2j}/2$ are the coupling, damping and dispersion coefficients, respectively. This form of the coupled wave equations is mathematically more complex and physically more realistic compared to the monochromatic model, Eq. (5.5) - Eq. (5.7), as the effects of the temporal and spectral shapes of the waves, as well as the dispersive properties of the nonlinear medium, are taken into account. The coupled equations were solved for different spectral and temporal pump shapes in a model PPKTP crystal of length 6.5 mm and $d_{eff} = 9$ pm/V. In order to simulate the experiment that yielded the spectra in Fig. 5.4, the input pump amplitude was linearly-chirped with a similar pulse length and the spectrum shown in Fig. 5.8(a). An input pump intensity of 1.1 GW/cm^2 generated the forward signal spectrum shown in Fig. 5.8(b) and the narrow backward idler spectrum in Fig. 5.8(c). The last part of the figure shows the phase distribution of the three waves inside the crystal at a given time. Clearly, the phase of the backward idler is in principle constant throughout the crystal and that of the forward signal is locked to the pump, all in very good agreement with experiments and theory.

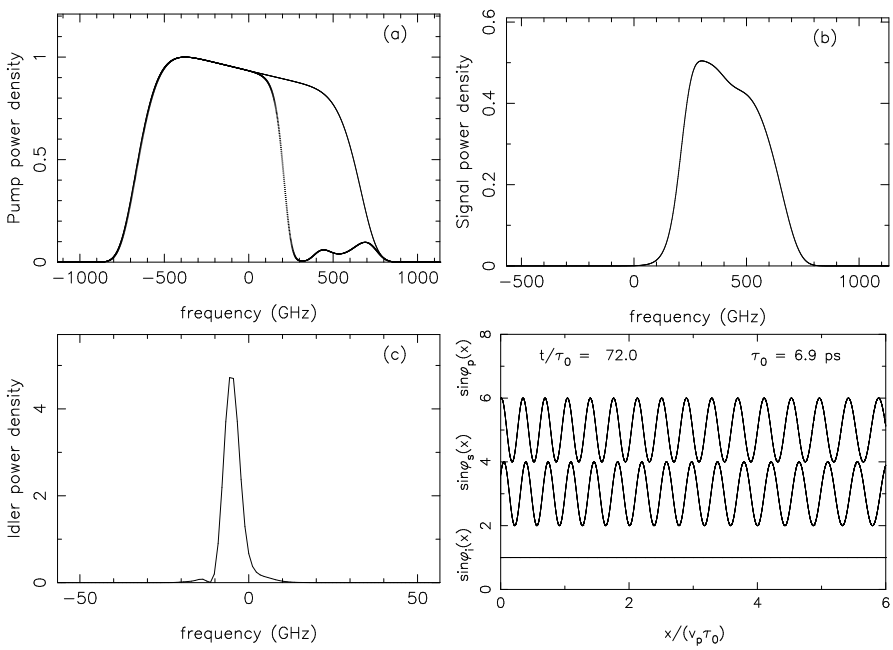

Fig. 5.8: A simulation of a MOPO at the pump intensity of 1.1 GW/cm^2. The input pump (spectral width, 1.27 THz) generates a forward signal (440 GHz) and a backward idler (6.5 GHz). The zeros on the frequency scales correspond to 814.5 nm, 1125 nm and 2952 nm for the pump, signal and idler. The last figure shows the phase distributions inside the crystal at a given time, where the x axis is given in mm [paper V].

Effects of dispersion and pump spectrum

In paper V, the MOPO is pumped with relatively narrowband pulses with a spectral width of 1.2 THz. In order to investigate the effects of a broad pump bandwidth, the MOPO was pumped with broadband pulses in paper VI. The regenerative amplifier settings were modified to let through a large part of the oscillator spectrum, resulting in pump pulses with a bandwidth of 4.0 THz. The temporal FWHM pulse length was 50 ps and the MOPO threshold was reached at an intensity of $I_{p,th} = 1.5$ GW/cm^2. Fig. 5.9 illustrates the spectra at $1.7I_{p,th}$, generating a forward signal and a backward idler with temporal lengths around 20 ps and bandwidths of 1.62 THz and 59 GHz, respectively. The pump was negatively chirped, which explains why the longer wavelengths in Fig. 5.9 are the ones converted into signal and idler. Compared to in Fig. 5.4, the pump chirp rate was changed by a factor of -31. The strong pump chirp makes the backward idler bandwidth to be slightly dominated by chirp rather than by the temporal length.

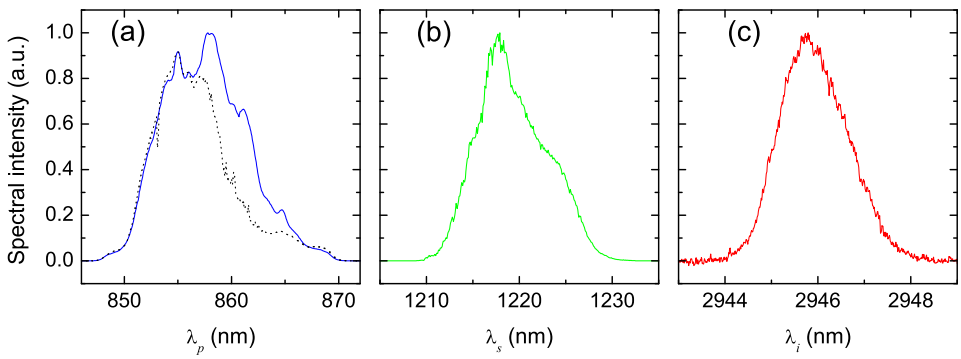

Fig. 5.9: (a) Depleted and undepleted pump spectrum, $\Delta\nu_p = 3.98$ THz. (b) The forward signal spectrum, $\Delta\nu_f = 1.62$ THz. (c) The backward idler spectrum, $\Delta\nu_b = 59$ GHz [paper VI].

In paper VI, the effect of the pump bandwidth on the MOPO efficiency is numerically studied by using linearly-chirped Gaussian pump pulses with the same temporal length of 52 ps, but with different chirp rates. With ε_1 as defined in Eq. (5.20), the dispersion in the PPKTP crystal at the interacting wavelengths, which are the same as in Fig. 5.9, is such that the group-velocity difference between the forward wave and the pump results in $\varepsilon_1 \simeq 9.8 \cdot 10^{-3}$. For these dispersion conditions, it is found that the conversion efficiency in the MOPO decreases with an increased pump spectral width, as is illustrated in Fig. 5.10 where the spectral width is increased from the transform limit up to about 5 THz. It is also found, by artificially manipulating the dispersion, that the reduction in the efficiency does not occur in the case where the group velocities of the forward wave and the pump are matched, $v_{gf} = v_{gp}$, which leads to $\varepsilon_1 = 0$. The height of the plus (+) symbols

in the figure denotes fluctuations in the conversion efficiency that depend on the initial phase of the pump pulse. As this is a random parameter for the pump source used in the corresponding experiments, averaging has been done over several initial phases. The reduction in the efficiency with an increased spectral width happens because the spectral components in the forward signal move slightly faster than those in the pump. This temporal walk-off reduces the effective interaction length and thereby the efficiency of the interaction. This does not occur when there is no group-velocity difference between the pump and the forward wave and the efficiency is therefore not affected.

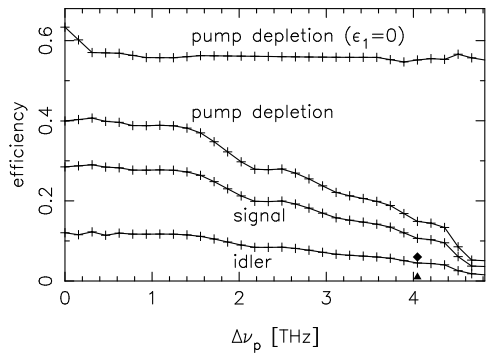

Fig. 5.10: Pump depletion and conversion into signal (1217.9 nm) and idler (2945.7 nm) as function of the pump spectral width for linearly-chirped pulses at the pump intensity of 2.57 GW/cm^2. When the dispersion is changed so that $\varepsilon_1 = 0$, the pump depletion is not affected by the pump bandwidth. The triangle and the diamond mark the pump depletion for a pump with stochastic phase modulation at the pump intensities of 2.57 GW/cm^2 and 3.5 GW/cm^2, respectively [paper VI].

In simulations, any phase modulation can be incorporated in the pump pulses. It was numerically shown in paper VI that MOPOs can operate when pumped with pulses of stochastic phase modulation. The forward wave absorbs the stochastic phase jumps and allows the backward wave to be almost free of phase modulation. However, Fig. 5.10 shows that the stochastic phase modulation has a more detrimental effect on the MOPO efficiency compared to a deterministic phase modulation in the form of a linear chirp. For the eventual experimental verification of this phenomenon, a pump source is needed that delivers pulses with a stable and high peak power, at the same time as the pulses are incoherent. Good candidates for such a pump source are figure-eight fibre lasers operating in noise-like pulse mode with pulse lengths around 1 ns [104], which could be amplified to the required energies in fibre amplifiers.

A MOPO with group-velocity matching

According to Fig. 5.10, group-velocity matching between the forward wave and the pump increases the MOPO efficiency. It is therefore interesting to realise such a MOPO experimentally, which could be done in KTP by using pump and forward wavelengths on different sides of the maximum on the group-velocity curve in Fig. 5.11. Group-velocity matching is obtained *e.g.* with the pump at 1060 nm and a forward idler around 2883 nm. This configuration generates a backward signal at 1676 nm and requires a QPM period as short as 456.7 nm, which currently is beyond the state-of-the-art poling technology in KTP.

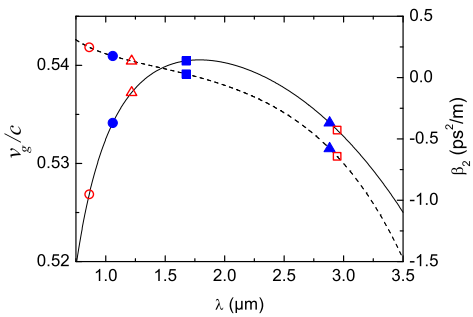

Fig. 5.11: Group velocity (solid line) and group-velocity dispersion (dashed line) for z-polarised waves in KTP. The symbols denote the pump (circle), the forward wave (triangle) and the backward wave (square) for the wavelengths in Fig. 5.9 (open symbols) and for the group-velocity-matched wavelengths (solid symbols) [paper VI].

As a result of different group-velocity dispersion around the wavelengths of the pump and the forward wave, there is a still a small amount of phase modulation in the backward wave. The value of $\partial\omega_b/\partial\omega_p$ varies within the pump bandwidth and is only strictly zero for one of the frequencies within the pump bandwidth. Instead of depending on the group-velocity difference, which here is zero, the phase modulation is approximately given by the pump bandwidth and the difference in GVD coefficients, which never is zero in KTP, as shown in Fig. 5.11. The variation in $\partial\omega_b/\partial\omega_p$ within the pump bandwidth can be approximated with

$$\left.\frac{\partial\omega_b}{\partial\omega_p}\right|_{\omega_p+\delta\omega_p} \simeq \delta\omega_p \left.\frac{\partial^2\omega_b}{\partial\omega_p^2}\right|_{\omega_p} = \delta\omega_p \frac{v_{gf}v_{gb}}{v_{gf}+v_{gb}}\left(\beta_{2f}-\beta_{2p}\right). \tag{5.26}$$

Group-velocity matched configurations enable for pumping with highly incoherent beams, as is shown by running a simulation with a 50 ps-long pump pulse with a FWHM bandwidth of 23 THz and stochastic phase modulation. The result is illustrated in Fig. 5.12, showing that the backward signal has a temporal length of 18 ps and a bandwidth of only 23 GHz, which means that the backward signal is transform limited, despite the broad pump bandwidth.

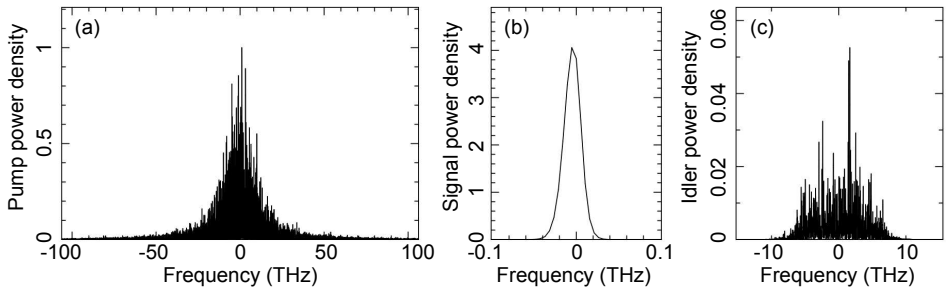

Fig. 5.12: A simulation of a MOPO at the pump intensity of 4 GW/cm^2. The input pump (spectral width, 23 THz) with random phase modulation generates a forward idler (10 THz) and a backward signal (23 GHz). The zeros on the frequency scales correspond to 1060 nm, 1676 nm and 2883 nm for the pump, signal and idler, respectively. The group-velocity matching makes the backward wave a factor of 1000 narrower than the pump [paper VI].

5.5 Output wavelengths from a MOPO

In the case of a quasi-phase-matched interaction, the parametric wavelengths are determined by energy conservation, Eq. (5.1), and quasi-phase matching, Eq. (5.10). The mutual solution of the two equations leads to the following relation between the QPM period and the interacting wavelengths:

$$\frac{1}{\Lambda} = \frac{1}{\lambda_p}(n_p - n_f) + \frac{1}{\lambda_b}(n_f + n_b), \tag{5.27}$$

where the forward wavelength has been eliminated by energy conservation. The MOPO wavelengths in KTP, calculated from Eq. (5.27) as function of either the pump wavelength or the QPM period, are shown in Fig. 5.13. The pump wavelength and the QPM periodicity determine which of the forward and the backward waves that carries the most energy, *i.e.* which is the signal and which is the idler. A backward signal requires that $\Lambda < \lambda_p/n_p$, whereas a reversed inequality results in a backward idler and the degenerate case $\lambda_f = \lambda_b = \lambda_p/2$ is obtained when $\Lambda = \lambda_p/n_p$. A general feature of MOPOs based on QPM is that the backward wavelength has a very strong dependence on the QPM period and is only slightly affected by the choice of pump wavelength. This is especially pronounced in cases where the dispersion is low, which is deduced by rewriting Eq. (5.27) as

$$\frac{1}{\lambda_b} = \frac{1}{2\bar{n}}\left(\frac{1}{\Lambda} - \frac{\Delta n}{\lambda_p}\right), \tag{5.28}$$

where $\Delta n \equiv n_p - n_f$ and $\bar{n} \equiv (n_f + n_b)/2$. The resulting backward wavelength can be seen be given by one contribution from the QPM grating and one contribution

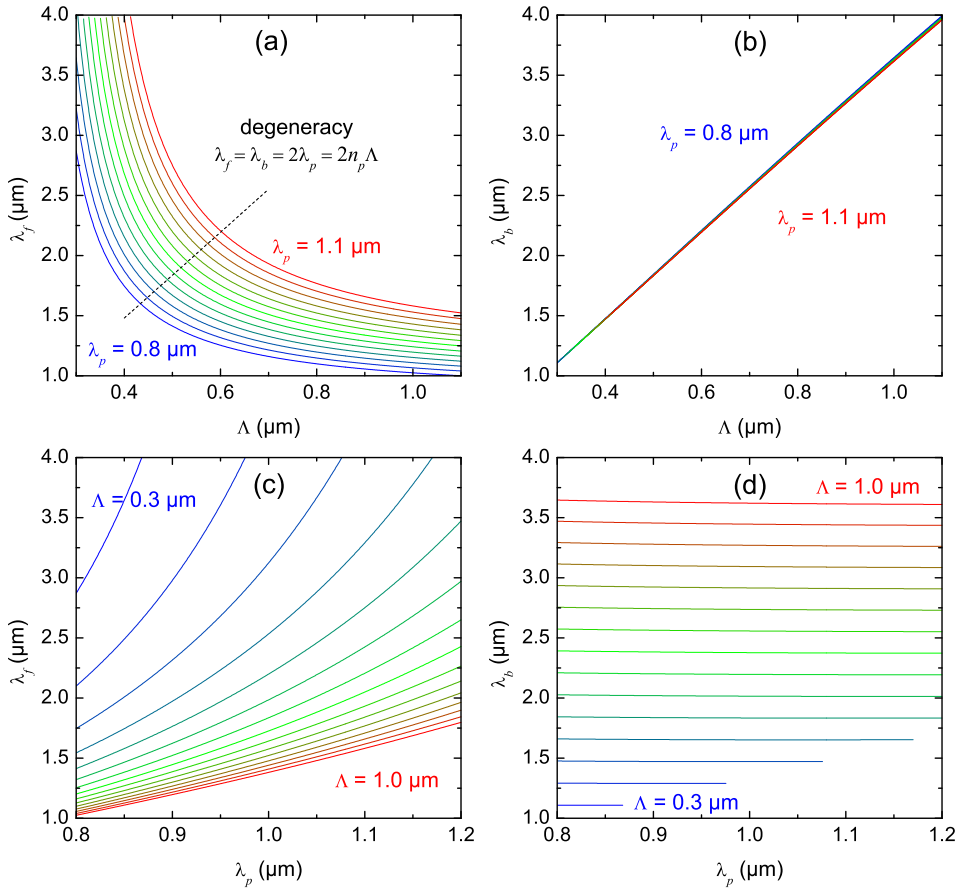

Fig. 5.13: The forward (a) and backward (b) wavelengths as function of the QPM period. The pump wavelengths range from from 0.8 μm to 1.1 μm in steps of 25 nm. The forward (c) and backward (d) wavelengths as function of the pump wavelength. The QPM periods range from 0.3 μm to 1.1 μm in steps of 50 nm. As KTP absorbs around 4.3 μm, the calculations are performed for parametric pairs where both wavelengths are below 4 μm.

from the pump and the dispersion, where the influence of the grating-related part typically is much stronger. In the case of KTP, where all interacting wavelengths are z polarised, n_z decreases monotonically from 1.84 at 800 nm to 1.78 at 3 μm, *i.e.* a decrease with 4 % (see Fig. 4.2). With $\Lambda \simeq 800$ nm and a Ti:sapphire pump, $\lambda_p \simeq \Lambda$, the difference in refractive index between the pump and the forward wave is in the interval $0.01 < \Delta n < 0.02$, meaning that the grating part is about 50 to 100 times larger than the pump-dispersive part. The backward wavelength is hence

to a good approximation directly given by the grating period and the average index of refraction,

$$\lambda_b \simeq 2\bar{n}\Lambda. \tag{5.29}$$

This gives an approximate expression for the required modulation period for a desired backward wavelength. The strong dependence of λ_b on Λ, and the weak dependence on λ_p, can be observed in Fig. 5.13(b) and Fig. 5.13(d). As a result of energy conservation, the dependence for the forward wave on the pump is the opposite. In Fig. 5.13(a), it can be seen that an increase in the pump wavelength essentially shifts the forward-wavelength curve vertically to longer wavelengths. As the pump wavelength increases, so does the forward wavelength, as shown in Fig. 5.13(c). In terms of frequency rather than wavelength, the frequency shift of the forward wave is approximately equal to the frequency shift of the pump, which is experimentally verified in the next section.

Clearly, the output wavelengths of a MOPO change when the pump is tuned or the QPM period is changed. Two other ways to tune MOPOs is to vary the crystal temperature and to rotate the QPM grating with respect to the pump beam. The tuning methods are described in the four sections below.

5.6 Pump tuning

Due to the counterpropagating quasi-phase matching, the frequency of the forward wave changes much faster than that of the backward wave when the pump is tuned, which could be seen in Fig. 5.13 and also from the asymmetries in $\partial\omega_f/\partial\omega_p$ and $\partial\omega_b/\partial\omega_p$. A shift of the pump of $\delta\omega_p$ shifts the forward and backward frequencies with an amount $\delta\omega_j$ $(j = f, b)$, given by

$$\delta\omega_j = \left\langle \frac{\partial\omega_j}{\partial\omega_p} \right\rangle \delta\omega_p, \tag{5.30}$$

where the angle bracket denotes the average for the pump frequencies between ω_p and $\omega_p + \delta\omega_p$. Pump tuning of a MOPO was experimentally measured for the crystal with $\Lambda \simeq 800$ nm and the spectra generated by three different pump wavelengths are shown in Fig. 5.14. From the spectra labelled with a to the ones labelled with b and c, the position where maximum pump depletion occurs is tuned by -19.82 THz and -26.79 THz, causing the forward signal to shift by -20.04 THz and -27.05 THz, whereas the backward idler shifts by only 0.22 THz and 0.26 THz. This tuning behaviour, using only two pump wavelengths, was shown in paper VI and was verified in [16] for a smaller frequency range. The forward signal tunes approximately 1 % faster than the pump and the backward idler tunes at only -1 % of the pump tuning rate, which is to be expected from the values of $\partial\omega_j/\partial\omega_p$.

In order to compare theory and experiments, Fig. 5.15 shows the pump tuning curves calculated with the dispersion from [86] for QPM periodicities between 795 nm and 815 nm in steps of 2.5 nm. The four experimental points suggest that the

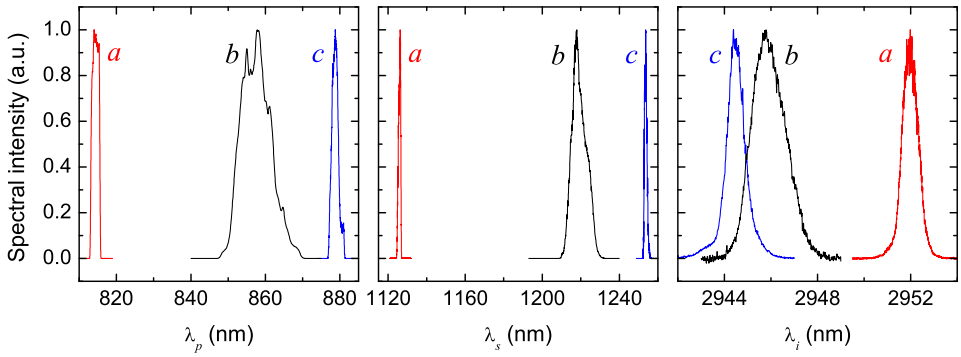

Fig. 5.14: Pump tuning of a MOPO in PPKTP with $\Lambda \simeq 800$ nm. The forward signal tunes about 1 % faster than the pump, whereas the backward idler tunes at only 1 % of the pump tuning rate in the opposite direction. The symbols *a*, *b* and *c* denote which of the parametric waves that corresponds to which of the three pumps.

QPM period is just above 805 nm, which is within 1 % from the 800 nm deduced by atomic force microscopy of the crystal (Fig. 4.6).

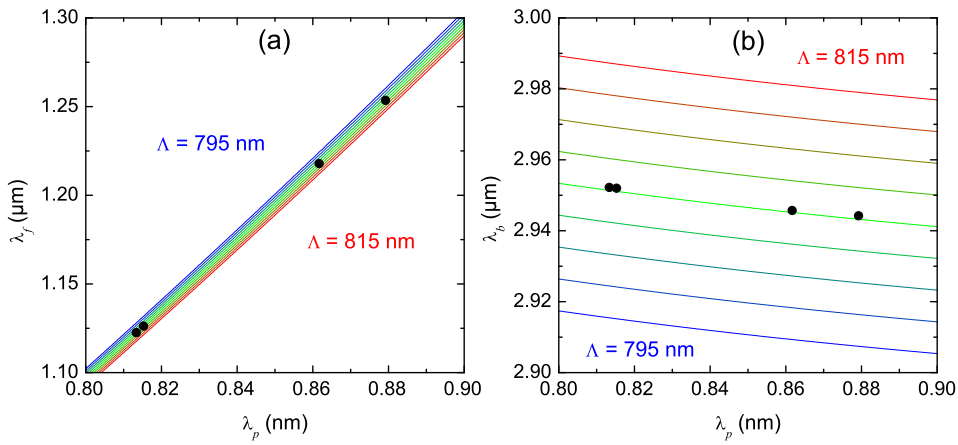

Fig. 5.15: The graphs show the calculated forward (a) and backward (b) wavelengths for QPM periodicities between 795 nm and 815 nm in steps of 2.5 nm. The four experimental points and the calculations with the KTP dispersion from [86] suggest that the QPM period is just above 805 nm.

5.7 Grating tuning

Another way to change the output wavelength is to change the grating periodicity. The rate of change of the backward frequency with respect to the QPM period can be calculated by differentiating the quasi-phase-matching condition with respect to the QPM period while keeping the pump frequency constant,

$$\frac{\partial \nu_b}{\partial \Lambda} = -\frac{\partial \nu_f}{\partial \Lambda} = -\frac{1}{\Lambda^2}\frac{v_{gf} v_{gb}}{v_{gf} + v_{gb}}, \tag{5.31}$$

which for KTP is illustrated in Fig. 5.16. The pump wavelength only affects the grating tunability slightly and indirectly through the dispersion at the parametric wavelengths and the derivative has an inverse-square dependence on the QPM period. For 800 nm $< \lambda_p <$ 900 nm and $\Lambda \simeq 805$ nm, the grating tunability is $\partial\nu_b/\partial\Lambda \simeq -124$ GHz/nm. The backward bandwidth in paper V was $\Delta\nu_b \simeq 13$ GHz, which means that a shift in the QPM periodicity of only 1 nm would tune the backward wave with almost 10 bandwidths.

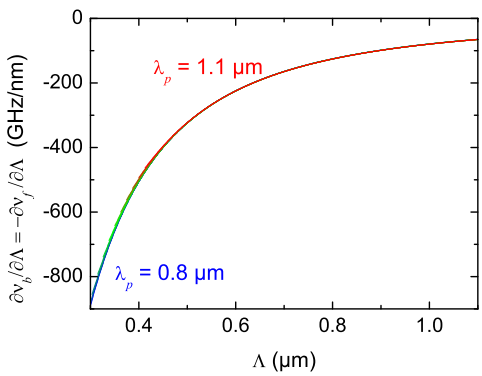

Fig. 5.16: The rate of change of MOPO output frequency with respect to the QPM period is essentially independent of the pump wavelength.

5.8 Temperature tuning

The MOPO output wavelengths can be tuned by changing the crystal temperature. Two separate effects contribute to the MOPO tuning: the temperature dependence of the refractive index, $n(\lambda, T)$, and the change in QPM periodicity due to the thermal expansion of the crystal. A change in the crystal temperature of ΔT gives rise to a change in the QPM period of $\Delta\Lambda \simeq \alpha\Lambda\Delta T$, where α is the thermal-expansion coefficient in the direction of the grating. The temperature tuning of a MOPO is calculated by differentiating the quasi-phase-matching condition, Eq.

(5.10), with respect to temperature while keeping the the pump frequency constant. By inserting the energy-conservation condition, the rate of change of the parametric frequencies with respect to temperature is

$$\frac{\partial \nu_b}{\partial T} = -\frac{\partial \nu_f}{\partial T} = -\frac{1}{n_f + n_b}\left[\nu_f\left(\frac{\partial n_p}{\partial T} - \frac{\partial n_f}{\partial T}\right) + \nu_b\left(\frac{\partial n_p}{\partial T} + \frac{\partial n_b}{\partial T}\right) + \frac{c\alpha}{\Lambda}\right], \quad (5.32)$$

The temperature tuning of a MOPO in a PPKTP crystal with $\Lambda \simeq 805$ nm is presented in Fig. 5.17(a). By varying the crystal temperature between 18 °C and 80 °C, the parametric waves tune around ±100 GHz, at an average rate of $\Delta\nu_i/\Delta T = -\Delta\nu_s/\Delta T \simeq -1.60$ GHz/K. The crystal is only heated from below, which explains the slight broadening of the backward wave that occurs during the heating. ±1.60 GHz/K is a slow temperature-tuning rate, meaning that the temperature cannot be used as a parameter for broad tuning, but is limited to fine tuning of the narrowband backward wave. On the other hand, this implies that the MOPO output is not sensitive to temperature fluctuations and that MOPOs are environmentally-stable devices.

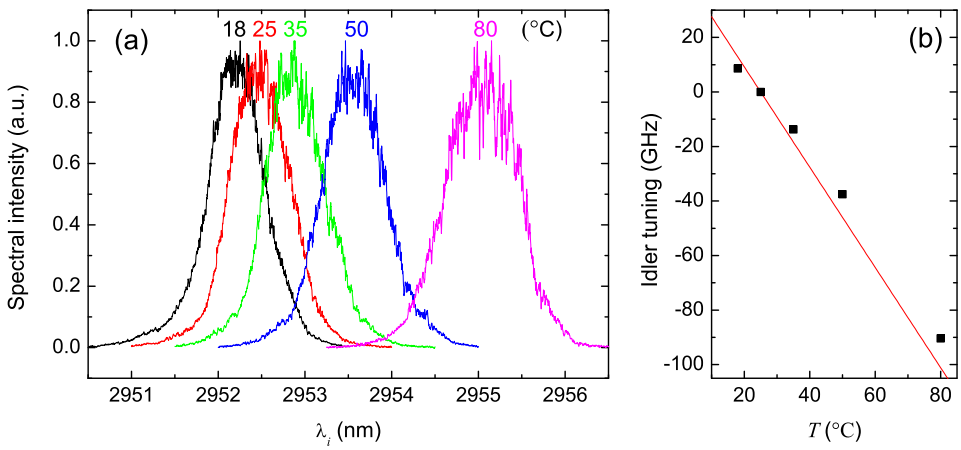

Fig. 5.17: (a) Temperature tuning of a MOPO between 18 °C and 80 °C, measured on the backward wave. (b) Experimental values and the tuning calculated from Eq. (5.32), with 25 °C as the reference temperature.

In order to compare the measured temperature tuning with theory, the temperature tuning was calculated by using the value of $\partial n_z/\partial T$ given by Eq. (5.32) and the thermal-expansion coefficient in the x direction of KTP of $\alpha \simeq 9.5 \cdot 10^{-6}$/K [87]. The calculated values and the experimental points are presented in Fig. 5.17(b) and show similar behaviour. The average value of the calculated temperature tuning in the interval is $\Delta\nu_i/\Delta T \simeq -1.84$ GHz/K, where approximately equal parts are attributed to the thermal expansion (-0.94 GHz/K) and to the temperature-induced change in the refractive index (-0.89 GHz/K).

5.9 Angular tuning

The angular tuning of a MOPO by the use of noncollinear interactions is explained in paper IV. Noncollinear interactions in a MOPO are fundamentally different from noncollinear interactions in co-propagating OPOs, as the nonlinear interaction in a MOPO self-selects the parametric wavelengths and their propagation directions. The parametric waves are here referred to as signal and idler, and the illustrations correspond to the case of a counterpropagating idler. As in noncollinear co-propagating interactions, energy conservation and vectorial quasi-phase matching apply:

$$1/\lambda_p = 1/\lambda_s + 1/\lambda_i, \tag{5.33}$$

$$n_p/\lambda_p = (n_s/\lambda_s)\cos\varphi_s + (n_i/\lambda_i)\cos\varphi_i + (1/\Lambda)\cos\varphi_G, \tag{5.34}$$

$$0 = (n_s/\lambda_s)\sin\varphi_s + (n_i/\lambda_i)\sin\varphi_i + (1/\Lambda)\sin\varphi_G, \tag{5.35}$$

where, as shown in Fig. 5.18(a), the angles are defined with the pump direction as the reference direction.

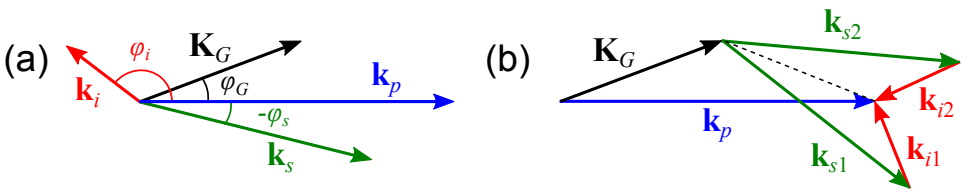

Fig. 5.18: (a) Definitions of the noncollinear angles, positive in the clockwise direction from the pump. (b) A general configuration that is a solution of Eq. (5.33) - Eq. (5.35).

λ_p and Λ are given by the pump source and the engineered crystal. The angle between the pump and the grating, φ_G, can be freely varied by rotating the crystal, meaning that there are four unknown variables: λ_s, λ_i, φ_s and φ_i. However, there are only three constraints, so the number of solutions of Eq. (5.33) - Eq. (5.35) is infinite.

For given wavelengths λ_s and λ_i, there are two geometrically nonequivalent solutions consistent with energy conservation and QPM, obtained by mirroring the signal and idler wave vectors for one phase-matched pair in the vector $\mathbf{k}_p - \mathbf{K}_G$, shown as a dashed line in Fig. 5.18(b). For noncollinear interactions in a singly-resonant co-propagating OPO, the direction of the resonant parametric wave is determined by the resonant cavity and is not a free parameter. This fixes the value of either φ_s or φ_i and a unique solution of Eq. (5.33) - Eq. (5.35) is obtained. Strictly speaking, the dispersion in the nonlinear medium may be such that two solutions are simultaneously possible with two signals and two idlers at different wavelengths [105, 106].

The situation is different in a MOPO. There is no cavity to fix a propagation direction and it is not obvious how, or if, the distributed feedback can establish in a situation where the interacting beams propagate in slightly different directions. Experimentally, it was shown that a MOPO indeed can operate in noncollinear configurations and that a single signal-idler pair is generated for each value of φ_G, with no measurable change in the bandwidths compared to when $\varphi_G = 0$. One could argue that the MOPO should operate at the wavelengths which experience the lowest oscillation threshold, or equivalently, which experience the highest parametric gain. This occurs for one of the configurations in Fig. 5.19. If the two signal-idler pairs with the same wavelengths are independent, and thus mutually incoherent, then the maximum gain should occur for the configuration with the largest beam overlap, *i.e.* for the pair with the smallest noncollinear angles $|\varphi_s|$ and $\pi - |\varphi_i|$. This occurs in Fig. 5.19(a), where the idler counterpropagates the pump and the signal propagates at an angle to compensate for the transverse component of the grating vector. If, on the other hand, both signal-idler pairs of the same frequencies contribute coherently to the parametric gain, the gain is maximised for the configuration in Fig. 5.19(b) where the two pairs become spatially degenerate. This can be seen by writing the wave equation for one of the phase matched signals as

$$\mathbf{k}_{s1} \cdot \nabla A_{s1} = i\frac{\omega_s^2 d_{eff}}{c^2} A_p \left[A_{i1}^* + A_{i2}^* e^{i(\mathbf{k}_{i1} - \mathbf{k}_{i2}) \cdot \mathbf{r}} \right], \tag{5.36}$$

which has two quasi-phase-matched contributions in the case when $\mathbf{k}_{i1} = \mathbf{k}_{i2}$. In terms of wave-vector magnitudes, this situation can be expressed as

$$k_s = k_i + \|\mathbf{k}_p - \mathbf{K}_G\|, \tag{5.37}$$

which means that the signal wavelength is minimised and that the idler wavelength consequently is maximised. The situation is equivalently described in terms of propagation angles as

$$|\varphi_s - \varphi_i| = \pi, \tag{5.38}$$

i.e. the signal and the idler are mutually counterpropagating.

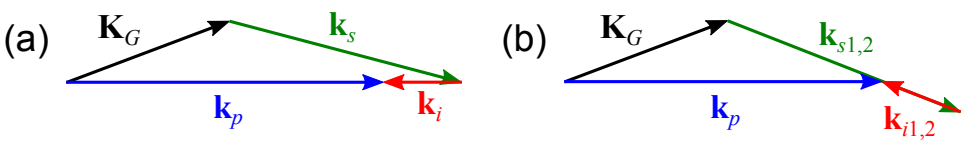

Fig. 5.19: (a) The idler counterpropagates the pump, resulting in the smallest angles and the largest beam overlap. (b) The idler counterpropagates the signal. For one specific wavelength pair, the two solutions in Fig. 5.18 coincide and become spatially degenerate.

The experimentally measured tuning from the collinear value and the beam angles are shown in Fig. 5.20, together with calculations for the spatially-degenerate configuration using the Sellmeier expansion by Fradkin *et. al* [85]. Two different pump

wavelengths around 813.3 nm and 879.2 nm were used and the pump intensity was $1.3I_{p,th0}$, where $I_{p,th0}$ is the collinear threshold intensity. As for the temperature tuning, the total tuning range is smaller than the FWHM signal bandwidth, so the angular tuning is measured on the spectrally-narrow backward idler. The angles are measured on the signal and the idler angles are calculated from the QPM condition. Note that the angles in Fig. 5.20 and Eq. (5.34) - Eq. (5.35) are defined relative to the pump inside the crystal, *i.e.* refraction at the crystal surfaces has been taken into account after the measurement. The physical rotation of the crystal is approximately $n_p\varphi_G \simeq 1.84\varphi_G$.

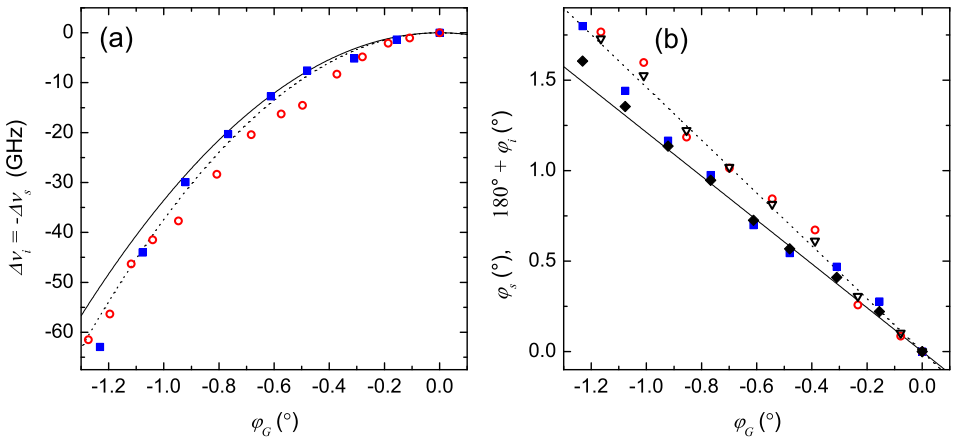

Fig. 5.20: (a) The idler tuning from the collinear value as function of φ_G. Pump at 813.3 nm: experimental points (squares) and calculation (solid line). Pump at 879.2 nm: Experimental points (circles) and calculation (dotted line). (b) The signal and idler angles as function of φ_G. Pump at 813.3 nm: measured φ_s (diamonds), φ_i deduced from experiments (squares) and calculation (solid line). Pump at 879.2 nm: measured φ_s (triangles), φ_i deduced from experiments (circles) and calculation (dotted line) [paper IV].

The angular tuning is rather slow and results in a shift of the idler of -63 GHz for $\varphi_G \simeq 1.2°$. An approximate expression for the tunability of the parametric frequencies with respect to φ_G can be derived for small angles when the MOPO is operating far from degeneracy. The small-angle approximation is valid when $\varphi_G \ll |\sqrt{n_p\Lambda/\lambda_p} - \sqrt{\lambda_p/(n_p\Lambda)}|$, which cannot be fulfilled near degeneracy, $\lambda_p/n_p \simeq \Lambda$. The angular tunability in the configuration with mutually counterpropagating signal and idler is given by

$$\frac{\partial\nu_i}{\partial\varphi_G} = -\frac{\partial\nu_s}{\partial\varphi_G} \simeq -\frac{v_{gs}v_{gi}}{v_{gs}+v_{gi}}\frac{1}{|\Lambda-\lambda_p/n_p|}\varphi_G, \tag{5.39}$$

which integrates to the angular tuning formula given in paper IV. Angular tuning of MOPOs is expected to always tune the signal and idler wavelengths away from

degeneracy, no matter which of the signal and idler that is the backward wave, but this remains to be verified experimentally for a backward signal. With a backward idler, the signal angle is in the small-angle approximation proportional to the grating angle,

$$\varphi_s \simeq -\frac{1}{\Lambda\left(n_s/\lambda_s - n_i/\lambda_i\right)}\varphi_G. \tag{5.40}$$

As the interaction goes from collinear to noncollinear, the beam overlap is reduced and the efficiency of the process decreases. This was investigated in paper IV by measuring the signal pulse energy as function of the grating angle when the pump power was increased to $2I_{p,th0}$. A pump beam with a radius of 110 μm was used, which determines the volume where the interaction can take place. The angular dependence on the efficiency for this pump beam and intensity is shown in Fig. 5.21.

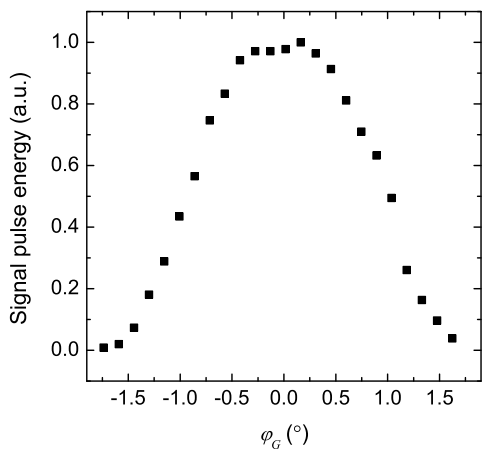

Fig. 5.21: The relative signal pulse energy as function of the grating angle, measured at $2I_{p,th0}$ with a pump beam radius of 110 μm [paper IV].

The efficiency clearly decreases with an increased rotation and eventually MOPO threshold cannot be reached. This could partially be circumvented by pumping the MOPO with a larger beam, *e.g.* with an elliptic beam that is larger in the y direction to increase the beam overlap throughout the crystal.

5.10 MOPO conversion efficiency

The conversion efficiency into signal and idler is an important parameter for the applicability of MOPOs. A direct measurement of the signal pulse energy as function of the pump pulse energy was done in [16] for 47 ps-long pump pulses, with the result presented in Fig. 5.22(a). For chirped pump pulses, the conversion efficiency

can also be estimated by measuring and comparing the input and output pump spectra, as is shown in Fig. 5.22(b) and (c) for 66 ps-long pulses with a negative linear chirp. The undepleted spectra are measured at the same pump power as the depleted ones, but with the beam propagating outside the structured area of the PPKTP crystal where the MOPO is not operational. In Fig. 5.22(b), the MOPO is close to threshold, $I_p \simeq 1.01 I_{p,th}$, and the interaction has just started depleting the pump. In Fig. 5.22(c), the pump intensity is increased to $I_p \simeq 1.44 I_{p,th}$ and clearly a larger part of the pump spectrum has been converted into parametric waves. The estimated average conversion efficiencies from the pump into signal and idler are in the two cases 9 % and 28 %, respectively. However, the pump is almost totally depleted at the end of the pulse and there seems to be no back-conversion from the parametric waves to the pump. The back-conversion depends on the product of the parametric amplitudes, $A_f(x)A_b(x)$, which in the counterpropagating configuration has a small value, since the parametric waves grow in opposite directions and one has its maximum where the other has its minimum. This can be seen in Fig. 5.2(b), where the intensity distributions inside the crystal are illustrated in the monochromatic approximation.

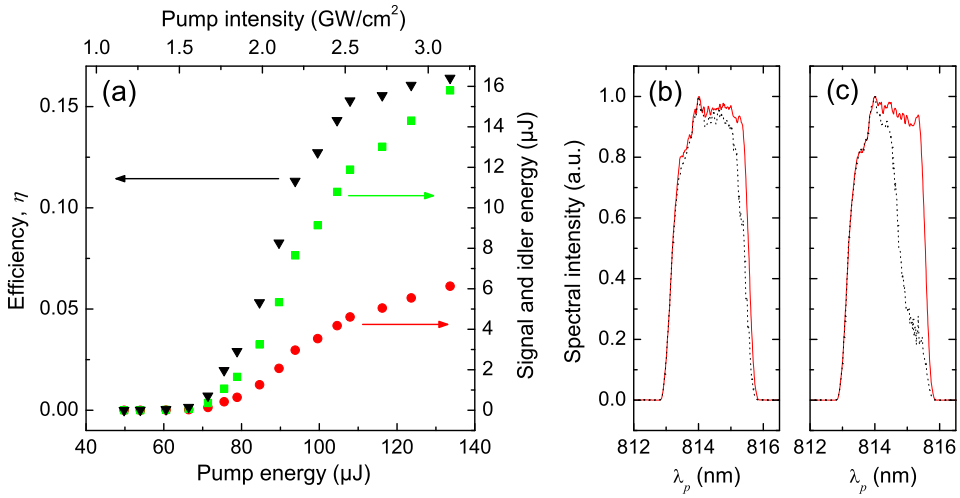

Fig. 5.22: (a) The conversion efficiency (triangles) and the signal (squares) and idler (circles) pulse energies as function of the pump pulse energy or peak intensity for 47 ps-long pump pulses [16]. (b), (c) The depleted (dotted line) and undepleted (solid line) pump spectra at $I_p \simeq 1.01 I_{p,th}$ and $I_p \simeq 1.44 I_{p,th}$ for 66 ps-long pump pulses.

5.11 Comparison with co-propagating parametric devices

In this section, the spectral and tuning properties of a MOPO with counterpropagating idler is compared with those of a co-propagating OPO or OPG. Just as for MOPOs, co-propagating OPOs can be made narrowband by the use of spectrally-selective elements, such as volume Bragg gratings [19]. However, the pumping of a crystal that is phase-matched for OPG in the forward direction gives a broadband output, unless spectral filtering is employed. Fig. 5.23(a) shows the signal spectra generated in a MOPO with $\Lambda \simeq 0.8$ μm and in another PPKTP crystal with $\Lambda \simeq 28.5$ μm that is phase matched for co-propagating OPG. Both are pumped at 827 nm with pulses of similar spectral widths.

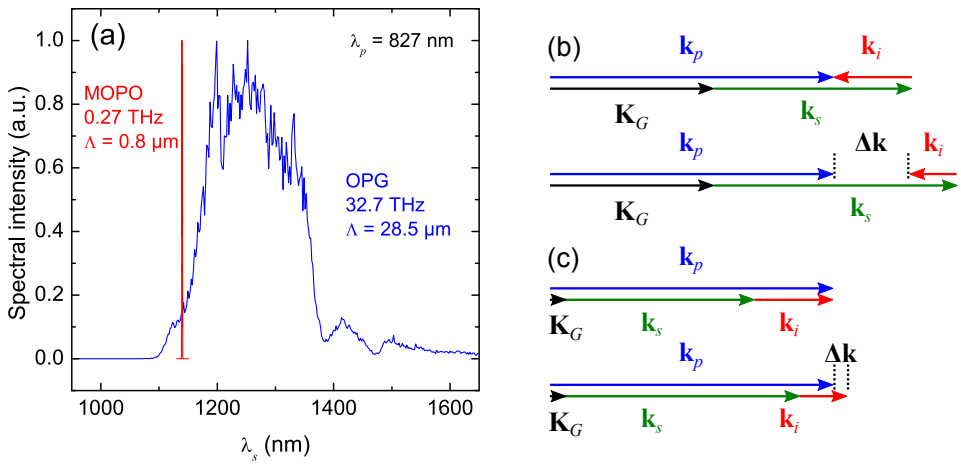

Fig. 5.23: (a) Comparison of the spectra generated in PPKTP crystals of periods $\Lambda \simeq 0.8$ μm and $\Lambda \simeq 28.5$ μm. (b), (c) For a given frequency detuning from the phase-matched point, the phase mismatch is much stronger in a counterpropagating interaction.

The OPG signal is more than 100 times broader than the MOPO signal. The idler spectra were not measured, but should in the co-propagating case be as broad as the signal, whereas it in the MOPO case is known to be around 13 GHz for similar pumping conditions and thereby differs from the co-propagating idler by a factor of 2500. The reason for the broadband output in the co-propagating case is that the phase mismatch varies slowly with a frequency detuning from the phase-matched point. This as can be seen by calculating the derivative of the phase mismatch, $\Delta k = k_p - k_s \pm k_i - K_G$, with respect to the change in the signal frequency for a constant pump frequency,

$$\frac{\partial(\Delta k)}{\partial \omega_s} = \frac{v_{gi} \pm v_{gs}}{v_{gi} v_{gs}}, \tag{5.41}$$

where the upper and lower signs in ± are for the cases with counterpropagating and co-propagating idler, respectively. With the sum of the group velocities in the numerator, the absolute value of the derivative is typically 300 times larger in the MOPO case than in the co-propagating case, meaning that the MOPO is much more sensitive for small detunings from the phase-matching point, as is schematically illustrated in Fig. 5.23(b) and (c).

The pump, grating and temperature tunabilities are also very different in the co-propagating and counterpropagating cases. For a numerical comparison, the pump, signal and idler wavelengths of 861.67 nm, 1217.94 nm and 2945.73 nm are considered (the same as in paper VI), which correspond to a PPKTP MOPO with $\Lambda \simeq 805$ nm or a co-propagating configuration with $\Lambda \simeq 30.27$ μm. In the MOPO case, a broad range of pump wavelengths can be used to pump the crystal, regardless of the dispersion in the medium. The large QPM grating vector allows the parametric waves to distribute the pump energy between themselves in such a way that the QPM condition is met. In the co-propagating case, the dispersion limits the pump-wavelength range where QPM is possible, typically to a few tens of nanometres. When QPM is possible, the pump tunabilities are

$$\frac{\partial \omega_s}{\partial \omega_p} = \frac{v_{gs}(v_{gi} \pm v_{gp})}{v_{gp}(v_{gi} \pm v_{gs})}, \tag{5.42}$$

$$\frac{\partial \omega_i}{\partial \omega_p} = \frac{v_{gi}(v_{gp} - v_{gs})}{v_{gp}(v_{gi} \pm v_{gs})}, \tag{5.43}$$

which for the selected wavelengths have the values 1.01 (-1.75) for the signal and -0.01 (2.75) for the idler, with the values in the brackets corresponding to the co-propagating case. The idler tunability is a factor of $(v_{gi} + v_{gs})/(v_{gi} - v_{gs}) \simeq -281$ faster in the co-propagating configuration, so the pump-tuning behaviours are completely different. It can also be seen that the phase-mismatch derivative with respect to the frequency detuning from phase matching, Eq. (5.41), differs by the same factor of -281, but has the larger magnitude in the counterpropagating case.

The tunability with respect to the QPM period is

$$\frac{\partial \nu_i}{\partial \Lambda} = -\frac{\partial \nu_s}{\partial \Lambda} = -\frac{1}{\Lambda^2} \frac{v_{gi} v_{gs}}{v_{gi} \pm v_{gs}}, \tag{5.44}$$

which has the value -124 GHz/nm (25 GHz/nm). These values differ by a factor of about -5, which is a much smaller difference than in the pump-tuning case. Despite the plus sign in the denominator, the MOPO tunes faster with a changed periodicity due to the fact that the QPM periods in the two cases differ by a factor of 38.

The temperature derivative is

$$\frac{\partial \nu_i}{\partial T} = -\frac{\partial \nu_s}{\partial T} = -\frac{1}{n_s \pm n_i} \left[\nu_s \left(\frac{\partial n_p}{\partial T} - \frac{\partial n_s}{\partial T} \right) + \nu_i \left(\frac{\partial n_p}{\partial T} \pm \frac{\partial n_i}{\partial T} \right) + \frac{c\alpha}{\Lambda} \right]. \tag{5.45}$$

The last term in Eq. (5.45) shows that the relative effect of thermal expansion becomes more pronounced in the counterpropagating configuration where the QPM periods are significantly shorter. For the selected wavelengths, the temperature derivative is -1.89 GHz/K (-24.1 GHz/K), whereof -0.91 GHz/K (-21.9 GHz/K) is attributed to the index change and -0.98 GHz/K (-2.1 GHz/K) to the thermal expansion. The temperature tuning is about 13 times faster in the co-propagating case, where most of the tuning is due to the change in the refractive index.

Regarding the angular tunability, it is hard to quantitatively compare the MOPO tuning with the tuning in co-propagating OPOs. In MOPOs, there is only one degree of freedom that can be controlled, *i.e.* the angle between the pump and the QPM grating, whereas the OPO designer has an additional degree of freedom in noncollinear co-propagating OPOs, where the propagation angle of the resonant wave can be changed by a rotation of the cavity. This fundamental difference makes a fair comparison of the two cases difficult. However, the angular tuning of a MOPO has so far been limited to 63 GHz, but could with a changed pumping geometry realistically be increased by at least a factor of 5. On the other hand, noncollinear interactions in co-propagating PPKTP devices reach angular tunabilities of 15 THz or more [107, 108], so the angular tunability of MOPOs can at this point be considered to be slow.

5.12 Conclusions

The spectral properties of mirrorless optical parametric oscillators are very different from those of conventional co-propagating OPOs as a result of the counterpropagating quasi-phase matching. A pump source with sufficient pulse energy and a properly engineered nonlinear crystal are the only things that are needed for the creation of a narrowband parametric source. It has been shown that the phase modulation in the pump is approximately transferred to the forward parametric wave, which means that the forward wave essentially is a frequency-shifted replica of the pump. The backward parametric wave then has a low phase modulation and a narrow bandwidth, which in simulations has been shown to be independent of if the phases in the pump are ordered, *e.g.* in a linear chirp, or if they are stochastic. Pumping with a narrowband pump, *i.e.* with a Q-switched laser, would automatically lead to the creation two narrowband parametric waves.

The strong dependence of the backward frequency on the QPM periodicity affects the tuning properties of MOPOs. With a fixed QPM period, the backward wave can only be tuned by a small amount. With $\Lambda \simeq 805$ nm, a tuning of the pump frequency by 26.8 THz shifts the backward idler by only (-)260 GHz, *i.e.* by approximately 1 % of the tuned pump. A change of the crystal temperature from 18 °C to 80 °C tunes the idler by about -100 GHz, or by -1.6 GHz/K. A rotation of the crystal so that the internal angle between the pump and the grating vector is 1.2° shifts the idler by about -60 GHz. Thus, the combined effects from a widley-tunable pump source, a rather large tempeature interval and some crystal

rotation can, for this QPM period, tune the backward wave in an interval of the order of 500 GHz, which for $\lambda_b \simeq 2952$ nm is about 15 nm, or a relative change of 0.5 %. The forward wave, on the other hand, tunes with the pump and has due to energy conservation the same temperature tuning and angular tuning as the backward wave, but with an opposite sign.

Chapter 6

Conclusions

In this thesis, I have described the nonlinear response in engineered optical materials, in particular in double-tungstate laser crystals and in periodically-poled $KTiOPO_4$.

The engineering of the chemical and crystallographic compositions of double-tungstate crystals leads to a modification of the Kerr nonlinearity. In paper I and paper II, the z-scan technique was used for the measurement of the Kerr nonlinearities of doped and undoped disordered-tetragonal and monoclinic $MT(XO_4)_2$ crystals. For the disordered-tetragonal crystals, with M = Na; T = Y, La, Gd, Lu or Bi; X = W or Mo, the values of n_2 range between $13 \cdot 10^{-16}$ cm^2/W and $68 \cdot 10^{-16}$ cm^2/W, and there is, for most of the measured compounds, a low anisotropy in n_2 for light of σ and π polarisations. An exception is NaBiW, which also has the largest n_2 of $68 \cdot 10^{-16}$ cm^2/W and $58 \cdot 10^{-16}$ cm^2/W for the σ and π polarisations, respectively. However, with the current growth techniques, NaBiW cannot be doped with sufficient amounts of laser ions without a degradation in the crystal quality.

For the monoclinic compounds, with M = K; T = Gd, Y, Yb or Lu; X = W, n_2 ranges between $15 \cdot 10^{-16}$ cm^2/W and $26 \cdot 10^{-16}$ cm^2/W. Just as for the linear refractive index, n_2 for these crystals is larger when $\mathbf{E}||N_m$ compared to when $\mathbf{E}||N_p$. The anisotropy is reduced when the crystals are doped with ytterbium. Still, n_2 is larger when $\mathbf{E}||N_m$, which also is the polarisation direction where the Yb^{3+} ions have the largest absorption and emission cross sections. The values of n_2 for these compounds tend to increase with the ionic radius of the T ion.

Considering all the measured compounds, the measured Kerr coefficients are 5 to 22 times as large as that of sapphire, $n_2 \simeq 3.1 \cdot 10^{-16}$ cm^2/W, which means that the double tungstates doped with active ions are good candidates for Kerr-lens modelocking of lasers. Thanks to the large Kerr nonlinearities, the intracavity focusing requirements for modelocking can be relaxed, which makes the cavity design more flexible. It should be emphasised that Yb-doped monoclinic double

tungstates have proven to be among the most efficient laser media to employ for the generation of ultrashort pulses.

Two different directions of the structure engineering of second-order nonlinear media have been used in this thesis. One direction is, as explained in paper III, the fabrication of large-aperture periodically-poled $KTiOPO_4$ crystals with a poling periodicity of $\Lambda = 38.86$ μm and a thickness of 3 mm for high-power laser applications. In these crystals, doping with rubidium improves the material's domain-switching properties and makes the domain walls straighter, at the same time as the domain broadening is reduced. These properties can be used for future improvement of the fabrication of thick Rb-doped PPKTP crystals, or for the fabrication of crystals with submicrometre periodicities.

The other direction of structure engineering is the use of submicrometre periodicities for the realisation of mirrorless optical parametric oscillators based on the distributed feedback between the counterpropagating parametric waves. As a result of the counterpropagating quasi-phase matching, the backward frequency has a very strong dependence on the QPM periodicity and can only be tuned with a small amount by changing the pump frequency. In the case with a QPM period of $\Lambda \simeq 805$ nm and a pump at Ti:sapphire wavelengths, a frequency shift in the pump of $\delta\omega_p$ only tunes the backward idler with approximately -0.01$\delta\omega_p$. As a result of energy conservation, most of the shift in the pump frequency is transferred to the forward signal, which here tunes slightly faster than the pump.

The slow pump tunability of the backward wave in MOPOs results in unique spectral properties. In paper V and paper VI, it was shown that the slow tunability leads to that most of the phase modulation in the pump is transferred to the forward parametric wave, which results in a backward parametric wave with low phase modulation and a narrow bandwidth. The transferred phase modulation essentially makes the forward wave a frequency-shifted replica of the pump. These are general spectral features of MOPOs, but are more pronounced in the cases where the group velocities of the forward wave and the pump are matched. In simulations, it was shown in paper VI that the phase-modulation transfer and the generation of a narrowband backward wave occur independently of the nature of the phase modulation in the pump. It does not matter if the pump phases are ordered, *e.g.* in a linear chirp, or if they are stochastic.

Apart from pump tuning of MOPOs, temperature tuning and angular tuning have been studied. Temperature tuning of a PPKTP crystal with a period of $\Lambda \simeq 805$ nm resulted in the slow tuning rate of the backward idler of -1.6 GHz/K. As explained in paper IV, the angular tuning is different compared to in co-propagating OPOs, as the output wavelengths and their propagation angles in MOPOs are self-selected by the nonlinear process. Angular tuning of the backward idler of -63 GHz was obtained by rotating the crystal so that the internal angle between the pump and the grating vector was 1.2°. With the strong dependence that the backward wave has on the QPM periodicity, the combined effects of pump tuning, temperature tuning and angular tuning only affect the backward wavelength to a small extent.

6.1 Outlook

With the relatively large Kerr nonlinearities in the $MT(XO_4)_2$ compounds, it should be possible to use these crystals doped with laser ions to construct Kerr-lens modelocked lasers, as has already been proven in the past. New cavity designs may be possible with the knowledge of the values of the Kerr coefficients.

As counterpropagating parametric devices form a very young subfield of nonlinear optics, many experiments remain to be done. Some of these may require longer crystals, as the oscillation threshold scales inversely to the square of the length of the periodically-poled area. The thresholds for 6.5 mm-long crystals are typically obtained at peak intensities around 1 GW/cm^2, which for a crystal length of 15 mm would be reduced to 200 MW/cm^2. Improved fabrication techniques are required for the fabrication of periodically-poled gratings with submicrometre periodicity that have a large degree of homogeneity over 10 millimetres or more, but can realistically be done with Rb-doping of the $KTiOPO_4$ crystals. With improved fabrication techniques, it is also possible to further reduce the grating periodicities and have a degenerate MOPO or a MOPO with a backward signal.

From a fundamental point of view, it is interesting to investigate the limitations that the pump spectrum imposes on the MOPO operation. In paper VI, the MOPO was successfully pumped with the most broadband pump source available that met the requirements of pulse energy and pulse length. It was shown in simulations that MOPOs can be pumped with highly incoherent pulses of stochastic phase modulation, but this remains to verify experimentally. However, from a practical point of view, it is probably more interesting to go in the other direction and pump MOPOs with pulses from a narrowband Q-switched laser and generate two spectrally-narrow parametric waves.

The spatial-coherence properties of MOPOs have so far not been well studied. For a given pump beam, this can be done by varying the focusing conditions inside the MOPO crystal and see how that affects the spatial properties of the parametric beams.

References

[1] T. H. Maiman, *Stimulated Optical Radiation in Ruby*, Nature **187**, 493 (1960).

[2] A. Javan, W. R. Bennett and D. R. Herriott, *Population Inversion and Continuous Optical Maser Oscillation in a Gas Discharge Containing a He-Ne Mixture*, Phys. Rev. Lett. **6**, 106 (1961).

[3] L. F. Johnson and K. Nassau, *Infrared fluorescence and stimulated emission of Nd^{3+} in $CaWO_4$*, Proc. IRE **49**, 1704 (1961).

[4] H. W. Etzel, H. W. Gandy and R. J. Ginther, *Stimulated Emission of Infrared Radiation from Ytterbium Activated Silicate Glass*, Appl. Opt. **1**, 534 (1962).

[5] R. N. Hall, G. E. Fenner, J. D. Kingsley, T. J. Soltys and R. O. Carlson, *Coherent Light Emission From GaAs Junctions*, Phys. Rev. Lett. **9**, 366 (1962).

[6] F. P. Schäfer, W. Schmidt and J. Volze, *Organic dye solution laser*, Appl. Phys. Lett. **9**, 306 (1966).

[7] F. J. McClung and R. W. Hellwarth, *Giant Optical Pulsations from Ruby*, J. Appl. Phys. **33**, 828 (1962).

[8] L. E. Hargrove, R. L. Fork and M. A. Pollack, *Locking of He-Ne laser modes induced by synchronous intracavity modulation*, Appl. Phys. Lett. **5**, 4 (1964).

[9] P. A. Franken, A. E. Hill, C. W. Peters and G. Weinreich, *Generation of Optical Harmonics*, Phys. Rev. Lett. **7**, 118 (1961).

[10] M. Bass, P. A. Franken, A. E. Hill, C. W. Peters and G. Weinreich, *Optical Mixing*, Phys. Rev. Lett. **8**, 18 (1962).

[11] J. M. DiDomenico, R. H. Pantell, O. Svelto and J. N. Weaver, *Optical frequency mixing in bulk semiconductors*, Appl. Phys. Lett. **1**, 77 (1962).

[12] J. A. Giordmaine and R. C. Miller, *Tunable Coherent Parametric Oscillation in $LiNbO_3$ at Optical Frequencies*, Phys. Rev. Lett. **14**, 973 (1965).

[13] D. E. Spence, P. N. Kean and W. Sibbett, *60-fsec pulse generation from a self-mode-locked Ti:sapphire laser*, Opt. Lett. **16**, 42 (1991).

[14] J. A. Armstrong, N. Bloembergen, J. Ducuing and P. S. Pershan, *Interactions between Light Waves in a Nonlinear Dielectric*, Phys. Rev. **127**, 1918 (1962).

[15] S. E. Harris, *Proposed backward wave oscillation in the infrared*, Appl. Phys. Lett. **9**, 114 (1966).

[16] C. Canalias and V. Pasiskevicius, *Mirrorless optical parametric oscillator*, Nature Photonics **1**, 459 (2007).

[17] L. B. Kreuzer, *Single mode oscillation of a pulsed singly resonant optical parametric oscillator*, Appl. Phys. Lett. **15**, 263 (1969).

[18] S. Brosnan and R. Byer, *Optical parametric oscillator threshold and linewidth studies*, IEEE J. Quantum. Electron. **15**, 415 (1979).

[19] B. Jacobsson, M. Tiihonen, V. Pasiskevicius and F. Laurell, *Narrowband bulk Bragg grating optical parametric oscillator*, Opt. Lett. **30**, 2281 (2005).

[20] A. Yariv, *Quantum electronics* (Wiley, 1989).

[21] R. Boyd, *Nonlinear optics* (Academic Press, 2003).

[22] R. Sutherland, *Handbook of nonlinear optics* (Marcel Dekker, 1996).

[23] E. Goulielmakis, M. Uiberacker, R. Kienberger, A. Baltuska, V. Yakovlev, A. Scrinzi, T. Westerwalbesloh, U. Kleineberg, U. Heinzmann, M. Drescher and F. Krausz, *Direct Measurement of Light Waves*, Science **305**, 1267 (2004).

[24] S. Wang, V. Pasiskevicius, F. Laurell and H. Karlsson, *Ultraviolet generation by first-order frequency doubling in periodically poled $KTiOPO_4$*, Opt. Lett. **23**, 1883 (1998).

[25] A. Zukauskas, N. Thilmann, V. Pasiskevicius, F. Laurell and C. Canalias, *5 mm thick periodically poled Rb-doped KTP for high energy optical parametric frequency conversion*, Opt. Mater. Express **1**, 201 (2011).

[26] P. D. Maker, R. W. Terhune, M. Nisenoff and C. M. Savage, *Effects of Dispersion and Focusing on the Production of Optical Harmonics*, Phys. Rev. Lett. **8**, 21 (1962).

[27] J. A. Giordmaine, *Mixing of Light Beams in Crystals*, Phys. Rev. Lett. **8**, 19 (1962).

[28] V. Petrov, V. Badikov, V. Panyutin, G. Shevyrdyaeva, S. Sheina and F. Rotermund, *Mid-IR optical parametric amplification with femtosecond pumping near 800 nm using $Cd_xHg_{1-x}Ga_2S_4$*, Opt. Commun. **235**, 219 (2004).

[29] G. D. Boyd and C. K. N. Patel, *Enhancement of optical second-harmonic generation (SHG) by reflection phase matching in ZnS and GaAs*, Appl. Phys. Lett. **8**, 313 (1966).

[30] M. S. Piltch, C. D. Cantrell and R. C. Sze, *Infrared second-harmonic generation in nonbirefringent cadmium telluride*, J. Appl. Phys. **47**, 3514 (1976).

[31] M. Yamada, N. Nada, M. Saitoh and K. Watanabe, *First-order quasi-phase matched $LiNbO_3$ waveguide periodically poled by applying an external field for efficient blue second-harmonic generation*, Appl. Phys. Lett. **62**, 435 (1993).

[32] J. Webjorn, V. Pruneri, P. Russell, J. Barr and D. Hanna, *Quasi-phase-matched blue light generation in bulk lithium niobate, electrically poled via periodic liquid electrodes*, Electron. Lett. **30**, 894 (1994).

[33] H. Karlsson and F. Laurell, *Electric field poling of flux grown $KTiOPO_4$*, Appl. Phys. Lett. **71**, 3474 (1997).

[34] C. Canalias, V. Pasiskevicius, R. Clemens and F. Laurell, *Submicron periodically poled flux-grown $KTiOPO_4$*, Appl. Phys. Lett. **82**, 4233 (2003).

[35] C. Canalias, V. Pasiskevicius, M. Fokine and F. Laurell, *Backward quasi-phase-matched second-harmonic generation in submicrometer periodically poled flux-grown $KTiOPO_4$*, Appl. Phys. Lett. **86**, 181105 (2005).

[36] L. A. Eyres, P. J. Tourreau, T. J. Pinguet, C. B. Ebert, J. S. Harris, M. M. Fejer, L. Becouarn, B. Gerard and E. Lallier, *All-epitaxial fabrication of thick, orientation-patterned GaAs films for nonlinear optical frequency conversion*, Appl. Phys. Lett. **79**, 904 (2001).

[37] A. Chowdhury, H. M. Ng, M. Bhardwaj and N. G. Weimann, *Second-harmonic generation in periodically poled GaN*, Appl. Phys. Lett. **83**, 1077 (2003).

[38] J. K. Hite, M. E. Twigg, N. D. Bassim, M. M. Mastro, F. J. Kub and C. R. Eddy, in *Periodically Oriented GaN for Optical Parametric Generation*, Lasers, Sources, and Related Photonic Devices (Optical Society of America, 2012), ITh5B.1.

[39] X. Mu, I. B. Zotova, Y. J. Ding and W. P. Risk, *Backward second-harmonic generation in submicron-period ion-exchanged $KTiOPO_4$ waveguide*, Opt. Commun. **181**, 153 (2000).

[40] M. Fejer, G. Magel, D. Jundt and R. Byer, *Quasi-phase-matched second harmonic generation: tuning and tolerances*, IEEE J. Quantum. Electron. **28**, 2631 (1992).

[41] M. V. Pack, D. J. Armstrong and A. V. Smith, *Measurement of the $\chi^{(2)}$ Tensors of $KTiOPO_4$, $KTiOAsO_4$, $RbTiOPO_4$, and $RbTiOAsO_4$ Crystals*, Appl. Opt. **43**, 3319 (2004).

[42] L. E. Myers, G. D. Miller, R. C. Eckardt, M. M. Fejer, R. L. Byer and W. R. Bosenberg, *Quasi-phase-matched 1.064-μm-pumped optical parametric oscillator in bulk periodically poled $LiNbO_3$*, Opt. Lett. **20**, 52 (1995).

[43] G. P. Agrawal, *Nonlinear fiber optics: its history and recent progress [Invited]*, J. Opt. Soc. Am. B **28**, A1 (2011).

[44] F. Shimizu, *Frequency Broadening in Liquids by a Short Light Pulse*, Phys. Rev. Lett. **19**, 1097 (1967).

[45] R. R. Alfano and S. L. Shapiro, *Emission in the Region 4000 to 7000 Å Via Four-Photon Coupling in Glass*, Phys. Rev. Lett. **24**, 584 (1970).

[46] A. Brodeur and S. L. Chin, *Ultrafast white-light continuum generation and self-focusing in transparent condensed media*, J. Opt. Soc. Am. B **16**, 637 (1999).

[47] S. A. Planas, N. L. P. Mansur, C. H. B. Cruz and H. L. Fragnito, *Spectral narrowing in the propagation of chirped pulses in single-mode fibers*, Opt. Lett. **18**, 699 (1993).

[48] L. F. Mollenauer, R. H. Stolen and J. P. Gordon, *Experimental Observation of Picosecond Pulse Narrowing and Solitons in Optical Fibers*, Phys. Rev. Lett. **45**, 1095 (1980).

[49] M. A. Duguay and J. W. Hansen, *An ultrafast light gate*, Appl. Phys. Lett. **15**, 192 (1969).

[50] T. Morioka, M. Saruwatari and A. Takada, *Ultrafast optical multi/demultiplexer utilising optical Kerr effect in polarisation-maintaining single-mode fibres*, Electron. Lett. **23**, 453 (1987).

[51] R. Y. Chiao, E. Garmire and C. H. Townes, *Self-Trapping of Optical Beams*, Phys. Rev. Lett. **13**, 479 (1964).

[52] P. L. Kelley, *Self-Focusing of Optical Beams*, Phys. Rev. Lett. **15**, 1005 (1965).

[53] J. E. Bjorkholm and A. A. Ashkin, *cw Self-Focusing and Self-Trapping of Light in Sodium Vapor*, Phys. Rev. Lett. **32**, 129 (1974).

[54] A. García-Cortés, J. M. Cano-Torres, X. Han, C. Cascales, C. Zaldo, X. Mateos, S. Rivier, U. Griebner, V. Petrov and F. J. Valle, *Tunable continuous wave and femtosecond mode-locked Yb^{3+} laser operation in $NaLu(WO_4)_2$*, J. Appl. Phys. **101**, 063110 (2007).

[55] M. Rico, A. Méndez-Blas, V. Volkov, M. Ángeles Monge, C. Cascales, C. Zaldo, A. Kling and M. T. Fernández-Díaz, *Polarization and local disorder effects on the properties of Er^{3+}-doped $XBi(YO_4)_2$, X = Li or Na and Y = W or Mo, crystalline tunable laser hosts*, J. Opt. Soc. Am. B **23**, 2066 (2006).

[56] C. Cascales, M. D. Serrano, F. Esteban-Betegón, C. Zaldo, R. Peters, K. Petermann, G. Huber, L. Ackermann, D. Rytz, C. Dupré, M. Rico, J. Liu, U. Griebner and V. Petrov, *Structural, spectroscopic, and tunable laser properties of Yb^{3+}-doped $NaGd(WO_4)_2$*, Phys. Rev. B **74**, 174114 (2006).

[57] C. Cascales, A. M. Blas, M. Rico, V. Volkov and C. Zaldo, *The optical spectroscopy of lanthanides R^{3+} in $ABi(XO_4)_2$ (A = Li, Na; X = Mo, W) and $LiYb(MoO_4)_2$ multifunctional single crystals: Relationship with the structural local disorder*, Opt. Mater. **27**, 1672 (2005).

[58] X. Han, A. García-Cortés, M. D. Serrano, C. Zaldo and C. Cascales, *Structural and Thermal Properties of Tetragonal Double Tungstate Crystals Intended for Ytterbium Laser Composites*, Chem. Mater. **19**, 3002 (2007).

[59] R. Solé, V. Nikolov, X. Ruiz, J. Gavaldà, X. Solans, M. Aguiló and F. Díaz, *Growth of β-$KGd_{1-x}Nd_x(WO_4)_2$ single crystals in $K_2W_2O_7$ solvents*, J. Cryst. Growth **169**, 600 (1996).

[60] V. Petrov, M. Cinta Pujol, X. Mateos, O. Silvestre, S. Rivier, M. Aguiló, R. Solé, J. Liu, U. Griebner and F. Díaz, *Growth and properties of $KLu(WO_4)_2$, and novel ytterbium and thulium lasers based on this monoclinic crystalline host*, Laser & Photon. Rev. **1**, 179 (2007).

[61] X. Mateos, R. Solé, J. Gavaldà, M. Aguiló, J. Massons and F. Díaz, *Crystal growth, optical and spectroscopic characterisation of monoclinic $KY(WO_4)_2$ co-doped with Er^{3+} and Yb^{3+}*, Opt. Mater. **28**, 423 (2006).

[62] A. García-Cortés, J. Cano-Torres, M. Serrano, C. Cascales, C. Zaldo, S. Rivier, X. Mateos, U. Griebner and V. Petrov, *Spectroscopy and Lasing of Yb-Doped $NaY(WO_4)_2$: Tunable and Femtosecond Mode-Locked Laser Operation*, IEEE J. Quantum. Electron. **43**, 758 (2007).

[63] H. Liu, J. Nees and G. Mourou, *Diode-pumped Kerr-lens mode-locked $Yb{:}KY(WO_4)_2$ laser*, Opt. Lett. **26**, 1723 (2001).

[64] B. Jacobsson, *Experimental and theoretical investigation of a volume-Bragg-grating-locked Yb:KYW laser at selected wavelengths*, Opt. Express **16**, 6443 (2008).

[65] K. V. Yumashev, N. N. Posnov, P. V. Prokoshin, V. L. Kalashnikov, F. Mejid, I. Poloyko, V. P. Mikhailov and V. P. Kozich, *Z-scan measurements of nonlinear refraction and Kerr-lens mode-locking with $Yb^{3+}{:}KY(WO_4)_2$*, Opt. Quantum. Electron. **32**, 43 (2000).

[66] A. Vodchits, V. Kozich, V. Orlovich and P. Apanasevich, *Z-Scan studies of KYW, KYbW, KGW, and $Ba(NO_3)_2$ crystals*, Opt. Commun. **263**, 304 (2006).

[67] A. Major, I. Nikolakakos, J. Aitchison, A. Ferguson, N. Langford and P. Smith, *Characterization of the nonlinear refractive index of the laser crystal $Yb{:}KGd(WO_4)_2$*, Appl. Phys. B: Lasers Opt. **77**, 433 (2003).

[68] M. Sheik-Bahae, A. Said, T.-H. Wei, D. Hagan and E. Van Stryland, *Sensitive measurement of optical nonlinearities using a single beam*, IEEE J. Quantum. Electron. **26**, 760 (1990).

[69] A.-C. Tien, S. Backus, H. Kapteyn, M. Murnane and G. Mourou, *Short-Pulse Laser Damage in Transparent Materials as a Function of Pulse Duration*, Phys. Rev. Lett. **82**, 3883 (1999).

[70] A. Owyoung, R. W. Hellwarth and N. George, *Intensity-Induced Changes in Optical Polarizations in Glasses*, Phys. Rev. B **5**, 628 (1972).

[71] J. Fournier and E. Snitzer, *The nonlinear refractive index of glass*, IEEE J. Quantum. Electron. **10**, 473 (1974).

[72] D. Huang, M. Ulman, L. H. Acioli, H. A. Haus and J. G. Fujimoto, *Self-focusing-induced saturable loss for laser mode locking*, Opt. Lett. **17**, 511 (1992).

[73] X. Chen, Y. Leng, J. Liu, Y. Zhu, R. Li and Z. Xu, *Pulse self-compression in normally dispersive bulk media*, Opt. Commun. **259**, 331 (2006).

[74] A. Major, J. Aitchison, P. Smith, F. Druon, P. Georges, B. Viana and G. Aka, *Z-scan measurements of the nonlinear refractive indices of novel Yb-doped laser crystal hosts*, Appl. Phys. B: Lasers Opt. **80**, 199 (2005).

[75] A. García-Cortés, J. M. Cano-Torres, X. Han, C. Cascales, C. Zaldo, X. Mateos, S. Rivier, U. Griebner, V. Petrov and F. J. Valle, *Tunable continuous wave and femtosecond mode-locked Yb^{3+} laser operation in $NaLu(WO_4)_2$*, J. Appl. Phys. **101**, 063110 (2007).

[76] A. Major, F. Yoshino, I. Nikolakakos, J. S. Aitchison and P. W. E. Smith, *Dispersion of the nonlinear refractive index in sapphire*, Opt. Lett. **29**, 602 (2004).

[77] V. Volkov, M. Rico, A. Méndez-Blas and C. Zaldo, *Preparation and properties of disordered $NaBi(XO_4)_2$, X=W or Mo, crystals doped with rare earths*, J. Phys. Chem. Solids **63**, 95 (2002).

[78] X. Feng, A. K. Mairaj, D. W. Hewak and T. M. Monro, *Nonsilica Glasses for Holey Fibers*, J. Lightwave Technol. **23**, 2046 (2005).

[79] J. D. Bierlein and H. Vanherzeele, *Potassium titanyl phosphate: properties and new applications*, J. Opt. Soc. Am. B **6**, 622 (1989).

[80] N. Sorokina and V. Voronkova, *Structure and properties of crystals in the potassium titanyl phosphate family: A review*, Crystallogr. Rep. **52**, 80 (2007).

[81] Z. W. Hu, P. A. Thomas and P. Q. Huang, *High-resolution x-ray diffraction and topographic study of ferroelectric domains and absolute structural polarity of* $KTiOPO_4$ *via anomalous scattering*, Phys. Rev. B **56**, 8559 (1997).

[82] S. Wang, V. Pasiskevicius and F. Laurell, *High-efficiency frequency converters with periodically-poled Rb-doped $KTiOPO_4$*, Opt. Mater. **30**, 594 (2007).

[83] G. Hansson, H. Karlsson, S. Wang and F. Laurell, *Transmission Measurements in KTP and Isomorphic Compounds*, Appl. Opt. **39**, 5058 (2000).

[84] T. Y. Fan, C. E. Huang, B. Q. Hu, R. C. Eckardt, Y. X. Fan, R. L. Byer and R. S. Feigelson, *Second harmonic generation and accurate index of refraction measurements in flux-grown $KTiOPO_4$*, Appl. Opt. **26**, 2390 (1987).

[85] K. Fradkin, A. Arie, A. Skliar and G. Rosenman, *Tunable midinfrared source by difference frequency generation in bulk periodically poled $KTiOPO_4$*, Appl. Phys. Lett. **74**, 914 (1999).

[86] K. Kato and E. Takaoka, *Sellmeier and Thermo-Optic Dispersion Formulas for KTP*, Appl. Opt. **41**, 5040 (2002).

[87] G. Ghosh, *Temperature dispersion in KTP for nonlinear devices*, IEEE Photonic. Tech. L. **7**, 68 (1995).

[88] F. Laurell, M. G. Roelofs, W. Bindloss, H. Hsiung, A. Suna and J. D. Bierlein, *Detection of ferroelectric domain reversal in $KTiOPO_4$ waveguides*, J. Appl. Phys. **71**, 4664 (1992).

[89] P. Urenski, M. Lesnykh, Y. Rosenwaks, G. Rosenman and M. Molotskii, *Anisotropic domain structure of $KTiOPO_4$ crystals*, J. Appl. Phys. **90**, 1950 (2001).

[90] C. Canalias, J. Hirohashi, V. Pasiskevicius and F. Laurell, *Polarization-switching characteristics of flux-grown $KTiOPO_4$ and $RbTiOPO_4$ at room temperature*, J. Appl. Phys. **97**, 124105 (2005).

[91] C. Canalias, S. Wang, V. Pasiskevicius and F. Laurell, *Nucleation and growth of periodic domains during electric field poling in flux-grown $KTiOPO_4$ observed by atomic force microscopy*, Appl. Phys. Lett. **88**, 032905 (2006).

[92] H. Karlsson, F. Laurell and L. K. Cheng, *Periodic poling of $RbTiOPO_4$ for quasi-phase matched blue light generation*, Appl. Phys. Lett. **74**, 1519 (1999).

[93] Y. Sheng, T. Wang, B. Ma, E. Qu, B. Cheng and D. Zhang, *Anisotropy of domain broadening in periodically poled lithium niobate crystals*, Appl. Phys. Lett. **88**, 041121 (2006).

[94] A. C. Busacca, C. L. Sones, V. Apostolopoulos, R. W. Eason and S. Mailis, *Surface domain engineering in congruent lithium niobate single crystals: A route to submicron periodic poling*, Appl. Phys. Lett. **81**, 4946 (2002).

[95] G. Rosenman, P. Urenski, A. Arie, M. Roth, N. Angert, A. Skliar and M. Tseitlin, *Polarization reversal and domain grating in flux-grown $KTiOPO_4$ crystals with variable potassium stoichiometry*, Appl. Phys. Lett. **76**, 3798 (2000).

[96] W. Shi and Y. J. Ding, *Generation of backward terahertz waves in GaSe crystals*, Opt. Lett. **30**, 1861 (2005).

[97] C.-S. Chuu and S. E. Harris, *Ultrabright backward-wave biphoton source*, Phys. Rev. A **83**, 061803 (2011).

[98] Y. Ding and J. Khurgin, *Backward optical parametric oscillators and amplifiers*, IEEE J. Quantum. Electron. **32**, 1574 (1996).

[99] H. Kogelnik and C. V. Shank, *Stimulated emission in a periodic structure*, Appl. Phys. Lett. **18**, 152 (1971).

[100] H. Kogelnik and C. V. Shank, *Coupled-Wave Theory of Distributed Feedback Lasers*, J. Appl. Phys. **43**, 2327 (1972).

[101] D. S. Chemla, E. Batifol, R. L. Byer and R. L. Herbst, *Optical backward mixing in sodium nitrite*, Opt. Commun. **11**, 57 (1974).

[102] A. Picozzi and M. Haelterman, *Parametric Three-Wave Soliton Generated from Incoherent Light*, Phys. Rev. Lett. **86**, 2010 (2001).

[103] A. Picozzi, C. Montes and M. Haelterman, *Coherence properties of the parametric three-wave interaction driven from an incoherent pump*, Phys. Rev. E **66**, 056605 (2002).

[104] K. Özgören, B. Öktem, S. Yilmaz, F. Ömer Ilday and K. Eken, *83 W, 3.1 MHz, square-shaped, 1 ns-pulsed all-fiber-integrated laser for micromachining*, Opt. Express **19**, 17647 (2011).

[105] M. Ebrahimzadeh, G. J. Hall and A. I. Ferguson, *Broadly tunable, all-solid-state, visible and infrared picosecond optical parametric oscillator*, Opt. Lett. **18**, 278 (1993).

[106] M. Tiihonen, V. Pasiskevicius, A. Fragemann, C. Canalias and F. Laurell, *Ultrabroad gain in an optical parametric generator with periodically poled $KTiOPO_4$;*, Appl. Phys. B: Lasers Opt. **85**, 73 (2006).

[107] M. Tiihonen, V. Pasiskevicius and F. Laurell, *Noncollinear double-ring optical parametric oscillators with periodically poled $KTiOPO_4$*, Opt. Express **12**, 5526 (2004).

[108] A. Fragemann, V. Pasiskevicius and F. Laurell, *Broadband nondegenerate optical parametric amplification in the mid infrared with periodically poled $KTiOPO_4$*, Opt. Lett. **30**, 2296 (2005).

Part II

Papers I - VI